



UNIVERSIDADE FEDERAL DO RIO DE JANEIRO
INSTITUTO DE FÍSICA

Influence of van der Waals corrections on multi layer graphene/graphite systems in Density Functional Theory

Rafael Rodrigues Del Grande

Dissertação de Mestrado apresentada ao Programa de Pós-Graduação em Física do Instituto de Física da Universidade Federal do Rio de Janeiro - UFRJ, como parte dos requisitos necessários à obtenção do título de Mestre em Ciências (Física).

Orientador: Rodrigo Barbosa Capaz

Coorientador: Marcos Gonçalves de Menezes

Rio de Janeiro

Março de 2017

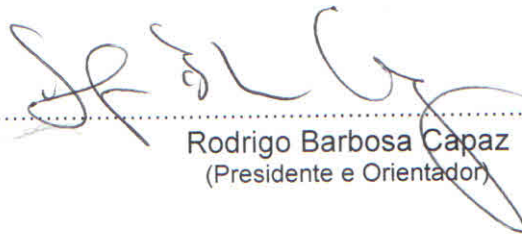
Influence of van der Waals corrections on multi layer graphene/graphite systems in Density Functional

Rafael Rodrigues Del Grande

Rodrigo Barbosa Capaz
Marcos Gonçalves de Menezes

Dissertação de Mestrado submetida ao Programa de Pós-Graduação em Física, Instituto de Física, da Universidade Federal do Rio de Janeiro – UFRJ, como parte dos requisitos necessários à obtenção do título de Mestre em Ciências (Física).

Aprovada por:



Rodrigo Barbosa Capaz
(Presidente e Orientador)



Marcos Gonçalves de Menezes
(Co-Orientador)



Leandro Malard Moreira



Pedro Paulo de Mello Venezuela

- P436 Del Grande, Rafael Rodrigues
Influence of van der Waals corrections on multi layer graphene/graphite systems in Density Functional Theory / Rafael Rodrigues Del Grande - Rio de Janeiro: UFRJ/IF, 2017.
xx, 86f.
Orientador: Rodrigo Barbosa Capaz
Coorientador: Marcos Gonçalves de Menezes
Dissertação (mestrado) - UFRJ / Instituto de Física / Programa de Pós-graduação em Física, 2017.
Referências Bibliográficas: f. 73-83.
1. Introduction. 2. Methodology. 3. Results and Discussion. 4. Conclusions. I. Capaz, Rodrigo Barbosa. II. Menezes, Marcos G. III. Universidade Federal do Rio de Janeiro, Instituto de Física, Programa de Pós-graduação em Física. IV. Influence of van der Waals corrections on multi layer graphene/graphite systems in Density Functional Theory.

Resumo

Influence of van der Waals corrections on multi layer graphene/graphite systems in Density Functional Theory

Rafael Rodrigues Del Grande

Orientador: Rodrigo Barbosa Capaz

Coorientador: Marcos Gonçalves de Menezes

Resumo da Dissertação de Mestrado apresentada ao Programa de Pós-Graduação em Física do Instituto de Física da Universidade Federal do Rio de Janeiro - UFRJ, como parte dos requisitos necessários à obtenção do título de Mestre em Ciências (Física).

O grafeno é um material formado por uma folha de átomos de carbono com a espessura de um único átomo que tem atraído atenção devido às suas propriedades mecânicas, elétricas e óticas não usuais. É possível empilhar diversas camadas de grafeno para se obter grafeno multicamadas (multilayer graphene), cujas propriedades são sensíveis ao número de camadas e à orientação relativa entre elas.

Estes materiais têm sido extensivamente estudados teoricamente ao longo dos anos com o auxílio da Teoria Funcional da Densidade (DFT na sigla em inglês), entretanto as interações de van der Waals (VDW), que são fundamentais para a estabilidade desses materiais, só foram incluídas em estudos mais recentes. Neste trabalho, a influência de diferentes formas de inclusão da interação de VDW nos cálculos DFT sobre as propriedades mecânicas e as frequências de vibração de modos óticos de baixa energia desses materiais é analisada e comparada.

Observamos que constantes elásticas e frequências de fônons relacionados ao deslocamento entre camadas são substancialmente alteradas, tanto para grafite quanto para grafeno multicamada, com a inclusão da interação de VDW. Interessantemente, sem a inclusão da interação de VDW, a aproximação LDA (densidade local) para o funcional de troca e correção da DFT provê uma boa descrição de algumas propriedades muito melhores do que a aproximação GGA (gradiente generalizado), e comparável com os resultados obtidos com funcionais de VDW.

Palavras-chave: Grafeno, Grafite, DFT, van der Waals

Abstract

Influence of van der Waals corrections on multi layer graphene/graphite systems in Density Functional Theory

Rafael Rodrigues Del Grande

Orientador: Rodrigo Barbosa Capaz

Coorientador: Marcos Gonçalves de Menezes

Abstract da Dissertação de Mestrado apresentada ao Programa de Pós-Graduação em Física do Instituto de Física da Universidade Federal do Rio de Janeiro - UFRJ, como parte dos requisitos necessários à obtenção do título de Mestre em Ciências (Física).

Graphene is one atom thick material made of carbon atoms that have attracted attention because of its unusual mechanical, electrical and optical properties. It is possible to stack several graphene layers in order to obtain multilayer graphene, which have properties that are sensitive to the number of layers and their relative orientation.

Those materials have been theoretically studied over the years with the Density Functional Theory (DFT), although the van der Waals (VDW) interactions, that are fundamental for those materials stability, have just recently been included on these studies. In this work, the influence of different ways of including VDW interactions in DFT calculations over the mechanical properties and vibrational frequencies of small energy optical modes of those materials is analyzed and compared.

We observe that, for both graphite and multilayer graphene, elastic constants and phonon frequencies related to inter-layer displacements are substantially altered with the inclu-

sion of VDW interactions. Interestingly, without VDW corrections, LDA (local density approximation) provides a fair description of some interlayer properties as well, much better than GGA (generalized gradient approximation) without VDW corrections, and comparable to the results obtained using VDW corrections.

Keywords: Graphene, Graphite, DFT, van der Waals

Agradecimentos

Agradeço ao meu orientador, Prof. Rodrigo Capaz, pela dedicação, confiança e paciência comigo desde a minha iniciação científica no meu segundo ano de faculdade (completando 5 anos de trabalho agora no final do mestrado!). Agradeço ao meu coorientador, Prof. Marcos Menezes, pelas discussões e por responder mensagens 00:50 de uma sexta-feira. Aos integrantes do grupo NAMOR que incluem além dos meus orientadores a Prof^a Belita Koiller, o Prof. André Saraiva, Amintor, Francisco e Adriana. Aos pesquisadores do Industrial Technology & Science group da IBM Research no Rio de Janeiro: Ronaldo Giro, Mathias Steiner, Rodrigo Neumann, Peter Bryant, Jaione Azpiroz e Claudius Feger, mostrando que ciência de qualidade pode sim ser feita no Brasil fora das universidades. Aos professores que tive durante a graduação e no mestrado, citando alguns: Luca Moriconi, Renata Simão, Pierre Esteves, Gilberto Weissmuller e Rafael Valverde. Ao Prof. Bruno Horta pela amizade. Cada um dos professores citados nesse parágrafo contribuiu em diferentes aspectos na minha formação como cientista. A todos, obrigado!

Agradeço à minha esposa e melhor amiga Gabriela por me aturar falando sobre ciências a qualquer hora. Aos meus pais, Marcelo e Carla, que são exemplos de pessoas e minhas referências de vida. À minha irmã, Nana, que eu perturbo. Aos meus familiares, que mesmo longe, sei que torcem pela minha felicidade e sucesso.

Aos meus amigos antigos de colégio, G13, pela amizade verdadeira. Aos colegas e amigos do curso de Nanotecnologia da UFRJ e ainda da empresa junior do curso, a Auger Nanotecnologia, que sempre me lembram o que inovação e força de vontade para mudar o mundo realmente significam. Aos amigos da pós graduação em física, Cláudio, Arouca, Carlos, Pedro, Tarik, Diego e tantos outros pelas discussões e zueiras.

Agradeço as agências de fomento CNPq e INCT nanomateriais de carbono pelo suporte financeiro oferecido durante o mestrado.

Contents

Abstract	x
List of Figures	xiii
List of Tables	xx
1 Introduction	1
1.1 Why study graphene?	1
1.2 Crystal structure	7
1.2.1 Graphene	7
1.2.2 Multilayer graphene	8
1.2.3 Graphite	10
2 Methodology	11
2.1 Crystal Hamiltonian	11
2.2 Born-Oppenheimer approximation	12
2.3 Density Functional Theory (DFT)	15
2.3.1 Introduction	15
2.3.2 The Hohenberg-Kohn theorems	17
2.3.3 The Kohn-Sham equations	20
2.3.4 Exchange-Correlation functional	23
2.3.5 Plane-waves	26

2.3.6	\vec{K} -point sampling	28
2.3.7	Pseudopotentials	29
2.4	Van der Waals interactions	32
2.4.1	Van der Waals on DFT	33
2.5	Crystalline vibrations	36
2.5.1	Dynamical Matrix	36
2.5.2	Forces on DFT	41
2.6	Calculation of Phonon Spectra	42
2.6.1	Frozen Phonon	42
2.6.2	Finite Difference Method	44
2.6.3	Density Functional Perturbation Theory (DFPT)	45
3	Results and Discussion	48
3.1	Technical Details	48
3.2	Lattice and Elastic Constants	49
3.2.1	Graphene	49
3.2.2	Graphite	51
3.2.3	Multilayer Graphene	58
3.3	Phonon Dispersion	59
3.3.1	Graphene	60
3.3.2	Graphite	60
3.3.3	Multilayer Graphene	64
4	Conclusions	73
	Bibliography	75
A	Eigenvectors for frozen phonon calculations	86
A.1	Bilayer graphene	87

A.2	Trilayer graphene	88
A.3	4-layer graphene	88
A.4	5-layer graphene	89
A.5	Graphite	89
B	Anharmonic Effects included by First Order Perturbation Theory	91

List of Figures

- 1.1 Schematic view of graphene generating others materials, respectively from left to the right: fullerene (0 dimensional), carbon nanotube (1 dimensional), graphite (3 dimensional). Figure reproduced from [1]. 2
- 1.2 Electronic dispersion of graphene with emphasis in the linear relation near the K and K' points of the first Brillouin zone. Figure reproduced from [7]. 3
- 1.3 $t(n+m)$ LGs are multilayer graphene with $n+m$ layers where the first n layers are rotated in relation to the other m layers, so $t(2+2)$ LG and $t(1+3)$ LG have the same number of layers but their relative orientation are different. Stokes/anti-Stokes Raman spectra in the C peak region and Stokes spectra in the G and 2D spectral regions for four $t(m+n)$ LGs are shown above. The excitation energy used for each $t(m+n)$ LG is indicated. Figure reproduced from [9]. 4
- 1.4 (a) Stokes and anti-stokes C peaks and G peak for multilayer graphene and graphite (bulk). (b) C and G peaks dependence on the number of layers in multilayer graphene. Figure reproduced from [33]. 5
- 1.5 (a) Raman spectra for multilayer graphene of different thickness and stacking order. (b) The frequency of the subpeaks in the LOZO' band for multilayer graphene with two stacking orders as a function of layer thickness. The error bars correspond to the width of Raman features. Figure reproduced from [35]. 5

1.6	Convergence of out of plane (left) and in plane (right) frequencies as a function of the number of layers. In both figures solid, open, and thick ring symbols denote, respectively, Raman, IR, and simultaneous Raman and IR activity. Dashed lines indicate the corresponding frequency values in bulk graphite. Figure adapted from [34].	6
1.7	Comparison of several VDW functionals to evaluate the binding energy between a graphene sheet and a Ni(111) surface. As one can notice the PBE functional gives a much smaller binding energy. Figure reproduced from [57].	7
1.8	Hexagonal sublattices A and B of graphene and the basis vectors \vec{a}_1 and \vec{a}_2 generating a honeycomb structure. Reciprocal lattice generated by \vec{b}_1 and \vec{b}_2 . First Brillouin zone and some high symmetry points (Γ , M , K and K'). Figure reproduced from [7].	8
1.9	Top view of bilayer graphene in configurations AB (left) and AA (right). Figure created with xcrysdn software [18,19].	9
1.10	Trilayer graphene in configurations ABA (left) and ABC (right). Figure reproduced from [20].	10
1.11	Graphite lattice structure (left) and first Brillouin zone and some high symmetry points. Figure adapted from [21].	10
2.1	Schematic algorithm to solve self-consistently the Kohn-Sham equations. The σ index indicates the spin degree of freedom, which is not discussed in this work. Figure reproduced from [16].	23
2.2	Representation of the BZ and IBZ of a square lattice. Figure reproduced from [59].	29
2.3	Schematic representation of the pseudopotential method in order to make the wave function smoother. Figure reproduced from [17].	30

2.4	F_x for various GGA_x functionals. Figure reproduced from [54].	35
	36figure.caption.30	
2.6	Phonon dispersion of graphene. As it has 2 atoms per unit cell there will be 6 branches. In graphene context the ZO and ZA branches indicate out-of-plane modes. Figure reproduced from [64].	41
3.1	Murnaghan fit (eq. 3.1) for $E(A)$. Harmonic fit is presented for comparison	50
3.2	Comparison of the performance of several functionals for the a lattice constant. The experimental value is 2.4607\AA [71]	51
3.3	Comparison of the performance of several functionals for the c lattice constant. The experimental value is 6.7053\AA [71]	52
3.4	$C_{11} + C_{12}$ elastic constant divided by its experimental value (1240GPa at 300K) [71]	53
3.5	C_{33} elastic constant divided by its experimental value (36.5GPa at 300K) [71]	54
3.6	C_{13} elastic constant divided by its experimental value (15GPa at 300K) [71]	54
3.7	C_t elastic constant divided by its experimental value (208.8GPa at 300K) [71]	55
3.8	Bulk modulus divided by its experimental value (35.8GPa at 300K) [71] . .	55
3.9	Graphite supercell used to evaluate poisson ratio, represented by the black rectangle. \hat{y} direction corresponds to armchair direction and \hat{x} to zig-zag. Figure created with xcrysden software [18,19].	56
3.10	Example of poisson ratio evaluation	56
3.11	Poisson ratio evaluated by applying distortion in the armchair (zig-zag) direction and measuring distortion in the zig-zag (armchair) direction. Experimental value: $\nu_{exp} = 0.165$ [72]	57

3.12	Interlayer interaction energy per atom in graphite as a function of the interlayer distance $c/2$ evaluated for several functionals. Horizontal dashed lines represent experimental values for the exfoliation energy per atom [78] and the horizontal line represents the experimental value for the interlayer distance 3.35265\AA [71]. Experimental values in meV/atom are: 42 [79], 35 [80], 52 [81], 31 [82]	58
3.13	Mean interlayer distance for multilayer graphene and graphite.	59
3.14	K path for evaluation of the phonon dispersion for graphite. For graphene and multilayer graphene the same path is used except the $A - \Gamma$ part . . .	59
3.15	(Left) Phonon dispersion of graphene calculated in the LDA and GGA approximations. (Right) Solid line: GGA calculation [71] on graphene and experimental data of graphite. The experimental data are EELS (electron energy loss spectroscopy) from [87–89] (respectively squares, diamonds, and filled circles), neutron scattering from [90] (open circles), and x-ray scattering from [86] (triangles). Figure reproduced from [71]	60
3.16	(Left) Phonon dispersion for graphite using GGA (red) and LDA (blue) with the theoretical lattice parameters (solid lines) or experimental (dashed lines). (Right) GGA (solid lines) and LDA (dashed lines) from [71]. The experimental data are EELS (electron energy loss spectroscopy) from [87–89] (respectively squares, diamonds, and filled circles), neutron scattering from [90] (open circles), and x-ray scattering from [86] (triangles). Figure reproduced from [71]	61
3.17	Example of frozen phonon calculations for out-of-plane (left) and in-plane (right) modes. The two in plane modes (displacements in the armchair and zigzag directions) are degenerate. Harmonic fits (green curves) are presented for comparison.	62

- 3.18 Comparison of DFPT method and frozen-phonon for several functionals for the in plane mode frequency at the Γ point. Experimental value is 42 cm^{-1} [91]. Bars without label DFPT refer to frozen phonon calculations. 63
- 3.19 Comparison of DFPT method and frozen-phonon for several functionals for the out of plane mode. Experimental value is 127 cm^{-1} [91]. Bars without label DFPT refer to frozen phonon calculations. 63
- 3.20 Phonon dispersion of bilayer graphene (top left), trilayer graphene (top right), 4layer graphene (down left) and 5layer graphene (down right) using LDA (red lines) and GGA (blue lines) functionals. Units in cm^{-1} 65
- 3.21 Force in the out-of-plane direction on the edge layer of 4-layer graphene as a function of the displacement in the out-of-plane direction of the same layer as an example of evaluation of a matrix element of the FCM. This example corresponds to $\mu = 1$ and $\nu = 1$ in eq. 2.104 66
- 3.22 Out of plane frozen phonon (FP), finite difference (FD) and DFPT calculations (triangles, reverse triangles and circles respectively) using GGA (blue), LDA (red) and vdw-df2-c09 (green) functionals. Experimental value for the layer breathing mode of graphite is from [91] and black crosses are experimental values from two-phonon overtone spectra observed in doubly resonant Raman spectroscopy in [94]. Lines are connecting the higher frequencies for each N-layer to show the convergence of those values with the number of layers until they reach the graphite frequency. Theoretical calculations of graphite presented here were done with the theoretical lattice parameters (figs. 3.19). 67

- 3.23 Effect of including anharmonic effects in the out-of-plane modes in frozen phonon calculations. Squares include anharmonic effects and triangles do not using GGA (blue), LDA (red) and vdw-df2-c09 (green) functionals. Experimental value for the layer breathing mode of graphite is from [91] and black crosses are experimental values from two-phonon overtone spectra observed in doubly resonant Raman spectroscopy in [94]. Lines are connecting the higher frequencies for each N-layer to show the convergence of those values until graphite frequency. Theoretical calculations of graphite presented here were done with the theoretical lattice parameters (figs. 3.18). 68
- 3.24 In plane frozen phonon (FP), finite difference (FD) and DFPT calculations (triangles, reverse triangles and circles respectively) using GGA (blue), LDA (red) and vdw-df2-c09 (green) functionals. Experimental value for the shear mode of graphite is from [91], black crosses are ab initio calculations from [33] and cyan stars are experimental Raman measures of C peak position from [33]. Lines are connecting the higher frequencies for each N-layer to show the convergence of those values until graphite frequency. Theoretical calculations of graphite presented here were done with the theoretical lattice parameters (figs. 3.18). 69
- 3.25 Convergence of the frequency of the highest mode of 5-layer graphene in relation to the number of K points sampling 70

3.26	In plane frozen phonon (FP) using higher K points sampling than in fig. 3.24, finite difference (FD) and DFPT calculations (triangles, reverse triangles and circles respectively) using GGA (blue), LDA (red) and vdw-df2-c09 (green) functionals. Experimental value for the shear mode of graphite is from [91], black crosses are ab initio calculations from [33] and cyan stars are experimental Raman measures of C peak position from [33]. Lines are connecting the higher frequencies for each N-layer to show the convergence of those values until graphite frequency. Theoretical calculations of graphite presented here were done with the theoretical lattice parameters (figs. 3.18).	71
A.1	Plot of the ratio ω_N/ω_∞ as a function of the number of layers using equation A.1.	87

List of Tables

3.1	Some physical parameters of graphene	51
3.2	$(\omega_{\text{graphite}}/\omega_{\text{bilayer}})^2$	72

Chapter 1

Introduction

1.1 Why study graphene?

Graphene is a two-dimensional material made of carbon that has attracted attention because of its physical properties and possible applications for industrial and academic purposes. It consists of a honeycomb arrangement of sp^2 carbon atoms and is one atom thick. For many years this material was studied just theoretically but since its experimental isolation in 2004 [1–3] by mechanical exfoliation of graphite the interest in it has been increased substantially.

There are other nanomaterials related to graphene, shown in the Figure 1.1. The first one is a 0D fullerene molecule (C_{60}) that was discovered by Kroto, Curl and Smalley [4, 5] who won the Nobel Prize in Chemistry in 1996. The C_{60} molecule is composed of 60 equivalent carbon atoms and it has the shape of a soccer ball. The second one is a 1D carbon nanotube, discovered by Iijima [6]. Both molecules are not synthesized from graphene but, schematically, they can be understood as rolled up graphene sheets. Graphite can be considered as a stack of several graphene layers with different relative orientations.

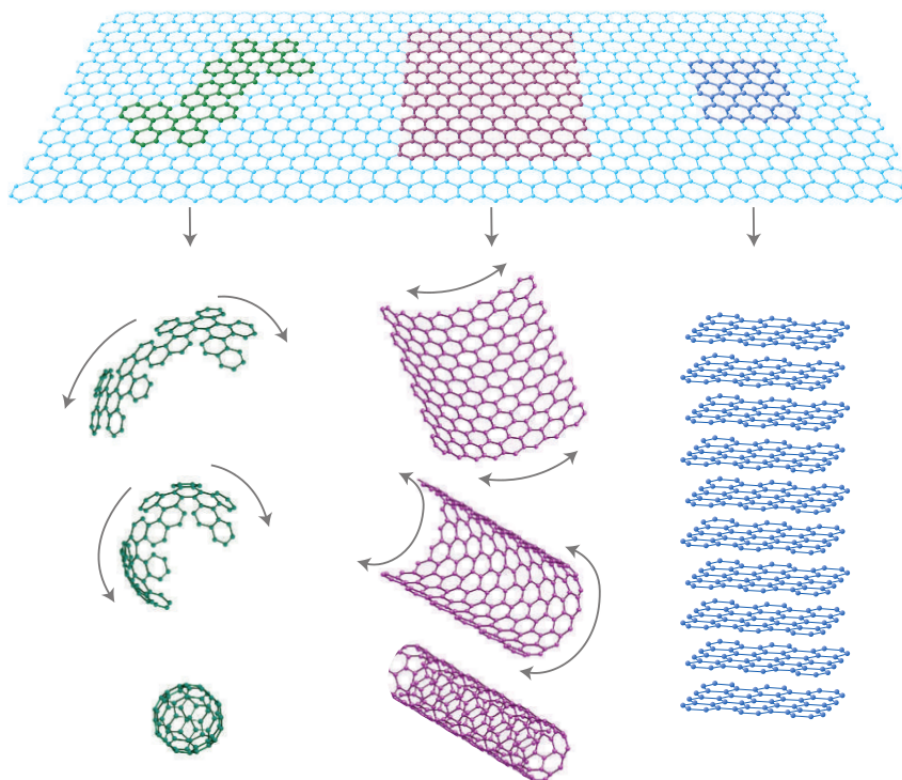


Figure 1.1: Schematic view of graphene generating others materials, respectively from left to the right: fullerene (0 dimensional), carbon nanotube (1 dimensional), graphite (3 dimensional).Figure reproduced from [1].

Graphene has special electronic properties. It is a zero-gap semiconductor and its valence and conduction bands touch each other at two points of the Brillouin zone (K and K') where the electronic dispersion is linear as a consequence of the symmetry between the graphene sublattices [2]. In addition to it, states in the valence and conduction bands are primarily described by the same spinor wave function, so electrons and holes are linked via charge conjugation what implies that quasiparticles in graphene obey chiral symmetry, similar to that happens between particles and antiparticles in quantum electrodynamics (QED). This behavior allows experiments that measures electronic properties of graphene to probe some QED phenomena [2].

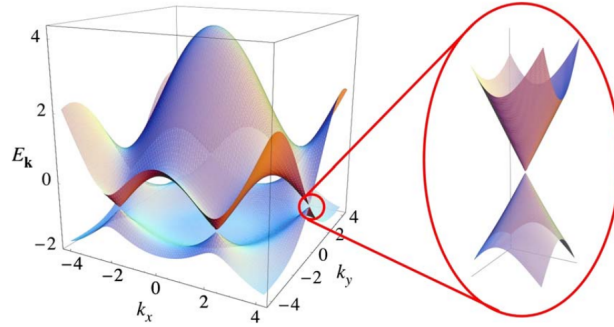


Figure 1.2: Electronic dispersion of graphene with emphasis in the linear relation near the K and K' points of the first Brillouin zone. Figure reproduced from [7].

The vibrational properties have also substantial importance. As graphene is made of light carbon atoms and the in plane bonds are strong, its sound velocity is high and its phonon dispersion has been studied theoretically and experimentally [8].

It is possible to stack several graphene layers. For a large number of layers we have graphite and for few layers we have multilayer graphene. The electronic and mechanical properties for multilayer graphene are sensitive to the number of graphene layers and their relative orientation. For example, for bilayer graphene, the electronic dispersion goes from linear to parabolic near the K point [7]. For multilayer graphene it is possible to characterize the relative orientation between layers with Raman spectroscopy [9] as shown in Figure 1.3. One interesting peak in multilayer graphene and graphite in this work is the C peak as it represents the frequency of shear modes in those materials.

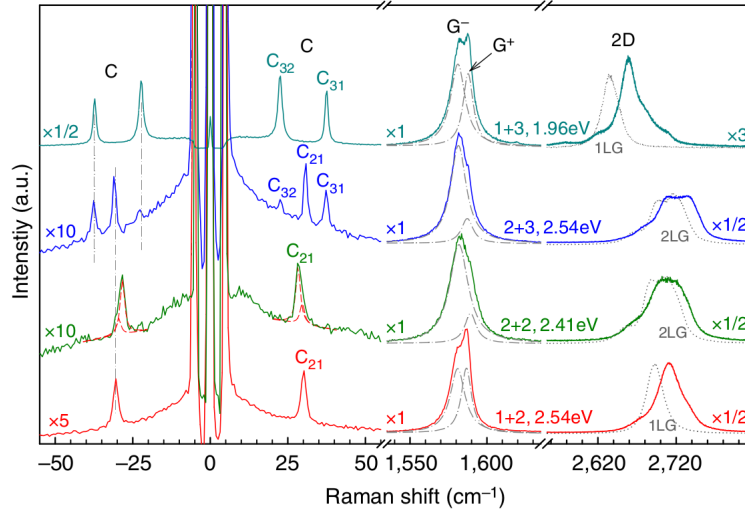


Figure 1.3: $t(n+m)$ LGs are multilayer graphene with $n+m$ layers where the first n layers are rotated in relation to the other m layers, so $t(2+2)$ LG and $t(1+3)$ LG have the same number of layers but their relative orientation are different. Stokes/anti-Stokes Raman spectra in the C peak region and Stokes spectra in the G and 2D spectral regions for four $t(m+n)$ LGs are shown above. The excitation energy used for each $t(m+n)$ LG is indicated. Figure reproduced from [9].

For vibrational dispersion, the frequency of modes with relative movement between the layers is highly influenced by the van der Waals (VDW) interactions [33]. From graphene to multilayer graphene, the understanding of how its physical properties change with the number of layers and their relative orientation is essential. Previous experimental and theoretical works evaluated the dependence of low-frequency optical modes on the number of layers. The shear modes of multilayer graphene were measured with Raman spectroscopy and well reproduced with DFT using LDA (local density approximation) without VDW corrections in [33] (see fig. 1.4). In [35] layer-breathing modes were observed using a Raman combination mode measuring the LO+ZO' combination mode of the out of plane layer breathing mode (ZO) and the in plane longitudinal optical mode (LO) (see fig. 1.5). In [34] the convergence of in-plane and out-plane modes frequencies was observed from bilayer graphene to graphite (Fig. 1.6) using DFT without VDW corrections.

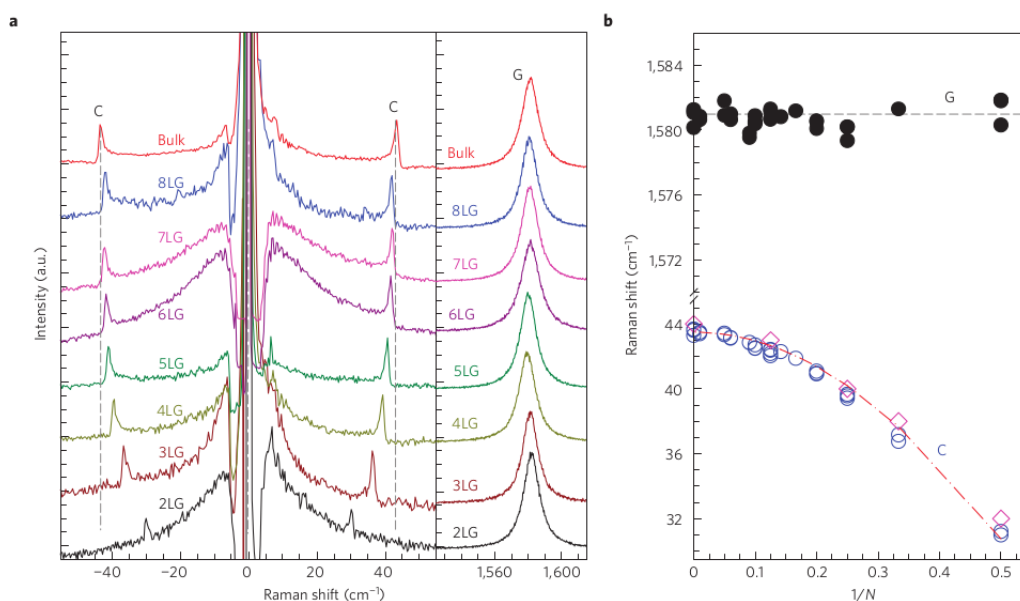


Figure 1.4: (a) Stokes and anti-stokes C peaks and G peak for multilayer graphene and graphite (bulk). (b) C and G peaks dependence on the number of layers in multilayer graphene. Figure reproduced from [33].

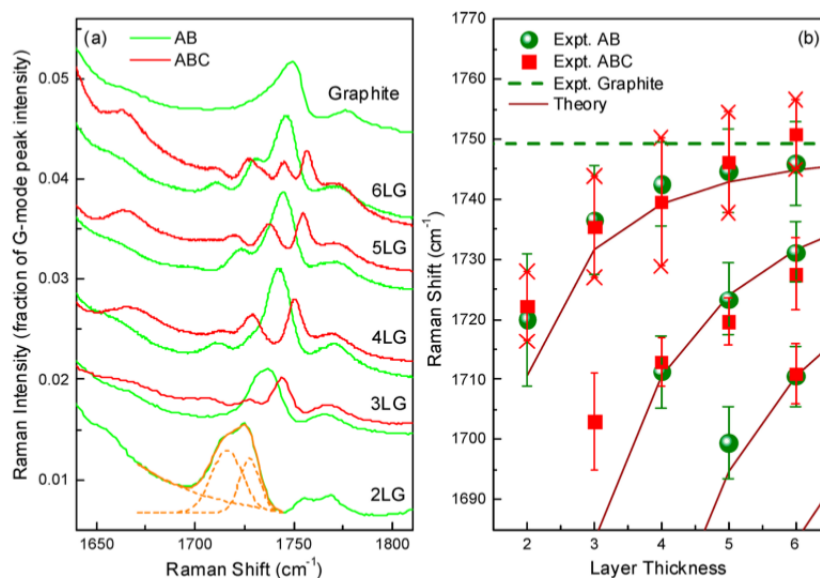


Figure 1.5: (a) Raman spectra for multilayer graphene of different thickness and stacking order. (b) The frequency of the subpeaks in the LOZO' band for multilayer graphene with two stacking orders as a function of layer thickness. The error bars correspond to the width of Raman features. Figure reproduced from [35].

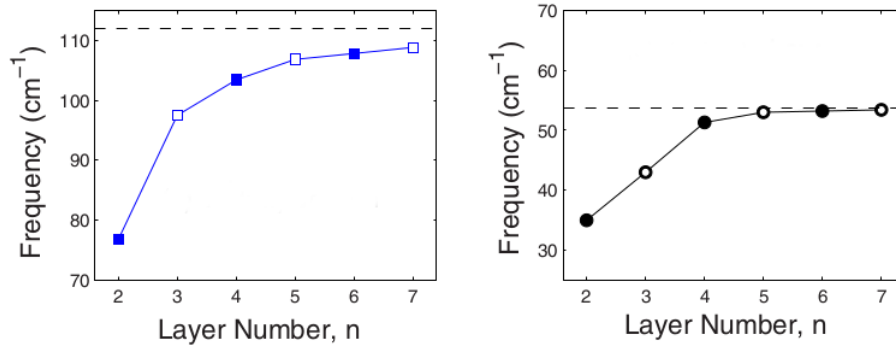


Figure 1.6: Convergence of out of plane (left) and in plane (right) frequencies as a function of the number of layers. In both figures solid, open, and thick ring symbols denote, respectively, Raman, IR, and simultaneous Raman and IR activity. Dashed lines indicate the corresponding frequency values in bulk graphite. Figure adapted from [34].

As those stacked structures are stabilized by VDW interactions, the purpose of this work is to analyze the effect of including those interactions on DFT calculations. As graphene is also a prototype for two dimensional materials, the understanding of graphene and multilayer graphene can help the understanding and development of other 2D materials and related heterostructures [40, 41].

There are works that compare several VDW corrections on DFT and in general binding energies and equilibrium distances are improved [57, 78] as one can see in fig. 1.7. Currently in Quantum Espresso package [68] the use of VDW corrections to evaluate the phonon dispersion through Density Functional Perturbation Theory (DFPT) is not yet implemented, however there are current works extending DFPT to include non-local VDW interactions [92]. For better explanations of VDW corrections on DFT and DFPT see sections 2.4.1 and 2.6.3 respectively.

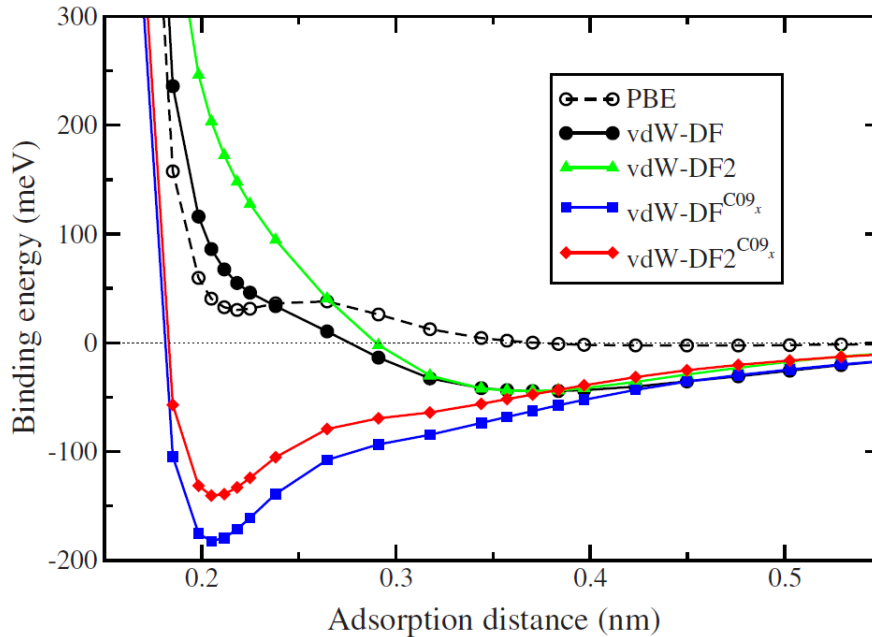


Figure 1.7: Comparison of several VDW functionals to evaluate the binding energy between a graphene sheet and a Ni(111) surface. As one can notice the PBE functional gives a much smaller binding energy. Figure reproduced from [57].

1.2 Crystal structure

1.2.1 Graphene

Carbon is an element with six electrons whose electronic distribution is $1s^2 2s^2 2p^2$. The $1s^2$ electrons are strongly bound to the nucleus and usually do not participate in the chemical bonds and are called core electrons. The remaining four electrons are responsible for the bonds in the carbon atom and are called valence electrons. The $2p$ and the $2s$ energy levels are relatively close to each other. This allows the mixing of the valence electrons' wave function changing the occupation of the $2p$ and the $2s$ orbitals. This mixing is the hybridization of the carbon atom and it is called sp^n ($n = 1, 2, 3$) [10, 11]. In graphene the carbon atoms are in sp^2 hybridization and in this configuration each atom has three σ bonds belonging to the same plane making an angle of 120° with respect to each other. The remaining valence electron is in the p_z orbital that is perpendicular to the σ orbitals.

Graphene consists in a honeycomb two dimensional lattice with a basis containing

two atoms. It is composed of two hexagonal sublattices: A and B (see Figure 1.8). The primitive vectors can be chosen to be [7]:

$$\vec{a}_1 = a \left(\frac{\sqrt{3}}{2}, \frac{1}{2} \right), \quad \vec{a}_2 = a \left(\frac{\sqrt{3}}{2}, -\frac{1}{2} \right); \quad (1.1)$$

where $a \approx 2.46\text{\AA}$ is the lattice parameter and the carbon-carbon distance is $d_{C-C} = a/\sqrt{3} \approx 1.42\text{\AA}$. The reciprocal lattice vectors are given by:

$$\vec{b}_1 = \frac{2\pi}{a} \left(\frac{1}{\sqrt{3}}, 1 \right), \quad \vec{b}_2 = \frac{2\pi}{a} \left(\frac{1}{\sqrt{3}}, -1 \right); \quad (1.2)$$

It is easy to see that the real space lattice vectors and the reciprocal lattice vectors obey the relation $\vec{a}_i \cdot \vec{b}_j = 2\pi\delta_{ij}$, where δ_{ij} is the Kronecker delta [12].

The basis can be chosen to be:

$$\vec{\tau}_1 = (0, 0), \quad \vec{\tau}_2 = \left(\frac{2a}{\sqrt{3}}, 0 \right); \quad (1.3)$$

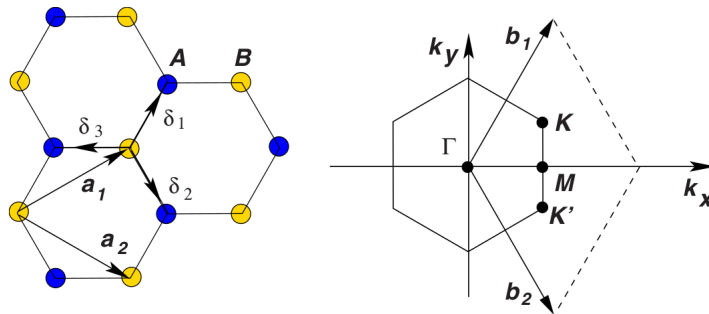


Figure 1.8: Hexagonal sublattices A and B of graphene and the basis vectors \vec{a}_1 and \vec{a}_2 generating a honeycomb structure. Reciprocal lattice generated by \vec{b}_1 and \vec{b}_2 . First Brillouin zone and some high symmetry points (Γ , M , K and K'). Figure reproduced from [7].

1.2.2 Multilayer graphene

For multilayer graphene the crystal structure is the same of graphene: it has the same primitive vectors, as long as there is no relative rotation between the layers. What changes is the basis as it is necessary to put one layer over the another.

For bilayer graphene there are two ways of stacking called: AA and AB. In the AA stacking both layers have the same atoms positions just changing its z component:

$$\vec{\tau}_1 = (0, 0, 0), \vec{\tau}_2 = \left(\frac{2a}{\sqrt{3}}, 0, 0 \right), \vec{\tau}_3 = (0, 0, \delta), \vec{\tau}_4 = \left(\frac{2a}{\sqrt{3}}, 0, \delta \right); \quad (1.4)$$

In the AB stacking the layer above is translated by $a/\sqrt{3}\hat{x}$:

$$\vec{\tau}_1 = (0, 0, 0), \vec{\tau}_2 = \left(\frac{2a}{\sqrt{3}}, 0, 0 \right), \vec{\tau}_3 = \left(\frac{a}{\sqrt{3}}, 0, \delta \right), \vec{\tau}_4 = \left(\sqrt{3}a, 0, \delta \right); \quad (1.5)$$

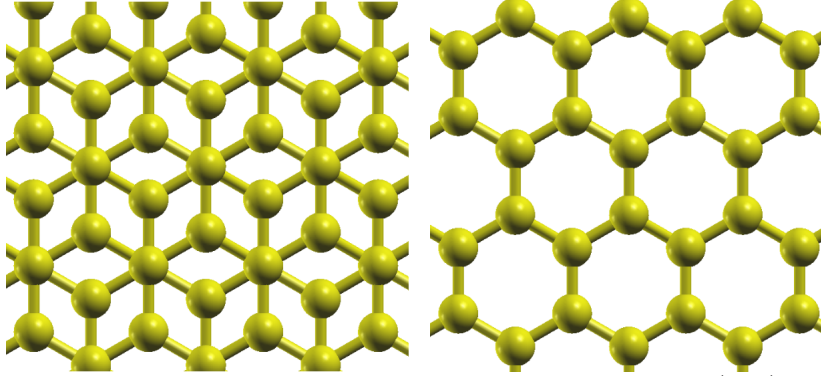


Figure 1.9: Top view of bilayer graphene in configurations AB (left) and AA (right). Figure created with xcrsden software [18, 19].

For trilayer graphene, one can find ABA (Bernal) and ABC (rhombohedral) stacking as shown in Figure 1.10. In ABA structure the third layer is a replica of the first one and on ABC structure the third layer is translated by $(2a/\sqrt{3})\hat{x}$ in relation to the first one. The difference between them is that the ABA structure exhibits mirror symmetry and ABC has inversion symmetry [20].

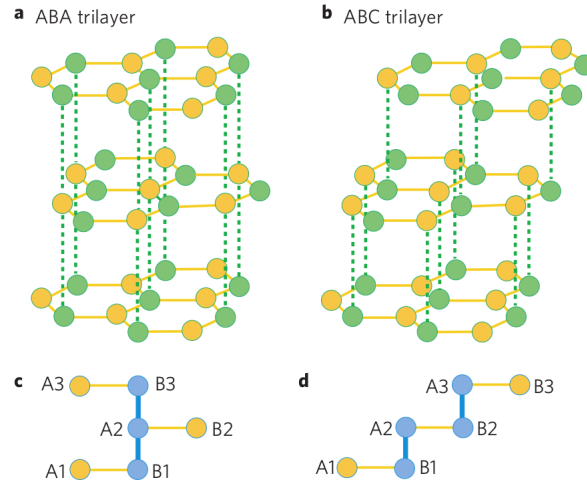


Figure 1.10: Trilayer graphene in configurations ABA (left) and ABC (right). Figure reproduced from [20].

1.2.3 Graphite

Graphite consists of several graphene layers packed in Bernal structure (ABABA...). Its primitive vectors are the same of graphene (eq. 1.1) plus one out of plane:

$$\vec{a}_1 = a \left(\frac{\sqrt{3}}{2}, \frac{1}{2}, 0 \right), \quad \vec{a}_2 = a \left(\frac{\sqrt{3}}{2}, -\frac{1}{2}, 0 \right), \quad \vec{a}_3 = (0, 0, c); \quad (1.6)$$

The c parameter is twice the interlayer distance in graphite.

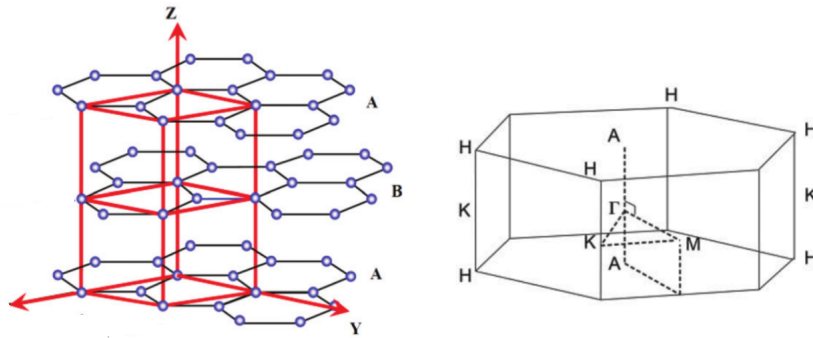


Figure 1.11: Graphite lattice structure (left) and first Brillouin zone and some high symmetry points. Figure adapted from [21].

Chapter 2

Methodology

2.1 Crystal Hamiltonian

We start by writing the non-relativistic hamiltonian of the system of many electrons and nuclei following [14,16]. It is composed by the kinetic energy and interactions among the particles. The electrons can be divided in core electrons and valence electrons. The core electrons are strongly bound to the nucleus and have little influence in chemical bonds. On the other hand, valence electrons belong to external shells and are responsible for chemical bonds. Therefore, the core electrons can be treated together with the nucleus as ions (see section 2.3.7) separately from the valence electrons.

The basic hamiltonian not including external potentials is given by:

$$H = H_{el} + H_{ion} + H_{el-ion}; \quad (2.1)$$

The first term in eq. 2.1 is given by:

$$H_{el} = -\frac{\hbar^2}{2m_e} \sum_i \nabla_i^2 + \frac{e^2}{4\pi\epsilon_0} \sum_{i>j} \frac{1}{|\vec{r}_i - \vec{r}_j|}; \quad (2.2)$$

The first part in eq. 2.2 is electronic kinetic energy and the second one is the Coulomb repulsion for each electronic pair. \hbar is the Planck's constant, m_e is the electron rest mass,

e is the electron charge and ϵ_0 is the vacuum permittivity. The i and j indices are labels of the electrons.

The second term in eq. 2.1 is given by:

$$H_{ion} = -\frac{\hbar^2}{2} \sum_A \frac{\nabla_A^2}{M_A} + \frac{e^2}{4\pi\epsilon_0} \sum_{A>B} \frac{Z_A Z_B}{|\vec{R}_A - \vec{R}_B|}; \quad (2.3)$$

The first part in eq. 2.3 is the kinetic energy of the ions and the second one is the potential energy for each pair of ions. M_I is the ion total mass, Z_I is the atomic number and the A and B indices are labels of the ions.

The last component of the hamiltonian is the interaction between ions and electrons.

$$H_{ion-el} = \sum_{i,A} V_{ion-el}(\vec{R}_A - \vec{r}_i); \quad (2.4)$$

The V_{ion-el} has not been written explicitly because the Coulomb interaction is altered by the screening of the atomic nucleus caused by core electrons.

In principle one could try to solve the Schrödinger equation:

$$H\Psi = E\Psi; \quad (2.5)$$

where $\Psi = \Psi(\{\vec{R}_A\}, \{\vec{r}_i\})$ is the full many-body wave-function, depending on the positions of all electrons and ions. However, eq. 2.5 can be solved analytically only for very simple cases. Therefore, we adopt a computational approach, on which a sequence of controlled approximations is employed.

2.2 Born-Oppenheimer approximation

The ratio between the mass of the electrons and nuclei is very small. This means that electrons respond faster than ions to forces between these two kinds of particles. Therefore, the movement of electrons and ions can be separated and the ions can be considered frozen when dealing with electron dynamics. In this point of view, the electrons respond

instantaneously to the movement of the ions, so one can solve eq. 2.5 for the electronic part considering the ions as fixed and its positions as parameters. This procedure is known as Born-Oppenheimer or adiabatic approximation [15, 16].

Firstly we can ignore H_{ion} as it depends only on the fixed ionic positions $\{\vec{R}\}$ and V_{ion-el} depends parametrically on $\{\vec{R}\}$. Therefore, we can write an equation for the electronic problem in the form

$$(H_{ion-el} + H_{el})\psi_\mu(\{\vec{r}\} : \{\vec{R}\}) = E_\mu^{el}(\{\vec{R}\})\psi_\mu(\{\vec{r}\} : \{\vec{R}\}); \quad (2.6)$$

where E_μ^{el} is the electronic eigenenergy that takes the ions positions as fixed parameters. The complete set of eigenfunctions $\{\psi_\mu\}$ can be used as a basis for the full wave-function $\Psi = \Psi(\{\vec{R}_A\}, \{\vec{r}_i\})$, solution of 2.5:

$$\Psi = \sum_\mu \chi_\mu(\{\vec{R}\})\psi_\mu(\{\vec{r}\} : \{\vec{R}\}); \quad (2.7)$$

where $\{\chi_\mu\}$ are the coefficients of the expansion that depend explicitly of $\{\vec{R}\}$.

The coupling between electrons and ions wave-functions is described by χ_μ . To find those functions, we need to insert eq. 2.7 in 2.5. Multiplying the resulting expression by $\psi_\mu^*(\{\vec{r}\}, \{\vec{R}\})$ and integrating over the electronic coordinates, one can obtain

$$\left[-\frac{\hbar^2}{2} \sum_A \frac{\nabla_A^2}{M_A} + \frac{e^2}{4\pi\epsilon_0} \sum_{A>B} \frac{Z_A Z_B}{|\vec{R}_A - \vec{R}_B|} + E_\mu^{el} - E \right] \chi_\mu(\{\vec{R}\}) = - \sum_\nu C_{\mu\nu} \chi_\nu(\{\vec{R}\}); \quad (2.8)$$

where $C_{\mu\nu} = A_{\mu\nu} + B_{\mu\nu}$ and

$$A_{\mu\nu} = \sum_A \frac{1}{M_A} \left\langle \psi_\mu(\{\vec{r}\} : \{\vec{R}\}) \left| \nabla_A \right| \psi_\nu(\{\vec{r}\} : \{\vec{R}\}) \right\rangle \nabla_A; \quad (2.9)$$

$$B_{\mu\nu} = \sum_A \frac{1}{2M_A} \left\langle \psi_\mu(\{\vec{r}\} : \{\vec{R}\}) \left| \nabla_A^2 \right| \psi_\nu(\{\vec{r}\} : \{\vec{R}\}) \right\rangle; \quad (2.10)$$

The Born-Oppenheimer approximation consists of ignoring the off-diagonal matrix element $C_{\mu\nu}$. It can be interpreted as if eqs. 2.9 and 2.10 are transition probabilities between electronic states due to the movement of the ions. By not considering the off-diagonal matrix elements such transitions are ignored and the movement of the ions is restricted to a single electronic energy surface $E_\mu^{el}(\{\vec{R}\})$. The diagonal terms can be treated easily. $A_{\mu\mu}$ is 0 and $B_{\mu\mu}$ can be grouped with $E_\mu^{el}(\{\vec{R}\})$ in order to generate a modified potential function for the ions $U_\mu(\{\vec{R}\}) = E_\mu^{el}(\{\vec{R}\}) + B_{\mu\mu}(\{\vec{R}\})$. In this approximation, the nuclear motion is described by:

$$\left[-\frac{\hbar^2}{2} \sum_A \frac{\nabla_A^2}{M_A} + \frac{e^2}{4\pi\epsilon_0} \sum_{A>B} \frac{Z_A Z_B}{|\vec{R}_A - \vec{R}_B|} + U_\mu(\{\vec{R}\}) - E_{\mu i} \right] \chi_{\mu i}(\{\vec{R}\}) = 0; \quad (2.11)$$

where the index i labels nuclear states. In summary, in the Born-Oppenheimer approximation the total wave function becomes

$$\Psi_{i\mu} = \chi_{\mu i}(\{\vec{R}\}) \psi_\mu(\{\vec{r}\} : \{\vec{R}\}); \quad (2.12)$$

where for a set of ionic positions $\{\vec{R}\}$ the equations 2.6 and 2.11 are obeyed.

Generally this is an excellent approximation except for the cases where there is degeneracy or near degeneracy of electronic states. Typical examples are metals, where there is no energy gap, or other materials with gap smaller than the typical energies for the motion of the ions.

Electron-phonon coupling plays a crucial role in phenomena like Raman scattering and superconductivity and results from the $C_{\mu\nu}$ off-diagonal terms. The dominant terms are given by eq. 2.9 and physically represent an electronic transition coupled with emission or absorption of one quantum of lattice vibrations, also known as a phonon.

2.3 Density Functional Theory (DFT)

We have separated the movements of ions and electrons in the last section, so now we can focus on the electronic problem.

2.3.1 Introduction

For a system of N electrons one would have to solve eq. 2.5 for a given set of ionic positions in the Born-Oppenheimer approximation. As this still is a many-body problem, it is analytical solvable only for very simple cases. Several methods have been developed in order to solve this problem, such as the Hartree-Fock and Configuration Interaction methods, extensively used in quantum chemistry community. However those methods are applicable only for a small number of atoms.

As explained in Walter Kohn's Nobel lecture [22] the Van Vleck catastrophe states: "In general the many-electron wave function $\psi(\vec{r}_1, \vec{r}_2, \dots, \vec{r}_N)$ for a system of N electrons is not a legitimate scientific concept, when $N > N_0$, where $N_0 \approx 10^3$ ". This statement is based on the fact that both the final numerical error and the amount of data needed to record the wave function increase exponentially with the number of atoms.

Instead of working with the complex many-electron wave-function, alternative methods were developed that work with the electronic density, a much simpler quantity. The electronic density in the state $\Psi(\vec{r}_1, \vec{r}_2, \dots)$ is defined by the following operator:

$$\hat{n}(\vec{r}) = \sum_{i=1}^N \delta(\vec{r} - \vec{r}_i); \quad (2.13)$$

where the label i indicates the electrons and δ is the Dirac delta function. The expectation value of the density operator is given by:

$$\begin{aligned} n(\vec{r}) &= \langle \Psi | \hat{n} | \Psi \rangle = \sum_i \int d\vec{r}_1 d\vec{r}_2 \dots, d\vec{r}_N \Psi^*(\vec{r}_1, \vec{r}_2, \dots, \vec{r}_N) \delta(\vec{r} - \vec{r}_i) \Psi(\vec{r}_1, \vec{r}_2, \dots, \vec{r}_N) \\ &= N \int d\vec{r}_2 \dots, d\vec{r}_N |\Psi(\vec{r}, \vec{r}_2, \dots, \vec{r}_N)|^2; \end{aligned} \quad (2.14)$$

We can also evaluate the expectation value of an external potential as an integral of the electronic density:

$$\begin{aligned}
\langle \psi | V_{ext} | \psi \rangle &= \int d^3r_1 d^3r_2 \dots d^3r_N \psi^*(r_1, r_2, \dots, r_N) \left[\sum_i V_{ext}(\vec{r}_i) \right] \psi(r_1, r_2, \dots, r_N) \\
&= \sum_i \int d^3r_i V_{ext}(\vec{r}_i) \int d^3r_1 \dots d^3r_{i-1} d^3r_{i+1} \dots d^3r_N |\psi(r_1, r_2, \dots, r_N)|^2 \\
&= N \int d^3r V_{ext}(\vec{r}) \int d^3r_2 d^3r_3 \dots d^3r_N |\psi(r, r_2, \dots, r_N)|^2 = \int d^3r V_{ext}(\vec{r}) n(\vec{r});
\end{aligned} \tag{2.15}$$

where we used eq. 2.14 and the fact that $V_{ext}(\vec{r})$ can be written as a sum of external potentials over each electron and the indistinguishability of electrons.

The Thomas-Fermi model was the first density functional method developed [23, 24]. In this model the total energy is written as a functional of electronic density in the form:

$$\begin{aligned}
E_{TF}[n] &= \frac{3}{10} \frac{\hbar^2}{m_e} (3\pi^2)^{2/3} \int d^3r n(\vec{r})^{5/3} + \int d^3r V_{ext}(\vec{r}) n(\vec{r}) \\
&\quad + \frac{1}{2} \frac{e^2}{4\pi\epsilon_0} \int d^3r \frac{n(\vec{r}') n(\vec{r})}{|\vec{r}' - \vec{r}|} - \frac{e^2}{4\pi\epsilon_0} \frac{3}{4} \left(\frac{3}{\pi} \right)^{1/3} \int d^3r n(\vec{r})^{4/3};
\end{aligned} \tag{2.16}$$

The first term is the kinetic energy within the ideal Fermi gas approximation. The second is the external potential for the electronic problem (V_{ion-el} included). The third is the classical Coulomb electronic repulsion (also known as Hartree energy) and the last one is the Dirac contribution including the exchange interaction for the ideal Fermi gas [15, 16].

The ground state density and energy can be found by minimizing the functional 2.16 for all possible $n(\vec{r})$ with the constraint on the total number of electrons

$$\int d^3r n(\vec{r}) = N; \tag{2.17}$$

Using Lagrange multipliers the solution can be found by minimizing the following functional

$$\Omega[n] = E_{TF}[n] - \mu \left[\int d^3\vec{r} n(\vec{r}) - N \right]; \quad (2.18)$$

where the Lagrange multiplier μ is the chemical potential (or Fermi energy for zero temperature). For small variations $\delta n(r)$ the condition for a stationary point is

$$\int d^3\vec{r} \left[\frac{\hbar^2}{m_e} \frac{1}{2} (3\pi^2)^{2/3} n(\vec{r})^{2/3} + v(\vec{r}) - \mu \right] \delta n(r) = 0; \quad (2.19)$$

where v corresponds to the functional derivative of the last three terms in 2.16 in respect to $n(\vec{r})$. Since 2.19 must be obeyed for any $\delta n(\vec{r})$, the expression inside the brackets must be equal to zero, resulting in a relation between the effective potential v and the density $n(\vec{r})$, known as Thomas-Fermi equation.

The use of density functional theory is attractive because it reduces a many-body problem that has $3N$ degrees of freedom for N electrons to a problem with 3 degrees of freedom, the spatial coordinates of the density. However the Thomas-Fermi approach shown above uses very simple assumptions and misses essential physical and chemical features, such as shell structures of atoms and molecular bonds.

2.3.2 The Hohenberg-Kohn theorems

Modern Density Functional Theory is based on two theorems proposed by Hohenberg and Kohn [25] that are very easily proved. We rewrite 2.6 as

$$(H_{ele} + V_{ext}(\vec{r})) \psi(\vec{r}_1, \vec{r}_2, \dots, \vec{r}_N) = E\psi(\vec{r}_1, \vec{r}_2, \dots, \vec{r}_N); \quad (2.20)$$

where H_{ele} is eq. 2.2 and V_{ext} is the potential due to the ions and other external potentials (electric field per example).

The first theorem is:

Theorem 1. *For any system of interacting particles in a external potential $V_{ext}(\vec{r})$, the potential $V_{ext}(\vec{r})$ is determined uniquely, except for a constant, by the ground state particle*

density $n_0(\vec{r})$

Proof. Suppose that for a given external potential V_{ext} the ground state is $|\psi\rangle$ and for another external potential V'_{ext} the ground state is $|\psi'\rangle$. Our assumption is that both V_{ext} and V'_{ext} give the same electronic density $n_0(\vec{r})$. By the variational principle, the ground state energies E and E' for each potential satisfy

$$E = \langle \psi | H_{el} + V_{ext} | \psi \rangle < \langle \psi' | H_{el} + V_{ext} | \psi' \rangle; \quad (2.21)$$

$$E' = \langle \psi' | H_{el} + V'_{ext} | \psi' \rangle < \langle \psi | H_{el} + V'_{ext} | \psi \rangle; \quad (2.22)$$

Adding and subtracting $\langle \psi' | V'_{ext} | \psi' \rangle$ in the inequality 2.21 we get:

$$\begin{aligned} E &< \langle \psi' | H_{el} + V_{ext} + V'_{ext} - V'_{ext} | \psi' \rangle \\ E &< \langle \psi' | H_{el} + V'_{ext} | \psi' \rangle + \langle \psi' | V_{ext} - V'_{ext} | \psi' \rangle \\ E &< E' + \int d^3r (V_{ext} - V'_{ext}) n_0(\vec{r}); \end{aligned} \quad (2.23)$$

where in the second step we have used 2.22 and 2.15. Repeating the procedure for E' in 2.22 we get

$$E' < E + \int d^3r (V'_{ext} - V_{ext}) n_0(\vec{r}); \quad (2.24)$$

summing 2.23 and 2.24 we have

$$E + E' < E' + E, \quad (2.25)$$

which is absurd. Since we have assumed the same density $n_0(\vec{r})$ for $V_{ext} \neq V'_{ext}$, we conclude that this assumption is incorrect, thus proving the theorem.

□

The second theorem is:

Theorem 2. *A universal functional for the energy $E[n]$ in terms of the density $n(\vec{r})$ can be defined, valid for any external potential $V_{ext}(\vec{r})$. For any particular $V_{ext}(\vec{r})$, the exact ground state energy of the system is the global minimum value of this functional, and the density $n(\vec{r})$ that minimizes that functional is the exact ground state density $n_0(\vec{r})$*

Proof. We can write the total energy as a functional of the density

$$E[n] = \langle \psi | H_{ele} + V_{ext} | \psi \rangle = F[n] + \langle \psi | V_{ext} | \psi \rangle ; \quad (2.26)$$

where $F[n]$ is an unknown universal functional and $\langle \psi | V_{ext} | \psi \rangle$ depends on the system.

In particular for the ground state

$$E[n_0] = \langle \psi_0 | H_{ele} + V_{ext} | \psi_0 \rangle = F[n_0] + \langle \psi_0 | V_{ext} | \psi_0 \rangle ; \quad (2.27)$$

Using the variational principle and assuming $n \neq n_0$

$$\begin{aligned} E[\psi_0] &< E[\psi] \\ \langle \psi_0 | H_{ele} + V_{ext} | \psi_0 \rangle &< \langle \psi | H_{ele} + V_{ext} | \psi \rangle \\ F[n_0] + \langle \psi_0 | V_{ext} | \psi_0 \rangle &< F[n] + \langle \psi | V_{ext} | \psi \rangle \\ E[n_0] &< E[n]; \end{aligned} \quad (2.28)$$

In conclusion, there is a variational principle valid the electronic density as there is one for the wave-function.

□

The Hohenberg-Kohn theorems describe an exact many-body theory expressing the energy of the system as a functional of the electronic density. However it does not tell us anything about how this electronic density functional is constructed or how to solve the problem. For this, the Kohn-Sham ansatz is needed.

2.3.3 The Kohn-Sham equations

Following the Hartree-Fock approach, the Kohn-Sham ansatz [26] aims to reduce the interacting many-body problem to several one body problems in the presence of an effective potential. It assumes that the exact ground state density can be represented by the density of an auxiliary system of non-interacting particles and the auxiliary hamiltonian is chosen to have the usual kinetic energy operator and an effective local potential. The density of the non-interacting system is

$$n(\vec{r}) = \sum_i |\psi_i(\vec{r})|^2; \quad (2.29)$$

where ψ_i are single-particle states. The auxiliary hamiltonian

$$H_{aux} = -\frac{\hbar^2}{2m_e} \nabla^2 + V_{eff}(\vec{r}); \quad (2.30)$$

The independent-particle kinetic energy is given by

$$T_s = -\frac{\hbar^2}{2m_e} \sum_i \langle \psi_i | \nabla^2 | \psi_i \rangle; \quad (2.31)$$

The classical electronic coulomb interaction is given by the Hartree term

$$H_{Hartree}[n] = \frac{1}{2} \frac{e^2}{4\pi\epsilon_0} \int d^3r d^3r' \frac{n(\vec{r})n(\vec{r}')}{|\vec{r} - \vec{r}'|}; \quad (2.32)$$

The Kohn-Sham approach is to rewrite the Hohenberg-Kohn expression 2.26 as

$$E_{KS} = T_s[n] + H_{Hartree}[n] + \int d^3r V_{ext}(\vec{r})n(\vec{r}) + E_{xc}[n]; \quad (2.33)$$

where the new term E_{xc} , the exchange-correlation energy, includes all the exchange and the so-called correlation effects. Comparing 2.26 and 2.33 we can see that

$$E_{xc}[n] = F[n] - (T_s[n] + E_{Hartree}[n]); \quad (2.34)$$

or more explicitly with $\langle T \rangle$ and $\langle V_{int} \rangle$ being the mean kinetic energy and mean internal energy respectively

$$E_{xc}[n] = \langle T \rangle - T_s[n] + \langle V_{int} \rangle - E_{Hartree}[n]; \quad (2.35)$$

The last equation shows that E_{xc} is just the difference of the kinetic and internal energies of the true many-body system from those auxiliary independent-particle system. If the exact E_{xc} were known then the exact ground state energy and density of the many-body problem could be found by minimizing the functional 2.33 with the constraint 2.17.

Following the approach of Thomas-Fermi, one should minimize 2.33 with respect to the electronic density. Since T_s is a functional of the single-electron orbitals, which are functionals of density themselves, and all the other terms are functionals of density explicitly, we can minimize the total energy functional E_{KS} with respect to any given orbital ψ_i^* and use the chain rule for $n(\vec{r})$.

$$\frac{\delta E_{KS}}{\delta \psi_i^*(\vec{r})} = \frac{\delta T_s}{\delta \psi_i^*(\vec{r})} + \left[\frac{\delta E_{ext}}{\delta n(\vec{r})} + \frac{\delta E_{Hartree}}{\delta n(\vec{r})} + \frac{\delta E_{xc}}{\delta n(\vec{r})} \right] \frac{\delta n(\vec{r})}{\delta \psi_i^*(\vec{r})} = 0; \quad (2.36)$$

with the orthonormalization condition

$$\langle \psi_i | \psi_j \rangle = \delta_{i,j}. \quad (2.37)$$

From 2.31:

$$\frac{\delta T_s}{\delta \psi_i^*(\vec{r})} = -\frac{\hbar^2}{2m_e} \nabla^2 \psi_i; \quad (2.38)$$

and from 2.29:

$$\frac{\delta n(\vec{r})}{\delta \psi_i^*} = \psi_i. \quad (2.39)$$

By using the Lagrange multiplier method, we get the Kohn-Sham equations

$$(H_{KS} - \varepsilon_i)\psi_i = 0, \quad (2.40)$$

where ε_i are the eigenvalues and H_{KS} is the effective hamiltonian, given by

$$H_{KS} = -\frac{\hbar^2}{2m_e}\nabla^2 + V_{KS}, \quad (2.41)$$

in which the Kohn-Sham potential is given by

$$V_{KS} = V_{ext} + \frac{\delta E_{Hartree}}{\delta n(\vec{r})} + \frac{\delta E_{xc}}{\delta n(\vec{r})}; \quad (2.42)$$

As one can see from above, to solve the Kohn-Sham equations 2.40 one needs to know the ground state electronic density in order to construct the functionals in 2.33 and the associated potentials in 2.42. In other words, the potentials depend on the solutions of the equations. To overcome this problem, the KS equations are solved in a self-consistent fashion: one starts with a initial guess for $n(\vec{r})$, solves the Kohn-Sham equations, calculates the new density from the solutions $\{\psi_i\}$ and repeats the same steps until convergence is achieved, as illustrated in Fig. 2.1.

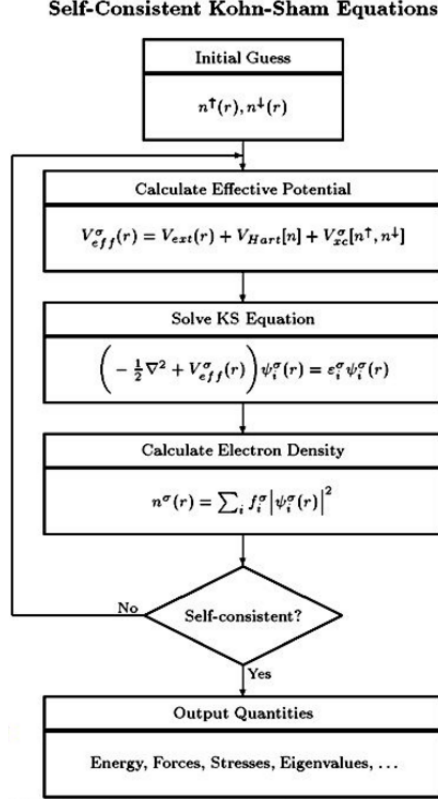


Figure 2.1: Schematic algorithm to solve self-consistently the Kohn-Sham equations. The σ index indicates the spin degree of freedom, which is not discussed in this work. Figure reproduced from [16].

2.3.4 Exchange-Correlation functional

In the Kohn-Sham approach, as the independent-particle kinetic-energy and the long-range Hartree terms are separated out, the remaining exchange-correlation functional can be approximated by a local or semilocal functional of the density. The exchange-correlation functional can be expressed as

$$E_{xc}[n] = \int d\vec{r} n(\vec{r}) \varepsilon_{xc}([n], \vec{r}); \quad (2.43)$$

where $\varepsilon_{xc}([n], \vec{r})$ is the exchange-correlation energy per electron at \vec{r} that depends on the electronic density $n(\vec{r})$.

The exchange-correlation potential is given by

$$V_{xc} = \frac{\delta E_{xc}[n]}{\delta n(\vec{r})} = \varepsilon_{xc}([n], \vec{r}) + n(\vec{r}) \frac{\delta \varepsilon_{xc}([n], \vec{r})}{\delta n(\vec{r})}; \quad (2.44)$$

The DFT in the KS is exact except by the exchange-correlation that is not known analytically. Several approximations to $E_{xc}[n]$ have been developed in order to pursue the "divine" functional as explained in [27, 28]. In this work, we will only discuss the Local Density and Generalized Gradient Approximations (LDA and GGA, respectively), which are the most widely used in Condensed Matter Physics, and some non-local van der Waals corrections (see chapter 2.4.1). There are another functionals as meta-GGA and hybrid functionals that are extensively used in the literature. For a comparison of several functionals, see [29, 30]

LDA (Local Density Approximation)

The LDA approximation consists in assuming that the exchange-correlation energy density is the same as in a homogeneous electron gas with the same electron density at a given point

$$E_{xc}^{LDA}[n] = \int d^3r n(\vec{r}) \varepsilon_{xc}^{hom}(n(\vec{r})) = \int d^3r n(\vec{r}) (\varepsilon_x^{hom}(n(\vec{r})) + \varepsilon_c^{hom}(n(\vec{r}))); \quad (2.45)$$

One can also separate the correlation and exchange effects. For a homogeneous gas the exchange term is given by [15]

$$\varepsilon_x^{hom}[n] = -\frac{e^2}{4\pi\epsilon_0} \frac{3}{4} \left(\frac{3}{\pi}\right)^{1/3} \int d^3r n(\vec{r})^{4/3}; \quad (2.46)$$

The correlation energy has been calculated with quantum Monte Carlo methods and fitted to analytical expressions in the form of $\varepsilon_c(r_s)$, where r_s is the Wigner-Seitz radius [12] and represents the radius of a sphere whose volume is equal to the mean volume occupied by one electron in a solid and is given by

$$r_s = \left(\frac{3}{4\pi n} \right)^{1/3}; \quad (2.47)$$

The $r_s < a_0$ ¹ regime is considered the high-density limit and $r_s \geq a_0$ is the low-density limit. Since r_s is a function of the density $n(\vec{r})$, it is straightforward to write $\varepsilon(r_s)$ as a functional of the density.

In this work we used the PZ (Perdew-Zunger) [31] LDA exchange-correlation functional. Its expression for the correlation energy density is

$$\varepsilon_c(r_s) = \begin{cases} \frac{\gamma}{(1+\beta_1\sqrt{r_s}+\beta_2r_s)}, & r_s \geq a_0 \\ A\ln(r_s) + B + Cr_s\ln(r_s) + Dr_s, & r_s < a_0 \end{cases} \quad (2.48)$$

The numerical values of the constants in the expression above can be found in [31] and in the Appendix B of [16].

GGA (Generalized Gradient Approximation)

In the GGA approximation, $\varepsilon_{xc}(n(\vec{r}))$ is also a function of the absolute value of the gradient of density $|\vec{\nabla}n(\vec{r})|$. As $n(\vec{r})$ varies strongly in real materials it is convenient to define

$$\begin{aligned} E_{xc}^{GGA}[n] &= \int d^3r n(\vec{r}) \varepsilon_{xc}(n, |\vec{\nabla}n|) \\ &= \int d^3r n(\vec{r}) \varepsilon_x^{hom}[n] F_{xc}(n, |\vec{\nabla}n|); \end{aligned} \quad (2.49)$$

where ε_x^{hom} is given by 2.46 and F_{xc} is a dimensionless function. It is natural to work with the dimensionless reduced density gradient that is defined as

$$s_m = \frac{|\nabla^m n|}{(2k_F)^m n}; \quad (2.50)$$

where $k_F = 3(2\pi/3)^{1/3}r_s^{-1}$.

In this work we use a PBE (Perdew-Burke-Ernzerhof) functional within the GGA approximation [32]. The expressions for the correlation and exchange functionals are

¹ a_0 is Bohr radius. $a_0 = 0.529\text{\AA}$

somewhat lengthy and can be found in [16, 32]. In general, GGA functionals give better results for binding energies than LDA, however we have found in this work that, for graphite the interlayer distance is better reproduced by a LDA functional (see fig. 3.3).

Both LDA and GGA approaches have some deficiencies, as for example the self-interaction. This happens because the approximated exchange interaction does not cancel the exact Hartree interaction when $\vec{r} \approx \vec{r}'$ in eq. 2.32. In the Hartree-Fock approach, this cancellation occurs because the exchange interactions are included in exact form [16].

2.3.5 Plane-waves

Once we have defined the exchange-correlation functional in Kohn-Sham approach we face the problem of solving the one-electron eqs. 2.40.

In crystals the $V_{ion-ele}$ potential has the same periodicity of the Bravais lattice. Mathematically

$$V_{ion-ele}(\vec{r} + \vec{R}) = V_{ion-ele}(\vec{r}); \quad (2.51)$$

where \vec{R} is a vector of the Bravais lattice. Since $V_{ion-ele}$ has this property, the electronic density must have the same periodicity and so does the Kohn-Sham (KS) potential (eq. 2.42).

As the KS equations (eq. 2.40) are one-electron equations and the KS potential is periodic, the KS orbitals obey Bloch's theorem [12–15] and the wave function can be written as

$$\psi_{n\vec{k}} = e^{i\vec{r}\cdot\vec{k}} u_{n\vec{k}}(\vec{r}); \quad (2.52)$$

where $u_{i\vec{k}}(\vec{r})$ is a function with the same periodicity of the lattice, n is the band index and \vec{k} is a vector in the first Brillouin zone (BZ) and the quantity $\hbar\vec{k}$ is known as crystal momentum because the wave function 2.52 is not an eigenstate of the momentum operator $\vec{p} = (\hbar/i)\vec{\nabla}$ making p not a good quantum number.

As $u_{n\vec{k}}$ is a periodic function, one can expand it in a plane wave function basis that only contains vectors of the reciprocal lattice

$$u_{n\vec{k}}(\vec{r}) = \sum_{\vec{G}} c_{n\vec{k}\vec{G}} e^{i\vec{G}\cdot\vec{r}}; \quad (2.53)$$

where \vec{G} is a vector of the reciprocal lattice. In the same way one can expand the periodic KS potential as

$$V_{KS}(\vec{r}) = \sum_{\vec{G}'} V_{\vec{G}'} e^{i\vec{G}'\cdot\vec{r}}; \quad (2.54)$$

Using expressions 2.52, 2.53 and 2.54 in equation 2.40, we get the following expression for the $c_{n\vec{k}\vec{G}}$ coefficients

$$\frac{\hbar^2}{2m} \sum_{\vec{G}} c_{n\vec{k}\vec{G}} (k + G)^2 e^{i\vec{G}\cdot\vec{r}} + \sum_{\vec{G}} \sum_{\vec{G}'} V_{\vec{G}'} c_{n\vec{k}\vec{G}} e^{i(\vec{G}'+\vec{G})\cdot\vec{r}} = \varepsilon_{n\vec{k}} \sum_{\vec{G}} c_{n\vec{k}\vec{G}} e^{i\vec{G}\cdot\vec{r}}; \quad (2.55)$$

Applying the bra $\langle e^{i\vec{G}''\cdot\vec{r}} |$ and using the orthonormalization condition $\langle e^{i\vec{G}''\cdot\vec{r}} | e^{i\vec{G}\cdot\vec{r}} \rangle = \delta_{\vec{G}'',\vec{G}}$ we get the central equation

$$\left(\frac{\hbar^2}{2m} (k + G'')^2 - \varepsilon_{n\vec{k}} \right) c_{n\vec{k}\vec{G}''} + \sum_{\vec{G}} c_{n\vec{k}\vec{G}} V_{\vec{G}''-\vec{G}} = 0; \quad (2.56)$$

By solving the eq. 2.56, one can obtain the eigenvalues $\varepsilon_{n\vec{k}}$ and the coefficients $c_{n\vec{k}\vec{G}}$ to construct the eigenfunction 2.52. The term $V_{\vec{G}''-\vec{G}}$ couples the coefficients $c_{n\vec{k}\vec{G}''}$ and $c_{n\vec{k}\vec{G}}$, making it impossible to find a general analytic solution.

If both the function $u_{n\vec{k}}$ and the KS potential are sufficiently smooth, the plane-wave expansions 2.53 and 2.54 can be truncated with a relatively small number of plane waves. The typical parameter used in the DFT context is the cutoff energy, defined as

$$E_c = \frac{\hbar^2}{2m} G^2; \quad (2.57)$$

The E_c value define the maximum magnitude of the \vec{G} s vectors in the plane-wave expansions.

The more localized the function $u_{n\vec{k}}$ and the KS potential are, more plane waves are necessary, thus increasing the computational cost of the calculation. In such cases, other basis sets might be more adequate, such as an atomic-like orbital basis, which we do not discuss in this work.

2.3.6 \vec{K} -point sampling

Evaluation of many quantities, such as energy, density of states and response functions, requires integration over the BZ. The mean value of an arbitrary quantity $f(\vec{k})$ is given by [16, 17]

$$\bar{f} = \frac{1}{N} \sum_{\vec{k} \in BZ} f(\vec{k}) = \frac{\Omega_{cell}}{(2\pi)^d} \int_{BZ} d^d k f(\vec{k}); \quad (2.58)$$

where Ω_{cell} is the unit cell volume in real space and d is the dimension.

If the function $f(\vec{k})$ is periodic in reciprocal space, one can expand it in a plane wave basis that contains only the vectors \vec{R} of the real space lattice, analogously in 2.53 and 2.54

$$f(\vec{k}) = \sum_{\vec{R}} \tilde{f}(\vec{R}) e^{i\vec{k}\vec{R}}; \quad (2.59)$$

To avoid an integration over the BZ, integrals are approximated by summations over an appropriated set of k points.

One first simplification is to take advantage of the point group symmetries of the crystal, reducing the summation over the BZ to a summation over the irreducible Brillouin zone (IBZ) [59]. For the summation over the IBZ each k point is associated to a weight function $\omega_{\vec{k}}$ that is the total of k points related to a given k point in the IBZ divided by the total of points N

$$\bar{f} = \frac{1}{N} \sum_{\vec{k} \in BZ} f(\vec{k}) = \frac{1}{N} \sum_{\vec{k} \in IBZ} \omega_{\vec{k}} f(\vec{k}); \quad (2.60)$$

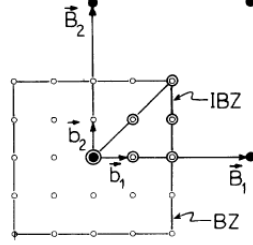


Figure 2.2: Representation of the BZ and IBZ of a square lattice. Figure reproduced from [59].

The method proposed by Monkhorst and Pack (MP) [58] is the most widely used method because it generates an uniform set of points using the following expression

$$\vec{k}_{n_1, n_2, n_3} = \sum_i^3 \frac{2n_i - N_i - 1}{2N_i} \vec{G}_i; \quad (2.61)$$

where N_i is the number of unit cells in the direction i and $n_i = 1, 2, \dots, N_i$. One of the main advantages of the MP method is that it reproduces exactly the mean value of f when the expansion 2.59 is truncated in a finite mesh $N_1 \times N_2 \times N_3$ of vectors of the real lattice.

2.3.7 Pseudopotentials

As explained in the beginning of this chapter, one can separate the electrons in valence and core electrons, because the core electrons are not substantially affected when the atoms form a solid or a molecule. The pseudopotential method transforms the Coulomb potential ($\sim r^{-1}$) into a smoother function for the valence electrons (see fig. 2.3) in the core region. By doing that, valence electrons that vary very quickly in the core region (as they are orthogonal to core electrons) becomes smoother functions in the core region but maintain their properties in the valence region. This procedure reduces the number of plane-waves necessary to describe the valence electrons and the V_{ion-el} potential 2.4.

In this section we describe the Phillips-Kleinman pseudopotential [16,60], which is the first pseudopotential proposed in the literature. Although it is not used any longer in practical calculations, it shares many of the properties of present-day pseudopotentials.

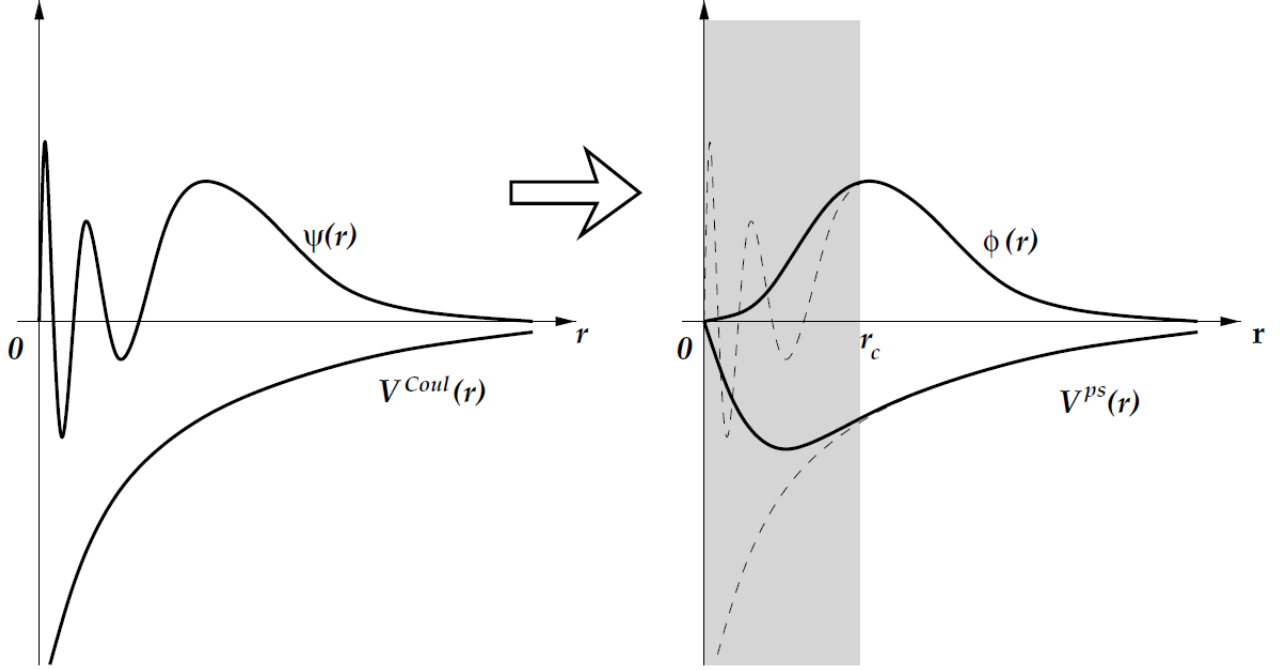


Figure 2.3: Schematic representation of the pseudopotential method in order to make the wave function smoother. Figure reproduced from [17].

For a given isolated atom we have the following eigenstates of the hamiltonian

$$H |\psi_i^c\rangle = \varepsilon_i^c |\psi_i^c\rangle \quad (2.62a)$$

$$H |\psi_{i'}^v\rangle = \varepsilon_{i'}^v |\psi_{i'}^v\rangle; \quad (2.62b)$$

where ψ_i^c is an eigenstate of a core electron and $\psi_{i'}^v$ is a valence electron. One can define a new set of valence states $\tilde{\phi}_{i'}^v$ that obey the following relation

$$|\psi_{i'}^v\rangle = |\tilde{\phi}_{i'}^v\rangle - \sum_i \langle \psi_i^c | \tilde{\phi}_{i'}^v \rangle |\psi_i^c\rangle, \quad (2.63)$$

which preserves the orthogonality condition $\langle \psi_{i'}^v | \psi_i^c \rangle = 0$. Using this expression in 2.62b we get

$$H \left[\left| \tilde{\phi}_{i'}^v \right\rangle - \sum_i \langle \psi_i^c | \tilde{\phi}_{i'}^v \rangle | \psi_i^c \rangle \right] = \varepsilon_{i'}^v \left[\left| \tilde{\phi}_{i'}^v \right\rangle - \sum_i \langle \psi_i^c | \tilde{\phi}_{i'}^v \rangle | \psi_i^c \rangle \right]; \quad (2.64)$$

By using eq. 2.62a we get

$$\left[H + \sum_i (\varepsilon_{i'}^v - \varepsilon_i^c) | \psi_i^c \rangle \langle \psi_i^c | \right] \left| \tilde{\phi}_{i'}^v \right\rangle = \varepsilon_{i'}^v \left| \tilde{\phi}_{i'}^v \right\rangle; \quad (2.65)$$

It is possible to see that the new states $\tilde{\phi}_{i'}^v$, also called pseudostates, obey a Schrödinger equation with the same eigenenergy of $\psi_{i'}^v$, but with a modified potential

$$V^{ps} = V + \sum_i (\varepsilon_{i'}^v - \varepsilon_i^c) | \psi_i^c \rangle \langle \psi_i^c |; \quad (2.66)$$

where V is the original (bare) potential and V^{ps} is the pseudopotential.

The additional term in 2.66 is repulsive as the valence states have greater energy than core states. Thus, this term is repulsive and tends to screen the attractive Coulomb potential from the nucleus. As it is composed by the projector of core states $\sum_i | \psi_i^c \rangle \langle \psi_i^c |$ this repulsive term acts more near the nucleus where the core states are localized and far from the nucleus the influence of the core states becomes smaller and the Coulomb potential is recovered.

One can notice that the pseudostates are not unique. By adding a linear combination of core states into it, eq. 2.63 remains unchanged. There are many possible pseudofunctions and pseudopotentials that obey eqs. 2.65. It is desirable to create a pseudopotential that is smooth near the nucleus and that represents well the Coulomb potential from the nucleus at long distances. The smoother is the wavefunction, the smaller is the number of plane waves necessary to reproduce it. For a more extensive review of the subject see [16] chapter 11.

2.4 Van der Waals interactions

Van der Waals (VDW) interactions are non-bonded interactions that are weaker than bonded and Coulomb interactions and whose range of distance is of the order of a few nanometers. Friction, surface tension, viscosity, adhesion, cohesion, wetting and capillarity are some of the phenomena related to VDW interactions [36–42]. Also known as dispersion interactions, VDW interactions are caused by the long range correlation of electrons.

VDW interactions are composed of three different interactions, all proportional to r^{-6} , where r is the distance between the atoms or molecules.

The first one is the Keesom interaction. This term represents the mean attractive interaction between two permanent dipoles and is temperature dependent [43]. It is given by

$$U_{Keesom} = -\frac{\vec{\mu}_1 \cdot \vec{\mu}_2}{3(4\pi\epsilon_0\epsilon)^2 k_B T r^6} = -\frac{C_{Keesom}}{r^6}; \quad (2.67)$$

where μ_i is the dipole moment of molecule (or atom) i , ϵ_0 is the vacuum permittivity, ϵ is dielectric constant of the surrounding, k_B is the Boltzmann constant and T is the temperature.

The second one is the Debye interaction. This term is due to the interaction of a permanent dipole with a induced dipole by the influence of the permanent dipole. It is given by

$$U_{Debye} = -\frac{\mu_1^2 \alpha_{02}}{(4\pi\epsilon_0\epsilon)^2 r^6} = -\frac{C_{Debye}}{r^6}; \quad (2.68)$$

where α_{02} is the dipole polarizability of the second atom or molecule.

The last term is the London interaction. This term is due to the interaction between two induced dipoles. It is caused by random fluctuations in the electronic density of a atom or a molecule generating an instantaneous dipole that induces a dipole in other

atom or molecule. It is given by

$$U_{London} = -\frac{3}{2} \frac{\alpha_{01}\alpha_{02}}{(4\pi\epsilon_0\epsilon)^2 r^6} \frac{I_1 I_2}{I_1 + I_2} = -\frac{C_{London}}{r^6}; \quad (2.69)$$

where α_{0i} is the dipole polarizability of the atom (or molecule) i and I_i is the first ionization potential.

The complete VDW interaction is thus given by

$$U_{VDW} = -\frac{(C_{London} + C_{Debye} + C_{Keesom})}{r^6} = -\frac{C_{VDW}}{r^6}; \quad (2.70)$$

The VDW interactions have some general properties [44, 45] as they are long-range interactions that range from 0.2 to 10nm, do not only attract molecules but tend to align them and are no additive as the surrounding affects the interactions of the molecules by changing their polarizabilities.

2.4.1 Van der Waals on DFT

As LDA is a local functional and GGA is a semilocal one the van der Waals interactions are not well described in those approximations as it consists on correlation in long range distances. Those interactions are of substantial importance for, 2D materials, biomolecules and liquids just to name a few systems.

In this section we describe the VDW corrections used in this work

DFT-D

The DFT-D correction [55, 56] is an empirical dispersion energy is added to the total energy

$$E_{disp} = -s_6 \sum_{i=1}^N \sum_{j=i+1}^N \frac{C_6^{ij}}{r_{ij}^6} f_{damp}(r_{ij}); \quad (2.71)$$

where C_6^{ij} denotes the dispersion coefficient for atom pair ij and s_6 is a global scaling factor that depends on the exchange-correlation functional used. To avoid singularities for small r_{ij} a damping function is used

$$f_{damp}(r_{ij}) = \frac{1}{1 - e^{-d(r_{ij}/r_r-1)}}; \quad (2.72)$$

where r_r is the sum of the atomic VDW radii.

For transferability purposes, the C_6^{ij} is parametrized for a pair with the same atomic species. For dimers with different atoms i and j the C_6^{ij} is given by the geometric mean of the individual coefficients.

VDW-DF

The vdw-df [46–48] is an exchange-correlation functional based in the adiabatic connection fluctuation-dissipation theorem (ACFDT) [49]. It is expressed as

$$E_{xc}[n(\vec{r})] = E_x^{GGA}[n(\vec{r})] + E_c^{LDA}[n(\vec{r})] + E_c^{nl}[n(\vec{r})]; \quad (2.73)$$

where the first terms is the rev-PBE GGA [50], the second is the PW correlation [51] and the last one is the non-local contribution given by

$$E_c^{nl}[n(\vec{r})] = \frac{1}{2} \int \int d^3r_1 d^3r_2 n(\vec{r}_1) n(\vec{r}_2) \phi(q_1, q_2, r_{12}); \quad (2.74)$$

where $r_{12} = |\vec{r}_1 - \vec{r}_2|$ and q_1, q_2 are values of a universal function $q_0[n(\vec{r}), |\nabla n(\vec{r})|]$, evaluated at \vec{r}_1 and \vec{r}_2 . The kernel ϕ has an universal form that depends on $q_1 \vec{r}_1$ and $q_2 \vec{r}_2$ that has to do to local response. Details of ϕ and q_0 can be found in [46, 47].

VDW-DF2

The differences from vdw-df2 [53] to vdw-df are that the exchange functional revPBE is replaced by the PW86 [52], with the motivation that revPBE is generally too repulsive

near the equilibrium separation, and a different approach is used to determine the kernel ϕ [53]. While it gives better results for intermolecular interactions, its behavior for asymptotic distances becomes worse compared to vdw-df [41].

VDW-DF-C09

The C09 correction [54] is an exchange functional created to work with the vdw-df functional by replacing the first term in eq. 2.73. In eq. 2.49 the $F_x(s)$ is chosen to be quadratic for small s and to reproduce the revPBE for large s as is shown in fig. 2.4.

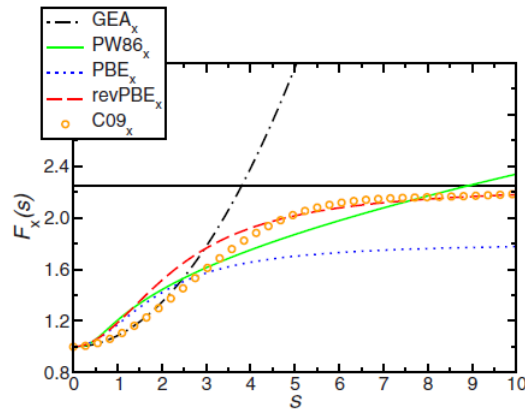


Figure 2.4: F_x for various GGA_x functionals. Figure reproduced from [54].

In fig. 2.5, it is possible to see that for a benzene sandwich dimer vdw-df2 improves the equilibrium distance in relation to vdw-df, but over-estimates the binding energy. Vdw-df-c09 corrects the overbinding and preserves the correct equilibrium distance.

VDW-DF2-C09

The vdw-df2-c09 functional is the vdw-df2 functional described above with the C09 exchange. As reported in [57], vdw-df2-c09 gives better results in general for adsorption of graphene on metal surfaces.

²Coupled Cluster method. For a quick introduction see [15]. S, D and T mean Single, Double and Triple substitution, respectively

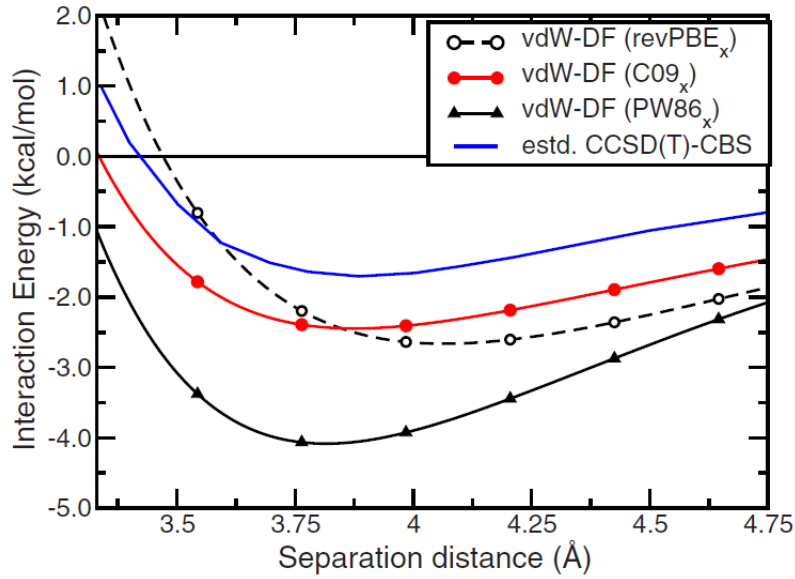


Figure 2.5: Performance of vdW-DF (open circles), vdW-DF (black triangles), vdW-DF-c09 (red circles) and CCSD(T)²(blue line) compared for the interaction energy for benzene sandwich dimer. Figure reproduced from [54].

2.5 Crystalline vibrations

Crystalline vibrations are of substantial importance for the understanding of matter. At finite temperature the atoms in solids or molecules vibrate around their equilibrium positions [12, 17, 62, 63] and these vibrations can be understood in terms of normal modes of ionic movement. The excitation of those normal modes is called phonons. A wide variety of physical properties of solids depend on phonons: infrared, Raman, and neutron-diffraction spectra; specific heats, thermal expansion, and heat conduction; and phenomena related to the electron-phonon interaction such as the resistivity of metals and superconductivity.

2.5.1 Dynamical Matrix

To study the lattice dynamics first we introduce the set of atomic positions described by

$$\vec{r}_{\vec{R},\vec{\tau}} = \vec{R} + \vec{\tau} + \vec{u}_{\vec{R},\vec{\tau}}; \quad (2.75)$$

where \vec{R} is the origin of the unit cell, $\vec{\tau}$ is the equilibrium position of an atom that composes the basis of the Bravais lattice and $\vec{u}_{\vec{R},\vec{\tau}}$ is its displacement from $\vec{R} + \vec{\tau}$.

The potential 2.11 for the ions depends only on the set of atomic positions $\{\vec{r}_{\vec{R},\vec{\tau}}\}$ and it is minimum when $\{\vec{r}_{\vec{R},\vec{\tau}}\} = \{\vec{R} + \vec{\tau}\}$. Assuming that the displacements $\{\vec{u}_{\vec{R},\vec{\tau}}\}$ are small compared to the interatomic distance one can expand the potential in a Taylor series

$$U(\{\vec{r}_{\vec{R},\vec{\tau}}\}) \approx U(\{\vec{R}\}) + (\vec{u} \cdot \vec{\nabla})U|_{\{\vec{r}_{\vec{R},\vec{\tau}}\}=\{\vec{R}\}} + \frac{1}{2}(\vec{u} \cdot \vec{\nabla})^2 U|_{\{\vec{r}_{\vec{R},\vec{\tau}}\}=\{\vec{R}\}} + O(u^3); \quad (2.76)$$

where we have introduced the matrix notation

$$\vec{u} = \begin{bmatrix} u_{1,1,x} \\ u_{1,1,y} \\ u_{1,1,z} \\ \vdots \\ u_{\vec{R},\vec{\tau}} \\ \vdots \\ u_{N,\gamma,x} \\ u_{N,\gamma,y} \\ u_{N,\gamma,z} \end{bmatrix}; \quad (2.77)$$

and the $\vec{\nabla}$ operator represents

$$\vec{\nabla} = \begin{bmatrix} \frac{\partial}{\partial x_{1,1}} \\ \frac{\partial}{\partial y_{1,1}} \\ \frac{\partial}{\partial z_{1,1}} \\ \vdots \\ \frac{\partial}{\partial \hat{n}_{\vec{R},\vec{\tau}}} \\ \vdots \\ \frac{\partial}{\partial x_{N,\gamma}} \\ \frac{\partial}{\partial y_{N,\gamma}} \\ \frac{\partial}{\partial z_{N,\gamma}} \end{bmatrix}; \quad (2.78)$$

where N is the total number of unit cells, γ the total number of atoms of the basis and we introduced the notation $u_{\vec{R},\vec{\tau}}$ where the index τ absorbs the directions of displacement, in other words, it describes a given atom of the basis moving in a given direction. This

procedure is called the harmonic approximation because eq. 2.76 is truncated at the quadratic term, in analogy to the harmonic oscillator.

The first term in the 2.76 is the equilibrium energy and we can take it to be zero. The second one is a term proportional to the first multidimensional derivative of the potential and, as the expansion occurs around the minimum of the potential, this term is zero.

The third term is given by

$$\begin{aligned} \frac{1}{2}(\vec{u} \cdot \vec{\nabla})^2 U &= \frac{1}{2} \left(u_{1,1,x} \frac{\partial}{\partial x_{1,1}} + \dots + u_{N,\gamma,z} \frac{\partial}{\partial z_{N,\gamma}} \right) \left(u_{1,1,x} \frac{\partial}{\partial x_{1,1}} + \dots + u_{N,\gamma,z} \frac{\partial}{\partial z_{N,\gamma}} \right) U \\ &= \frac{1}{2} \sum_{\nu=1}^{3N\gamma} \sum_{\mu=1}^{3N\gamma} u_{\mu} \frac{\partial^2 U}{\partial u_{\mu} \partial u_{\nu}} u_{\nu}; \end{aligned} \quad (2.79)$$

where the indices μ and ν represent the which unit cell, atom of the base and direction of displacement and $N\gamma$ is the total of atoms.

In matrix notation, it can be written as $\frac{1}{2} \mathbf{u}^T \Phi \mathbf{u}$, where Φ is known as a Hessian matrix or Force Constant Matrix (FCM)

$$\Phi = \begin{bmatrix} \frac{\partial^2 U}{\partial u_1 \partial u_1} & \cdots & \frac{\partial^2 U}{\partial u_1 \partial u_{3N\gamma}} \\ \vdots & \ddots & \vdots \\ \frac{\partial^2 U}{\partial u_{3N\gamma} \partial u_1} & \cdots & \frac{\partial^2 U}{\partial u_{3N\gamma} \partial u_{3N\gamma}} \end{bmatrix}; \quad (2.80)$$

Each term $\Phi_{\mu\nu}$ in the FCM represents a constant of spring that connects the pair of atom/direction μ and ν .

Forces over all atoms can also be represented by a $3N\gamma$ vector as 2.77. The force component \hat{n} over the atom $(\vec{R}, \vec{\tau})$ represented by the index μ is given by

$$F_{\mu} = -(\Phi \mathbf{u})_{\mu} = - \sum_{\nu} \frac{\partial^2 U}{\partial u_{\nu} \partial u_{\mu}} u_{\nu}; \quad (2.81)$$

or particularly, if in a crystal one atom/direction has the infinitesimal displacement δu_{μ} the atom/direction ν will be sense a force $\delta F_{\nu} = -\Phi_{\nu\mu} \delta u_{\mu}$. To construct the FCM, one

only needs to apply infinitesimal displacements and measure the forces components of all atoms.

The FCM has 2 key properties

- Φ is a symmetric matrix. This happens because one can change the order in the mixed derivatives

$$\Phi_{\nu\mu} = \frac{\partial^2 U}{\partial u_\nu \partial u_\mu} \Big|_{\{\vec{r}\}=\{\vec{R}+\vec{\tau}\}} = \frac{\partial^2 U}{\partial u_\mu \partial u_\nu} \Big|_{\{\vec{r}\}=\{\vec{R}+\vec{\tau}\}} = \Phi_{\mu\nu}; \quad (2.82)$$

- The sum of all elements over a line (or a column) is zero. This is a consequence of the fact that if every ion moves with the same displacement, there will not be any internal distortions and forces in the crystal.

Once defined the FCM, to study the dynamics of ions we need to write $3N\gamma$ equations of motion.

$$M_\tau \ddot{u}_{\vec{R},\tau} = - \sum_{\vec{R}',\vec{\tau}'} \Phi_{\vec{R}'\vec{\tau}',\vec{R}\vec{\tau}} u_{\vec{R}',\vec{\tau}'}; \quad (2.83)$$

or in matrix notation

$$M\ddot{\mathbf{u}} = -\Phi\mathbf{u}; \quad (2.84)$$

where M is the mass matrix, a diagonal matrix with the elements $M_{\mu\mu}$ represents the mass of the ion μ , and $\ddot{\mathbf{u}}$ is the second derivative in time of \mathbf{u} .

To solve eq. 2.83 we can use the following *ansatz*

$$u_{\vec{R},\vec{\tau}} = \frac{1}{\sqrt{M_\tau}} \hat{\epsilon}_\tau(\vec{k}) e^{i[\vec{k}\cdot\vec{R}-\omega t]}; \quad (2.85)$$

where $\hat{\epsilon}_\tau$ is the polarization vector of the normal mode that describes the direction in which the ions move. This means that every (τ) ion/direction have a displacement $\hat{\epsilon}_\tau$ and that equivalent ions separated by a lattice vector \vec{R} oscillate with a phase shift $e^{i\vec{k}\cdot\vec{R}}$

Using Born-von Karman Periodic Boundary Conditions (PBC) we restrict the \vec{k} to be in the first BZ [12]. The translation of k to the real space is the wavelength $\lambda = 2\pi/k$ that indicates the length of the periodicity of a vibration. As k is in the BZ, its smaller magnitude is 0 ($\lambda \rightarrow \infty$) and greater when it is lying over the edge of the BZ ($\lambda \rightarrow$ the order of lattice parameter)

Using the *ansatz* 2.85 in 2.83, one gets

$$\omega^2(\vec{k})\hat{\epsilon}_{\vec{\tau}}(\vec{k}) = \sum_{\vec{\tau}} \left[\sum_{\vec{R}'} \frac{\Phi_{\vec{\tau}\vec{R},\vec{\tau}'\vec{R}'} e^{i\vec{k}\cdot(\vec{R}'-\vec{R})}}{\sqrt{M_{\vec{\tau}}M_{\vec{\tau}'}}} \right] \hat{\epsilon}_{\vec{\tau}'}(\vec{k}), \quad (2.86)$$

in matrix notation

$$\omega^2(\vec{k})\hat{\epsilon}(\vec{k}) = D(\vec{k})\hat{\epsilon}(\vec{k}); \quad (2.87)$$

$D(\vec{k})$ is known as the dynamical matrix. Its elements are given by

$$D_{\vec{\tau}\vec{\tau}'}(\vec{k}) = \frac{1}{\sqrt{M_{\vec{\tau}}M_{\vec{\tau}'}}} \left[\sum_{\vec{R}'} \Phi_{\vec{\tau}\vec{R},\vec{\tau}'\vec{R}'} e^{i\vec{k}\cdot(\vec{R}'-\vec{R})} \right]; \quad (2.88)$$

As one can notice Φ is a $3N\gamma \times 3N\gamma$ matrix while D is a $3\gamma \times 3\gamma$ matrix that is easily diagonalizable. The problem is completely defined. To find the frequencies and modes of vibration of a crystal, one must solve the eigenvalue eq. 2.87 for each \vec{k} , finding the dispersion relation $\omega(\vec{k})$.

As there are γ atoms per unit cell, there will be $3(\gamma - 1)$ optical and 3 acoustic branches. The 3 acoustical branches have zero frequency at the Γ point and, in general, for small k their frequencies depends linearly on k with the sound velocity as constant of proportionality. The 3 acoustical branches are called LA (Longitudinal Acoustic), when the polarization vector is parallel to the wave vector \vec{k} and TA (transverse acoustic), when the polarization vector is perpendicular to LA displacements. The optical branches are also classified as LO (Longitudinal Acoustic) or TO (Transverse Acoustic) using the same rule. An example of phonon dispersion curve is shown in fig. 2.6.

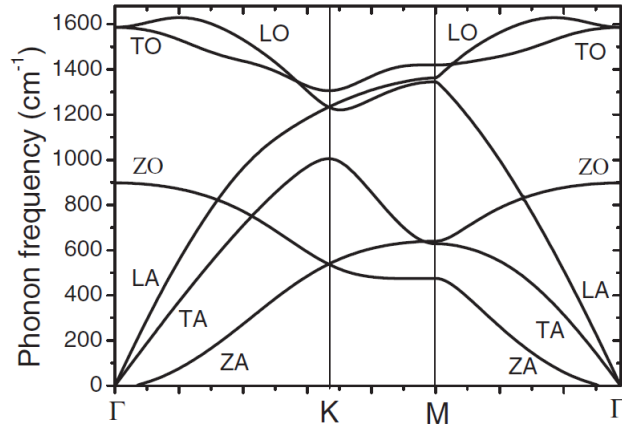


Figure 2.6: Phonon dispersion of graphene. As it has 2 atoms per unit cell there will be 6 branches. In graphene context the ZO and ZA branches indicate out-of-plane modes. Figure reproduced from [64].

2.5.2 Forces on DFT

Once we have discussed how to construct the dynamical matrix, one needs to know how to measure forces on ions in the DFT context. To solve this problem we can make use of the Hellman-Feynman theorem [15, 16]

One can consider that a hamiltonian, H , depends on a parameter λ , where λ may represent the ionic coordinates as, for example, in the KS hamiltonian (eq. 2.41). The eigenvalues and eigenstates of $H(\lambda)$ also depend on λ .

Theorem 3. *Starting with the eigenvalue problem*

$$H(\lambda) |\Psi(\lambda)\rangle = E(\lambda) |\Psi(\lambda)\rangle; \quad (2.89)$$

with

$$E(\lambda) = \langle \Psi | H(\lambda) | \Psi \rangle; \quad (2.90)$$

Deriving both sides of 2.90 in respect to λ and using 2.89

$$\begin{aligned}
\frac{dE(\lambda)}{d\lambda} &= \left\langle \Psi \left| \frac{dH(\lambda)}{d\lambda} \right| \Psi \right\rangle + E(\lambda) \left(\left\langle \frac{d\Psi(\lambda)}{d\lambda} \left| \Psi \right\rangle + \left\langle \Psi \left| \frac{d\Psi(\lambda)}{d\lambda} \right\rangle \right) \right) \\
&= \left\langle \Psi \left| \frac{dH(\lambda)}{d\lambda} \right| \Psi \right\rangle + E(\lambda) \frac{d\langle \Psi | \Psi \rangle}{d\lambda};
\end{aligned} \tag{2.91}$$

as $\langle \Psi | \Psi \rangle$ is constant, the last derivative is 0.

The final Hellmann-Feynman expression is

$$\frac{dE(\lambda)}{d\lambda} = \left\langle \Psi \left| \frac{dH(\lambda)}{d\lambda} \right| \Psi \right\rangle; \tag{2.92}$$

In the DFT context the total energy is given by

$$\begin{aligned}
E[n] &= -\frac{\hbar^2}{2m} \sum_i \left\langle \Psi_i \left| \vec{\nabla}^2 \right| \Psi_i \right\rangle + \frac{1}{2} \frac{e^2}{4\pi\epsilon_0} \int \int d^3r d^3r' \frac{n(\vec{r})n(\vec{r}')}{|\vec{r} - \vec{r}'|} - \int d^3r V_{el-ion} n(\vec{r}) \\
&\quad + \frac{e^2}{4\pi\epsilon_0} \sum_{A < B} \frac{Z_A Z_B}{|\vec{R}_A - \vec{R}_B|} + \int d^3r \epsilon_{xc}[n(\vec{r})] n(\vec{r});
\end{aligned} \tag{2.93}$$

One can derive this expression with respect to a certain position \vec{R}_μ of ion μ with charge $Z_\mu e$. If one uses the correct ground state density, the force on ion μ is

$$\vec{F}_\mu = -Z_\mu \frac{e^2}{4\pi\epsilon_0} \left(\frac{\partial}{\partial \vec{R}_\mu} \sum_{A \neq \mu} \frac{Z_A}{|\vec{R}_A - \vec{R}_\mu|} - \int d^3r n(\vec{r}) \frac{\partial}{\partial \vec{R}_\mu} \frac{1}{|\vec{r} - \vec{R}_\mu|} \right); \tag{2.94}$$

For a complete derivation of eq. 2.94, see [15] section 6.7

2.6 Calculation of Phonon Spectra

2.6.1 Frozen Phonon

The frozen-phonon is a direct approach [16, 63, 65]. One can apply infinitesimal displacements corresponding to the normal modes, by knowing them previously, and measure the second derivative of the energy variation to get the frequency associated with this mode.

A given eigenvector ε_α of the dynamical matrix $D(\vec{k})$ obeys

$$D(\vec{k})\varepsilon_\alpha = \omega_\alpha^2 \varepsilon_\alpha; \quad (2.95)$$

and this eigenvector is given by

$$\vec{\varepsilon} = \begin{bmatrix} \varepsilon_1 \\ \varepsilon_2 \\ \vdots \\ \varepsilon_{\vec{\tau}} \\ \vdots \\ \varepsilon_{3\gamma} \end{bmatrix}; \quad (2.96)$$

Applying ε_α^T and using eq. 2.88

$$\begin{aligned} \varepsilon_\alpha^T D(\vec{k}) \varepsilon_\alpha &= \varepsilon_\alpha^T \omega_\alpha^2 \varepsilon_\alpha \\ \sum_{\vec{\tau}} \sum_{\vec{\tau}'} \varepsilon_{\vec{\tau}} D_{\vec{\tau}, \vec{\tau}'}(\vec{k}) \varepsilon_{\vec{\tau}'} &= \omega_\alpha^2 \|\varepsilon_\alpha\|^2 = \omega^2 \sum_{\vec{\tau}} |\varepsilon_{\vec{\tau}}|^2; \end{aligned} \quad (2.97)$$

where $\|\varepsilon_\alpha\|$ is the modulus of vector ε_α

On the other hand, if we want to evaluate the energy variation for a given displacement u , using the *ansatz* 2.85 in the quadratic term of 2.76 we get

$$\begin{aligned} u^T \Phi u &= \sum_{\mu} \sum_{\nu} u_{\mu} \Phi_{\mu\nu} u_{\nu} \\ &= \sum_{\vec{R}\vec{\tau}} \sum_{\vec{R}'\vec{\tau}'} \varepsilon_{\vec{\tau}} \frac{\Phi_{\vec{R}\vec{\tau}, \vec{R}'\vec{\tau}'} e^{i\vec{k} \cdot (\vec{R}' - \vec{R})}}{\sqrt{M_{\vec{\tau}} M_{\vec{\tau}'}}} \varepsilon_{\vec{\tau}'} \\ &= \sum_{\vec{\tau}} \sum_{\vec{\tau}'} \sum_{\vec{R}'} \sum_{\vec{R}} \varepsilon_{\vec{\tau}} \frac{\Phi_{\vec{R}\vec{\tau}, \vec{R}'\vec{\tau}'} e^{i\vec{k} \cdot (\vec{R}' - \vec{R})}}{\sqrt{M_{\vec{\tau}} M_{\vec{\tau}'}}} \varepsilon_{\vec{\tau}'} \\ &= N \sum_{\vec{\tau}} \sum_{\vec{\tau}'} \varepsilon_{\vec{\tau}} \left[\sum_{\vec{R}'} \frac{\Phi_{\vec{0}\vec{\tau}, (\vec{R}' - \vec{R})\vec{\tau}'} e^{i\vec{k} \cdot \vec{R}'}}{\sqrt{M_{\vec{\tau}} M_{\vec{\tau}'}}} \right] \varepsilon_{\vec{\tau}'} \\ &= N \sum_{\vec{\tau}} \sum_{\vec{\tau}'} \varepsilon_{\vec{\tau}} D_{\vec{\tau}\vec{\tau}'} \varepsilon_{\vec{\tau}'} = N \varepsilon^T D \varepsilon; \end{aligned} \quad (2.98)$$

where N is the total of unit cells in the crystal and we used the translational symmetry of the crystal in the first summation. If ε is chosen to be an eigenvector 2.97, the 2.76 becomes

$$U \approx U_0 + \frac{N\omega_\alpha^2}{2} \|\varepsilon_\alpha\|^2; \quad (2.99)$$

We can relate $\|\varepsilon_\alpha\|$ to $\|u_\alpha\|$, which is easier to work with. By the *ansatz* 2.85, the $3N\gamma$ length u vector relates to the ϵ , 3γ length vector, by

$$u = \begin{bmatrix} u_1 \\ u_2 \\ \vdots \\ u_{3\gamma} \\ u_{3\gamma+1} \\ \vdots \\ u_{3(N-1)\gamma+1} \\ \vdots \\ u_{3N\gamma} \end{bmatrix} = \begin{bmatrix} \epsilon_1 e^{i\vec{k} \cdot \vec{R}_1} / M_1^{1/2} \\ \epsilon_2 e^{i\vec{k} \cdot \vec{R}_1} / M_2^{1/2} \\ \vdots \\ \epsilon_{3\gamma} e^{i\vec{k} \cdot \vec{R}_1} / M_{3\gamma}^{1/2} \\ \epsilon_1 e^{i\vec{k} \cdot \vec{R}_2} / M_1^{1/2} \\ \vdots \\ \epsilon_1 e^{i\vec{k} \cdot \vec{R}_N} / M_1^{1/2} \\ \vdots \\ \epsilon_{3\gamma} e^{i\vec{k} \cdot \vec{R}_N} / M_{3\gamma}^{1/2} \end{bmatrix} \quad (2.100)$$

The norm of u is given by

$$\|u_\alpha\|^2 = N \sum_{\vec{\tau}} \frac{|\epsilon_{\vec{\tau}}|^2}{M_{\vec{\tau}}}; \quad (2.101)$$

in the particular case of $M_{\vec{\tau}} = M$ and supposing we are working with an eigenvector ε_α

$$\|u_\alpha\|^2 = \frac{N}{M} \sum_{\vec{\tau}} |\epsilon_{\vec{\tau}}|^2 = \frac{N}{M} \|\varepsilon_\alpha\|^2; \quad (2.102)$$

combining the above expression with 2.99

$$U \approx U_0 + \frac{M\omega_\alpha^2}{2} \|u_\alpha\|^2; \quad (2.103)$$

One can create a curve of energy as function of $\|u_\alpha\|$ and from that obtain the respective frequency. For more applications, see section 3.3.3

2.6.2 Finite Difference Method

This method consist on to apply a displacement δu_ν over an atom in a certain direction and measure the forces components δF_μ on all atoms of the unitary cell in order to construct

the FCM

$$\Phi_{\mu\nu} \approx -\frac{\delta F_\mu}{\delta u_\nu}; \quad (2.104)$$

For the frozen phonon and finite difference method one can make use of group theory to find symmetries in the Φ matrix related to the point group symmetries of the crystal or the eigenvectors [66,67]. For studies at the Γ point, one only needs to study one unit cell, as since $k = 0$ means that in eq. 2.85 all equivalent atoms from different unit cells have the same displacement. For studies at points $\vec{k} \neq 0$ one needs the supercell approximation, in which a cell with size of the order of the wavelength $\lambda = 2\pi/k$ is chosen, since the periodicity of vibrations in real space is equal to λ ³.

2.6.3 Density Functional Perturbation Theory (DFPT)

To evaluate the the force constant matrix element $\Phi_{\mu\nu}$ (eq. 2.80), one can derive the force F_μ (eq. 2.94) with respect to the position \vec{R}_ν ⁴ [61]

$$\begin{aligned} \Phi_{\mu\nu} &= \frac{\partial^2 U}{\partial \vec{r}_\mu \partial \vec{r}_\nu} = -\frac{\partial F_\mu}{\partial u_\nu} \\ &= Z_\mu \frac{e^2}{4\pi\epsilon_0} \left(\frac{\partial^2}{\partial \vec{R}_\mu \partial \vec{R}_\nu} \sum_{A \neq \mu} \frac{Z_A}{|\vec{R}_A - \vec{R}_\mu|} - \int d^3r n(\vec{r}) \frac{\partial^2}{\partial \vec{R}_\mu \partial \vec{R}_\nu} \frac{1}{|\vec{r} - \vec{R}_\mu|} - \int d^3r \frac{\partial n(\vec{r})}{\partial \vec{R}_\nu} \frac{\partial}{\partial \vec{R}_\mu} \frac{1}{|\vec{r} - \vec{R}_\mu|} \right); \end{aligned} \quad (2.105)$$

To obtain the force constant $\Phi_{\mu\nu}$ from eq. 2.105 one needs the ground state density and the linear response to a distortion of the nuclear geometry $\partial n(\vec{r})/\partial \vec{R}_\nu$.

We can generalize the eq. 2.105 by replacing the ionic coordinates by the parameters λ_i , which can represent the positions of ions or external electric fields. The mixed second derivative of the energy is given by

³In eq. 2.85 for $k \neq 0$ the phase shift between two u vectors is $e^{2\pi i(\vec{R}_\mu - \vec{R}_\nu)/\lambda}$

⁴In this section we adopt that $\{\vec{R}_\nu\}$ represents a general set of atomic positions (not necessarily the ground-state) for the simplification of the notation

$$\frac{\partial^2 E}{\partial \lambda_i \partial \lambda_j} = \frac{\partial^2 V_{ion-ion}}{\partial \lambda_i \partial \lambda_j} + \int d^3 r n(\vec{r}) \frac{\partial^2 V_{ext}}{\partial \lambda_i \partial \lambda_j} + \int d^3 r \frac{\partial n(\vec{r})}{\partial \lambda_i} \frac{\partial V_{ext}}{\partial \lambda_j}; \quad (2.106)$$

where $V_{ion-ion}$ is the ionic Coulomb interaction (second term in eq. 2.3) and V in our case is the interaction of the electronic density with the ions as in the second part of 2.105 but can include also other external agents.

To evaluate the derivative $\partial n(\vec{r})/\partial \lambda_i$ one can linearize the independent particle density (eq. 2.29)

$$\Delta^\lambda n = 2Re \sum_i \psi_i^*(\vec{r}) \Delta^\lambda \psi_i(\vec{r}); \quad (2.107)$$

where the ψ_i are the solutions to the KS problem (eqs. 2.40) and the Δ^λ operator is defined as

$$\Delta^\lambda f \equiv \sum_i \frac{\partial f}{\partial \lambda_i} \Delta \lambda_i; \quad (2.108)$$

using first order perturbation theory

$$(H_{KS} - \epsilon_i) |\Delta \psi_i\rangle = -(\Delta V_{KS} - \Delta \epsilon_i) |\psi_i\rangle; \quad (2.109)$$

where V_{KS} is the KS potential (eq. 2.42), $\Delta \epsilon_i = \langle \psi_i | \Delta V_{KS} | \psi_i \rangle$ and ΔV_{KS} is the first-order correction to the self-consistent potential

$$\Delta V_{KS} = \Delta V_{ext} + \Delta V_{Hartree} + \Delta V_{xc}; \quad (2.110)$$

and the above terms depend on the perturbed electronic density (eq. 2.107). The perturbed wave-function is

$$\Delta \psi_i(\vec{r}) = \sum_{i \neq j} \psi_j \frac{\langle \psi_j | \Delta V_{KS} | \psi_i \rangle}{\epsilon_i - \epsilon_j}; \quad (2.111)$$

Equations 2.107 and 2.109 form a set of self-consistent equations analogous to the KS problem, in which the eigenvalue problem is replaced with a linear system. The right side of 2.109 couples equations with different indices i making the solution of this linear system costfull. Several improvements to deal with this problem can be found in [61].

Chapter 3

Results and Discussion

3.1 Technical Details

All DFT calculations were done with the Quantum Espresso package [68]. For all materials (graphite, graphene and multilayer graphene), in the plane wave approximation (section 2.3.5), a cutoff energy of 60Ry was used. For integrations over the BZ, a Monkhorst-Pack mesh [58] was used for k -point sampling (section 2.3.6). For graphite a $8 \times 8 \times 8$ grid was used and for graphene and multilayer graphene a $8 \times 8 \times 1$ grid was used.

In this work, we compared the performance of GGA and LDA approximations with and without the DFT-D corrections [55, 56] and the vdw-df [46–48] and vdw-df2 [53] functionals with and without the c09 correction [54] (for a brief description see section 2.4.1). For GGA we used the PBE exchange-correlation functional [32] and for LDA we used the PZ functional [31]. We used the RRKJ ultrasoft pseudopotentials [70] with non-linear core correction [69] ¹.

The atomic positions of graphite and graphene were relaxed with convergence threshold on forces of 10^{-3} Ry/bohr and on energy of 10^{-4} Ry and multilayer graphene structures were relaxed with a convergence threshold on forces of 10^{-5} Ry/bohr and on energy of

¹For details on pseudopotential generation see <http://www.quantum-espresso.org/wp-content/uploads/Doc/pseudo-gen.pdf>

10^{-4} Ry. The convergence threshold for selfconsistency field (SCF) calculations for the KS equations is 10^{-10} Ry (Fig. 2.1). A vacuum slab of 15\AA for graphene and multilayer graphene was inserted in the direction perpendicular to the graphene sheets.

3.2 Lattice and Elastic Constants

3.2.1 Graphene

For graphene, only LDA and GGA functionals with no VDW corrections were used as it consists of a single graphene sheet.

To obtain the equilibrium lattice parameter for graphene, we evaluated its total energy for a set of lattice parameters and fitted the corresponding values to a two-dimensional Murnaghan equation [73]

$$E(A) = E_0 + B_0 A_0 \left[\frac{1}{B'_0(B'_0 - 1)} \left(\frac{A}{A_0} \right)^{1-B'_0} + \frac{1}{B'_0} \frac{A}{A_0} - \frac{1}{B'_0 - 1} \right]; \quad (3.1)$$

where $A = a^2\sqrt{3}/2$ is the area of the unit cell, A_0 is the ground state area of the unit cell, E_0 is the ground state energy, B_0 is the two-dimensional bulk modulus and $B'_0 = (\partial B/\partial P)|_{B=B_0}$, where $P = \partial E/\partial A$ is the two-dimensional pressure (surface tension).

In fig. 3.1 the Murnaghan fit is compared to a harmonic fit, showing that the curve $E(A)$ for graphene is not symmetric with respect to its minimum.

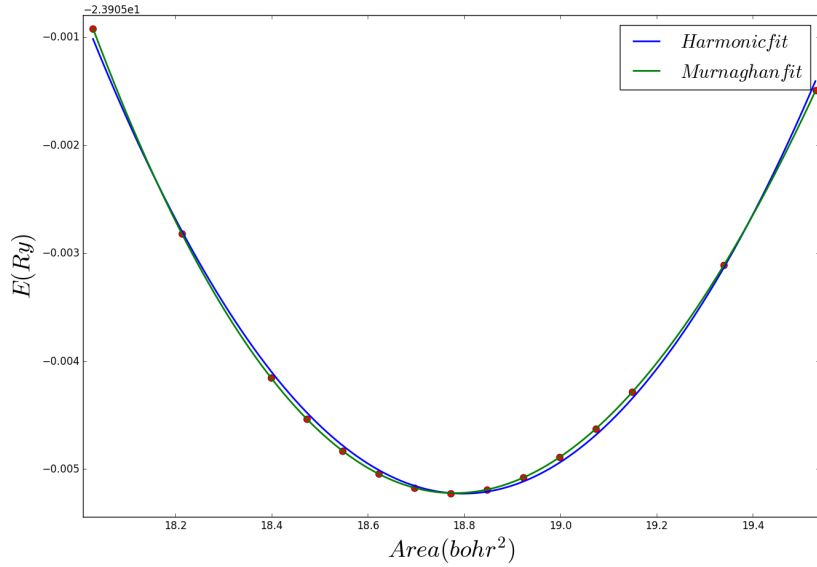


Figure 3.1: Murnaghan fit (eq. 3.1) for $E(A)$. Harmonic fit is presented for comparison

The Poisson ratio for graphene was obtained in the same way as for graphite (figs. 3.9, 3.10 and 3.11). As there is no experimental value of the Poisson ratio of graphene, it can be estimated to be the same as the in plane Poisson ratio of graphite [74]. Several theoretical works found values in the range 0.125 – 0.456 [75, 76].

The knowledge of the bulk modulus B_0 and the poisson ratio ν allows one to evaluate other elastic constants for graphene [77]. The Lamé coefficients λ and μ are related to λ and ν through

$$B_0 = \lambda + \mu; \quad (3.2)$$

$$\nu = \frac{\lambda}{2\mu + \lambda}; \quad (3.3)$$

The evaluated elastic constants for graphene are summarized in the table 3.1. For the poisson ratio ν in the above equations the mean of ν_{xy} and ν_{yx} was used.

Table 3.1: Some physical parameters of graphene

	GGA	LDA	Experimental value	Other theoretical works
$a(\text{\AA})$	2.4642	2.4457	2.461 [71]	2.4619 [71]
$B_0(N/m)$	207.41	216.53	-	203.31(0K) [83], 200 [84] 206.6 [85]
B'_0	4.40623	4.3496	-	4.33 [85]
ν_{xy}	0.16775	0.17644	0.165 [72]	0.125 – 0.456 [75, 76]
ν_{yx}	0.16881	0.17317	0.165 [72]	0.125 – 0.456 [75, 76]
$\lambda(N/m)$	29.87	32.22	-	52.06(0K) [83]
$\mu(N/m)$	147.65	152.09	-	151.25(0K) [83]

3.2.2 Graphite

The relaxed structural parameters for graphite for each functional we considered are shown in figs. 3.2 and 3.3. For the in plane lattice parameter a it is possible to see that GGA, GGA with dft-d correction, vdw-df-c09 and vdw-df2-c09 give the best results, although the other cases present variations about 0.02\AA only. For the out of plane lattice parameter c , which is twice the interlayer distance, LDA and vdw-df2-c09 have better results and GGA gives the worst result.

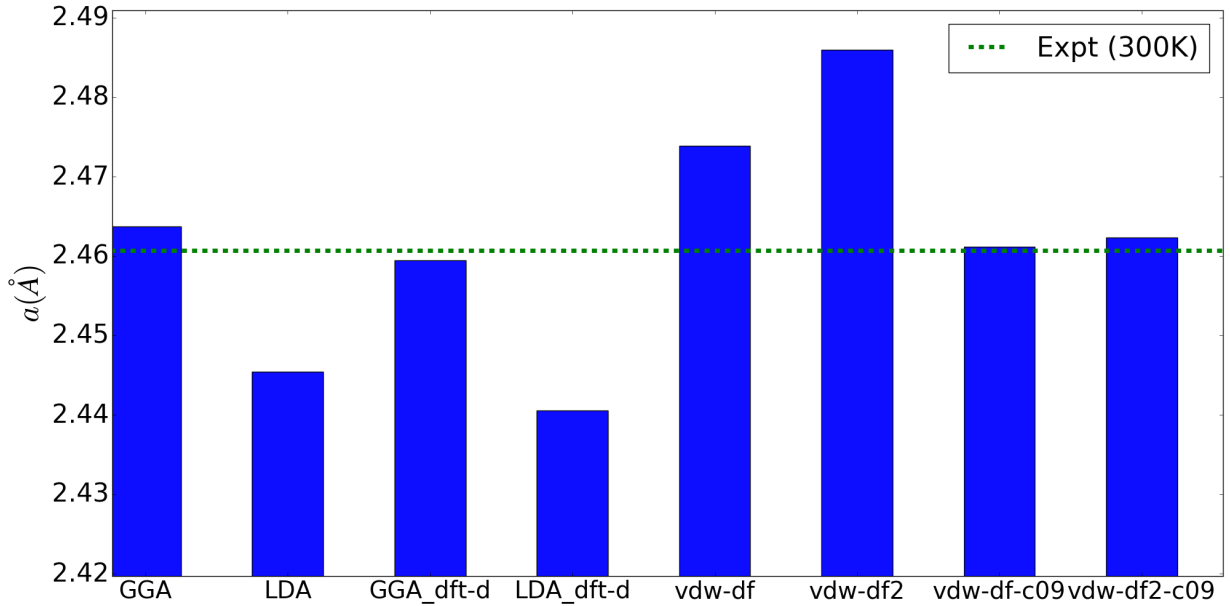


Figure 3.2: Comparison of the performance of several functionals for the a lattice constant. The experimental value is 2.4607\AA [71]

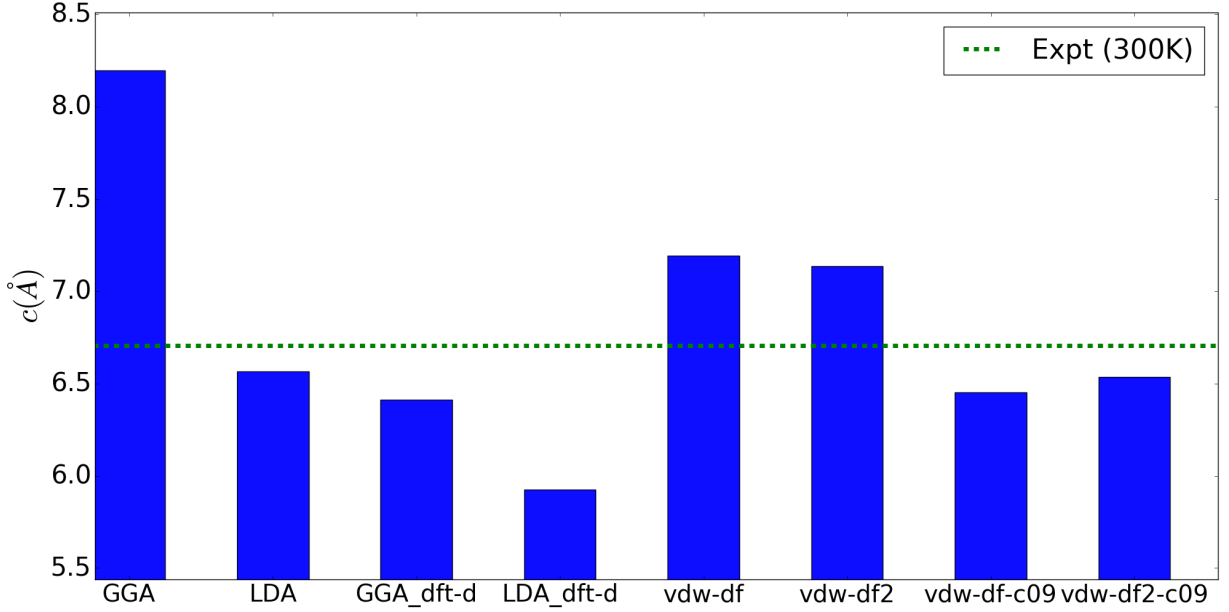


Figure 3.3: Comparison of the performance of several functionals for the c lattice constant. The experimental value is 6.7053\AA [71]

According to the elasticity theory, elastic constants are related to second derivatives of the energy evaluated in the ground-state. In the case of graphite one can obtain the following elastic constants [71]

$$\begin{aligned}
C_{11} + C_{12} &= \frac{1}{\sqrt{3}c_0} \frac{\partial^2 E}{\partial a^2} \\
C_{33} &= \frac{2c_0}{\sqrt{3}a_0^2} \frac{\partial^2 E}{\partial c^2} \\
C_{13} &= \frac{1}{\sqrt{3}a_0} \frac{\partial^2 E}{\partial a \partial c} \\
C_t &= \frac{1}{6} [(C_{11} + C_{12}) + 2C_{33} - 4C_{13}] \\
B_0 &= \frac{C_{33}(C_{11} + C_{12}) - 2C_{13}^2}{6C_t},
\end{aligned} \tag{3.4}$$

where C_{ij} are stiffness coefficients, C_t is the tetragonal shear modulus and B_0 is the bulk modulus. To evaluate the derivatives on the equations above the total energy was evaluated in SCF calculations for a set of (a, c) points around the equilibrium parameters obtained by the minimizations. The data was fitted by a fourth-order two-dimensional Taylor series. To evaluate the elastic constants 3.4 we used the relaxed parameters (figs.

3.2 and 3.3) and the experimental ones [71] for the values a_0 and c_0 .

For $C_{11} + C_{12}$, the use of experimental values for a_0 and c_0 improves the results, as shown in Fig. 3.4. This means that the second derivative $\partial^2 E / \partial a^2$ is well evaluated. One can compare fig. 3.3 and fig. 3.4 and realize that functionals that have c parameter smaller (higher) than the experimental value present higher (smaller) values for $C_{11} + C_{12}$ what comes from due to the $1/c_0$ factor in eq. 3.4. For C_{33} the use of experimental values gives better results for LDA, vdw-df-c09 and vdw-df2-c09 functionals as shown in Fig. 3.5. For C_{13} , Fig 3.6 shows that negatives values for this constant were found in accordance with the theoretical calculations of [71], although the experimental value is positive. For C_t and B_0 (Figs. 3.7 and 3.8, respectively), the best performances are from LDA, vdw-df-c09 and vdw-df2-c09 using the experimental lattice constants and vdw-df and vdw-df2 using the theoretical lattice constants.

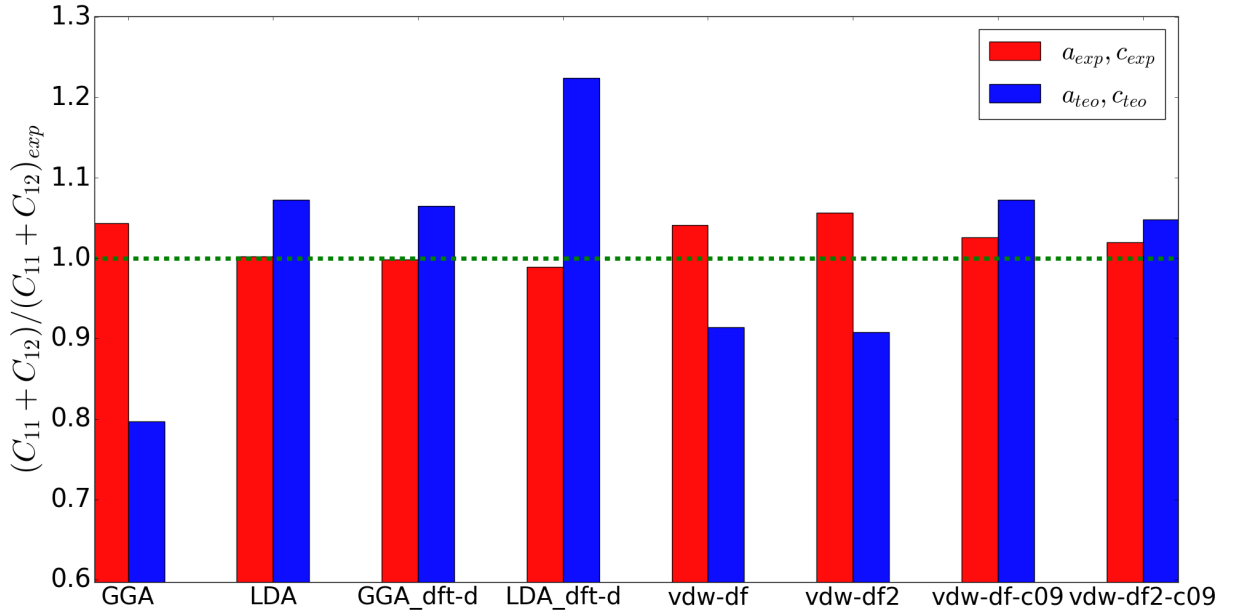


Figure 3.4: $C_{11} + C_{12}$ elastic constant divided by its experimental value (1240GPa at 300K) [71]

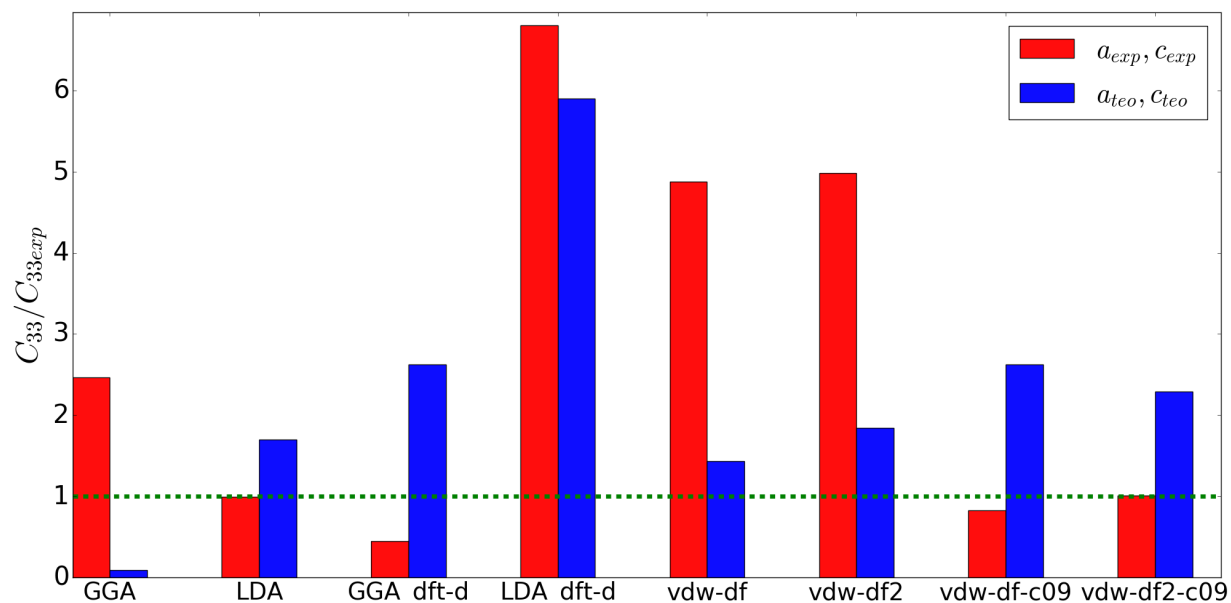


Figure 3.5: C_{33} elastic constant divided by its experimental value (36.5GPa at 300K) [71]

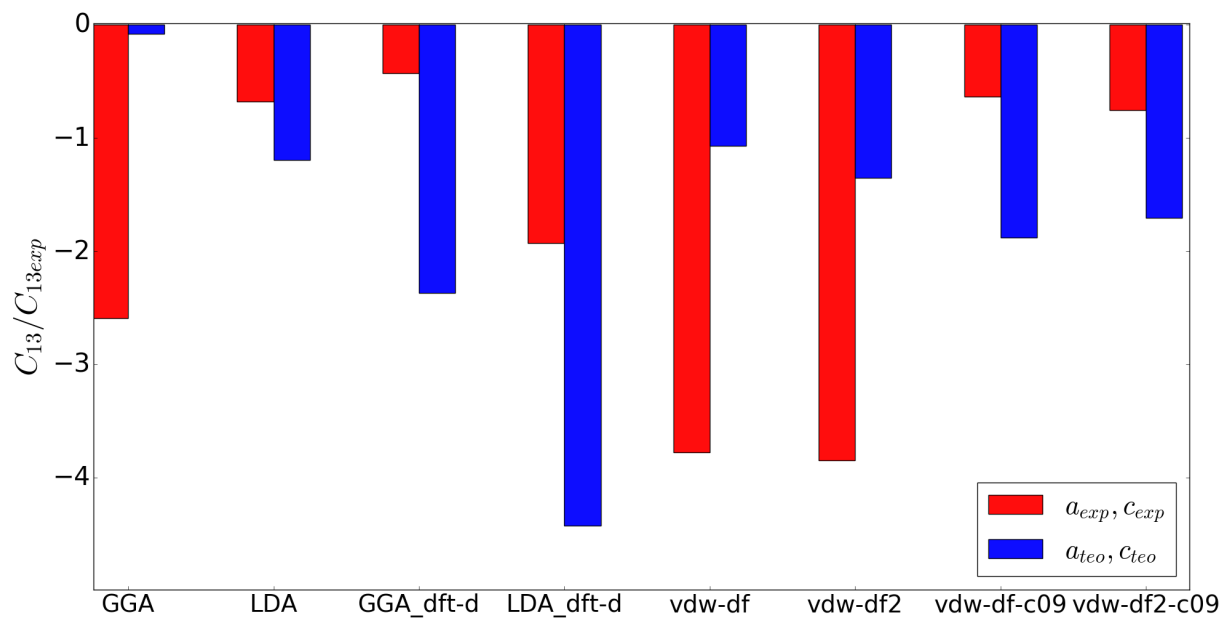


Figure 3.6: C_{13} elastic constant divided by its experimental value (15GPa at 300K) [71]

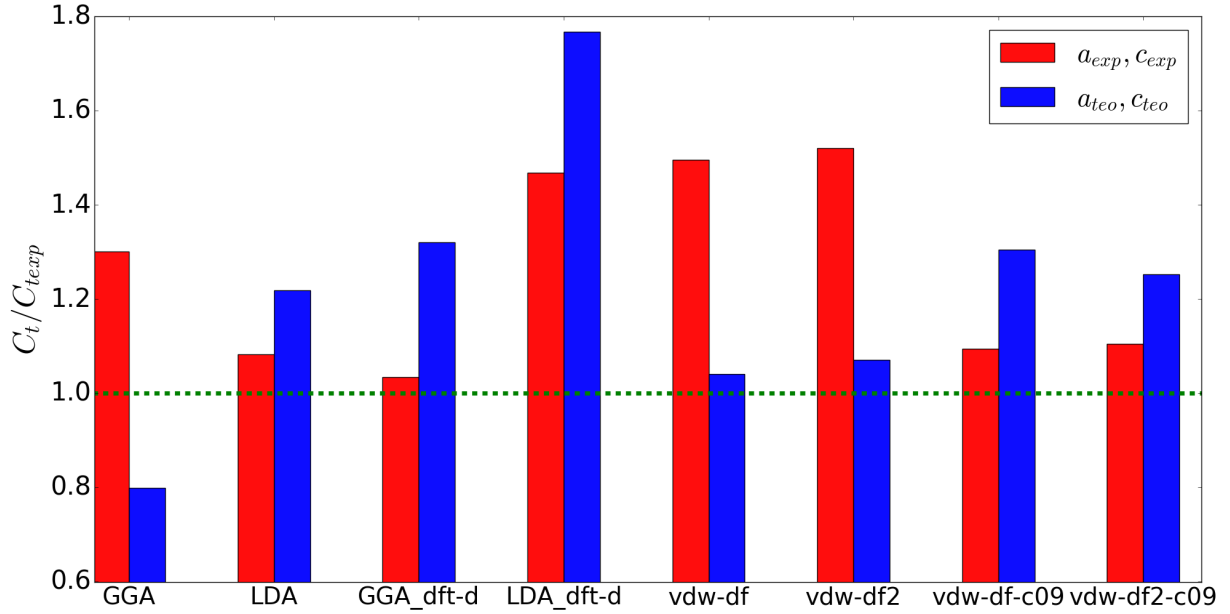


Figure 3.7: C_t elastic constant divided by its experimental value (208.8GPa at 300K) [71]

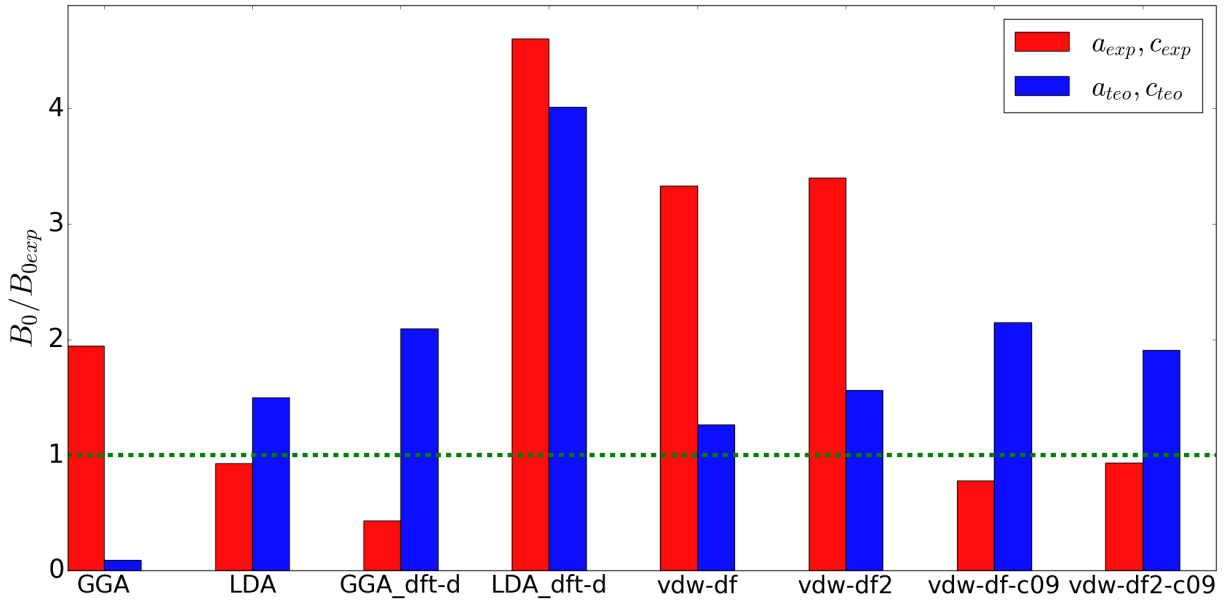


Figure 3.8: Bulk modulus divided by its experimental value (35.8GPa at 300K) [71]

Another relevant elastic constant is the Poisson ratio. To evaluate it, a rectangular supercell was created (fig. 3.9) and distortions from -2% to 2% were applied in the \hat{x} (\hat{y}) direction and, after relaxations the distortions in the \hat{y} (\hat{x}) directions were measured. As the Poisson ratio is given by

$$\nu_{ij} = -\frac{\epsilon_i}{\epsilon_j}, \quad (3.5)$$

where ϵ_i is the strain in the \hat{i} direction, we plotted ϵ_y as a function of ϵ_x and fit the curve to a linear function (fig. 3.10), from which the Poisson ratio ν_{xy} was extracted.

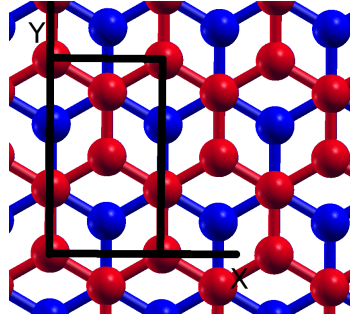


Figure 3.9: Graphite supercell used to evaluate poisson ratio, represented by the black rectangle. \hat{y} direction corresponds to armchair direction and \hat{x} to zig-zag. Figure created with xcrsden software [18, 19].

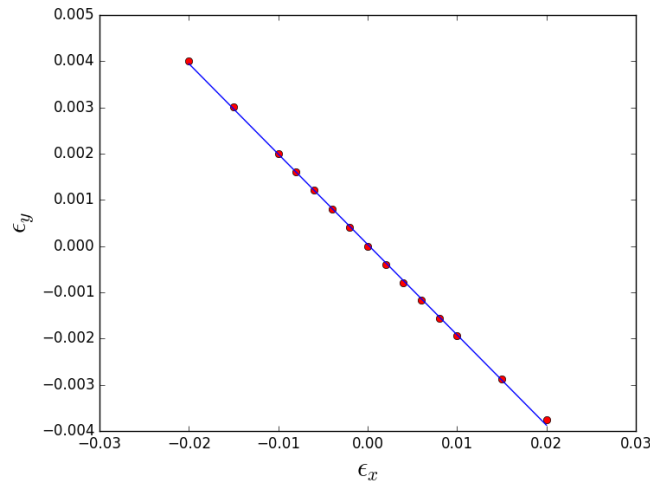


Figure 3.10: Example of poisson ratio evaluation

The in-plane Poisson ratio was evaluated by applying distortions in armchair and zig-zag directions for different functionals. The results are shown in Fig. 3.11. The values are independent of the distortion direction and the vdw-df2 has the closest agreement with the experimental value [72].

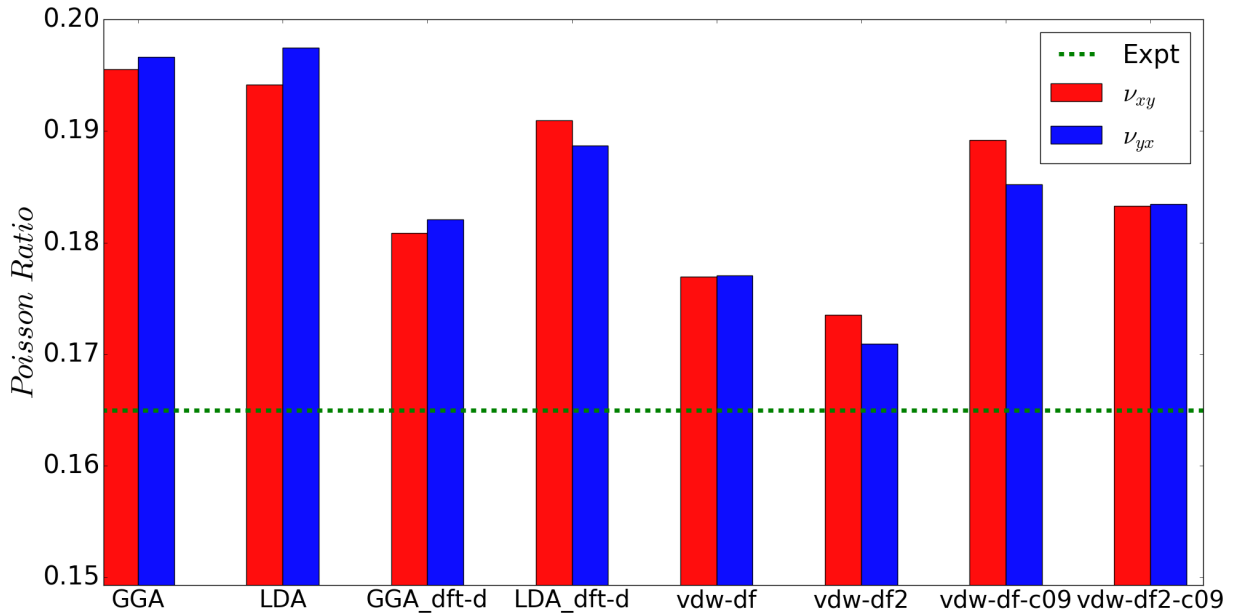


Figure 3.11: Poisson ratio evaluated by applying distortion in the armchair (zig-zag) direction and measuring distortion in the zig-zag (armchair) direction. Experimental value: $\nu_{exp} = 0.165$ [72]

The energy per atom was evaluated for several interlayer distances $c/2$ in order to calculate the exfoliation energy of graphite. The results are summarized in Fig. 3.12. The values that are closer to the reported experimental values are from the GGA with dft-d, vdw-df, vdw-df2 and vdw-df2-c09 functionals. LDA has also a good performance reproducing the exfoliation energy and GGA gives a much smaller exfoliation energy as compared to experiment data.

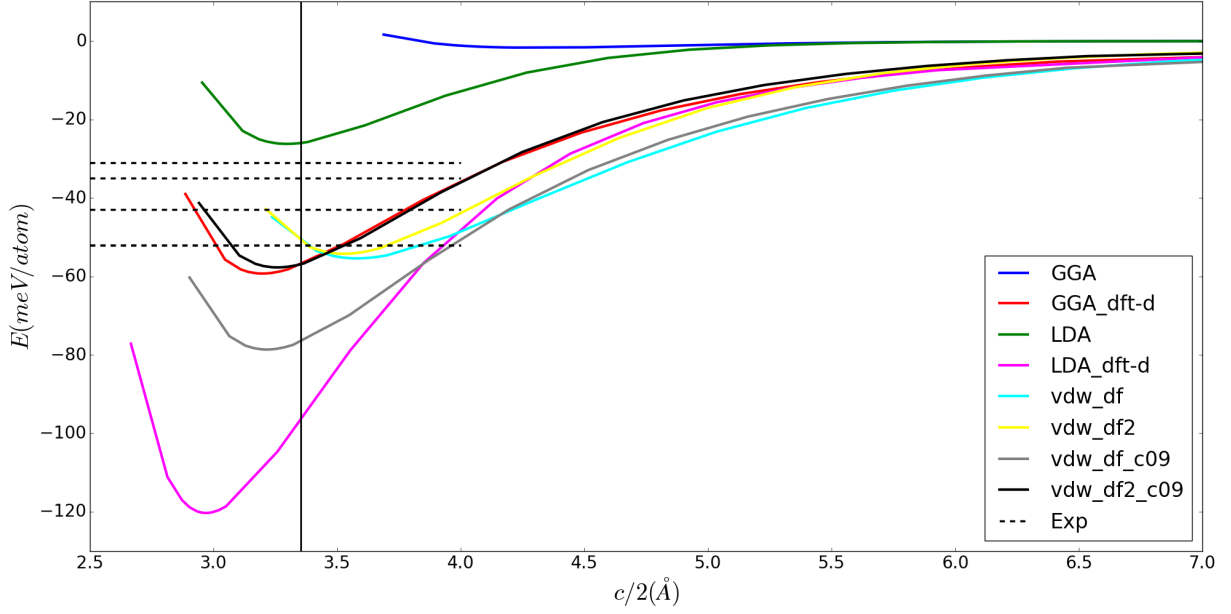


Figure 3.12: Interlayer interaction energy per atom in graphite as a function of the interlayer distance $c/2$ evaluated for several functionals. Horizontal dashed lines represent experimental values for the exfoliation energy per atom [78] and the horizontal line represents the experimental value for the interlayer distance 3.35265\AA [71]. Experimental values in meV/atom are: 42 [79], 35 [80], 52 [81], 31 [82]

3.2.3 Multilayer Graphene

Considering the exfoliation energy, stiffness coefficients and phonon frequencies (section 3.3.2) we chose as VDW functional the vdw-df2-c09. For multilayer graphene we worked with GGA and LDA without VDW corrections and vdw-df2-c09 functionals to evaluate their layer breathing and shear modes frequencies. For each functional we used as in plane lattice parameter those in fig. 3.2 assuming that the bond distance will not vary with the number of layers.

The structures were prepared in the Bernal stacking and its ionic positions relaxed in z direction. For bilayer, trilayer graphene and graphite the mean interlayer distance is the real interlayer although in 4layer and 5 layer graphene the variation in interlayer distances is about 0.02\AA . The mean interlayers distances are shown in fig. 3.13.

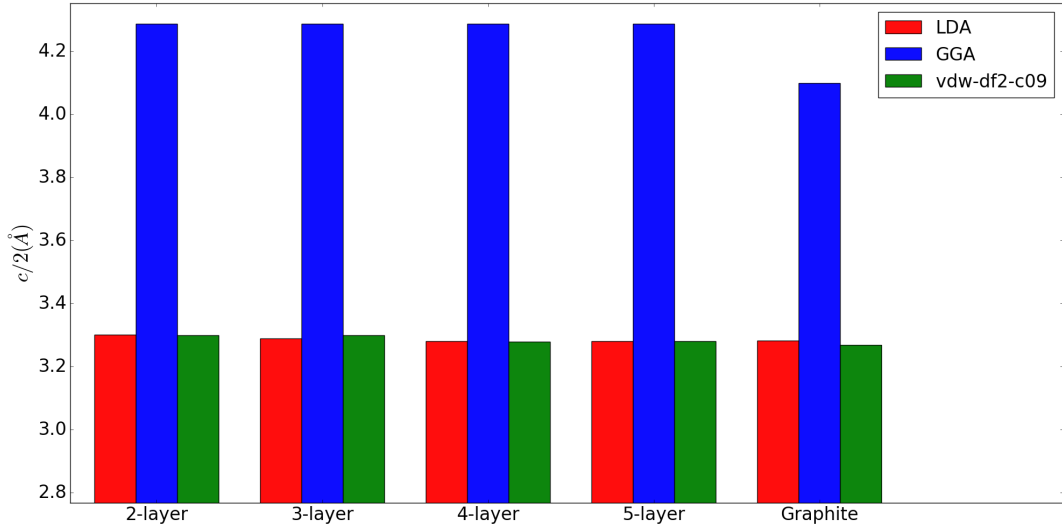


Figure 3.13: Mean interlayer distance for multilayer graphene and graphite.

3.3 Phonon Dispersion

For all DFPT calculations the acoustic sum rule is imposed, the frequencies of acoustic modes at the Γ point are zero and the Monkhorst-Pack mesh used was $8 \times 8 \times 2$. The path in the BZ for the phonon dispersion evaluation for graphene, graphite and multilayer graphene is shown in fig. 3.14.

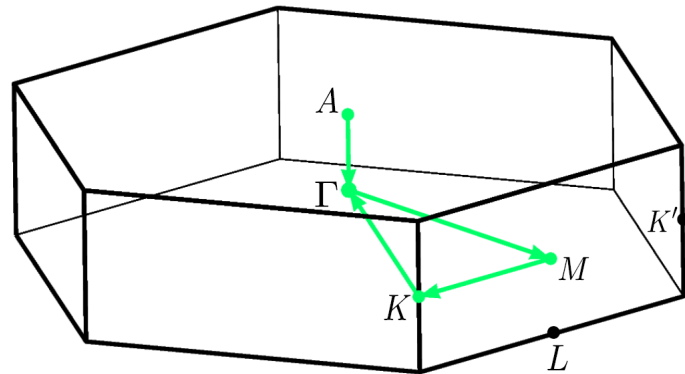


Figure 3.14: K path for evaluation of the phonon dispersion for graphite. For graphene and multilayer graphene the same path is used except the $A - \Gamma$ part

3.3.1 Graphene

DFPT

For graphene, only DFPT calculations with GGA and LDA functionals were done. The results are shown in fig. 3.15. LDA calculations give higher frequencies than GGA for optical modes.

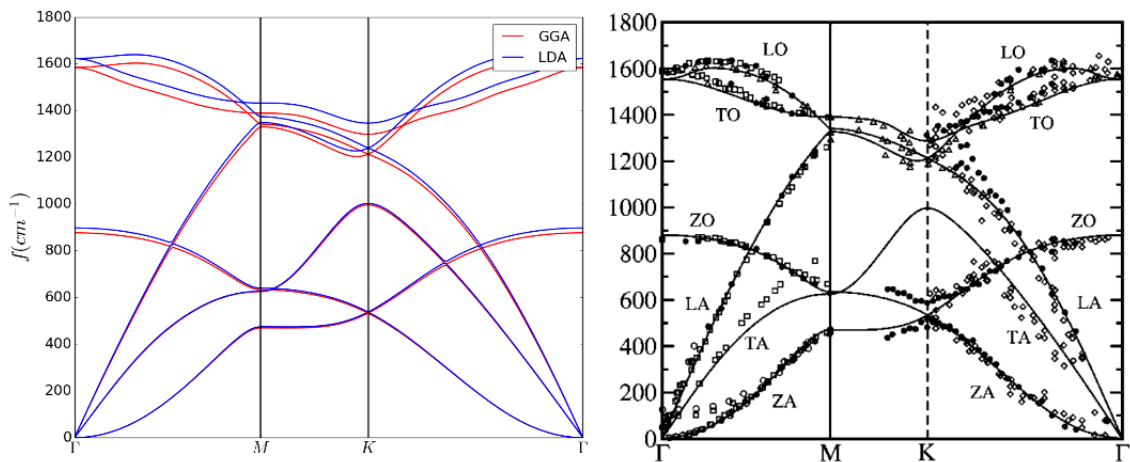


Figure 3.15: (Left) Phonon dispersion of graphene calculated in the LDA and GGA approximations. (Right) Solid line: GGA calculation [71] on graphene and experimental data of graphite. The experimental data are EELS (electron energy loss spectroscopy) from [87–89] (respectively squares, diamonds, and filled circles), neutron scattering from [90] (open circles), and x-ray scattering from [86] (triangles). Figure reproduced from [71]

3.3.2 Graphite

DFPT

For graphite, DFPT calculations with LDA and GGA functionals using the theoretical and experimental lattice constants (figs. 3.2 and 3.3) were done and the results are summarized in fig. 3.16. Presently, DFPT calculations with VDW functionals are not yet implemented in the Quantum Espresso [68], although there are works in progress in this direction [92].

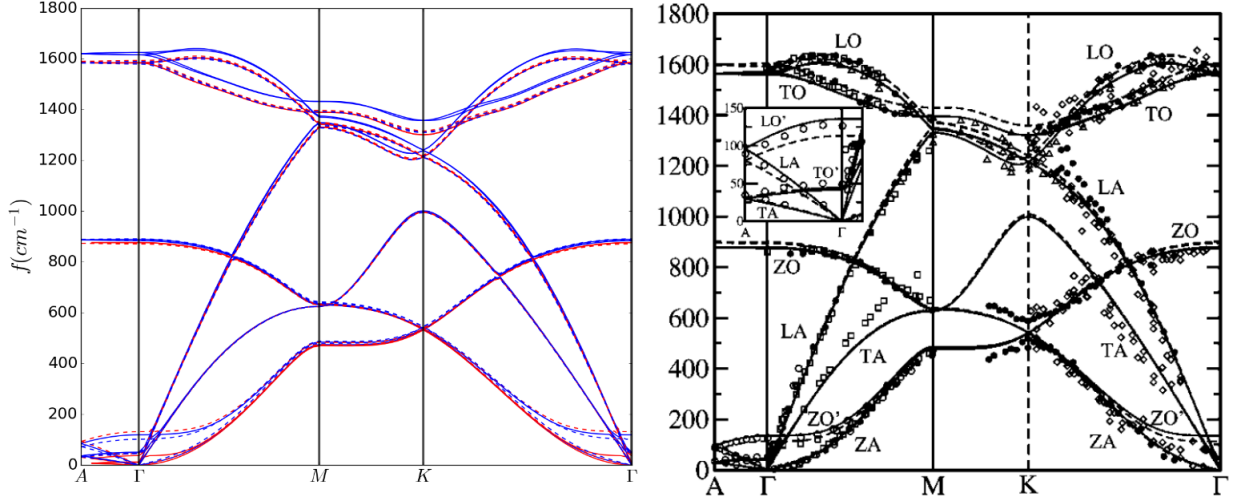


Figure 3.16: (Left) Phonon dispersion for graphite using GGA (red) and LDA (blue) with the theoretical lattice parameters (solid lines) or experimental (dashed lines). (Right) GGA (solid lines) and LDA (dashed lines) from [71]. The experimental data are EELS (electron energy loss spectroscopy) from [87–89] (respectively squares, diamonds, and filled circles), neutron scattering from [90] (open circles), and x-ray scattering from [86] (triangles). Figure reproduced from [71]

Frozen Phonon

Following the procedure explained in section 2.6.2, we performed frozen-phonon calculations for a couple phonon-modes. We focus on in-plane (shear) and out-of-plane modes at Γ in which the graphite planes move rigidly with respect to each other according to the eigenvectors shown in appendix A. For each displacement along these modes a SCF calculation was done and the corresponding frequencies were obtained from the harmonic approximation (Appendix B). Examples of how the procedure works are shown in fig. 3.17

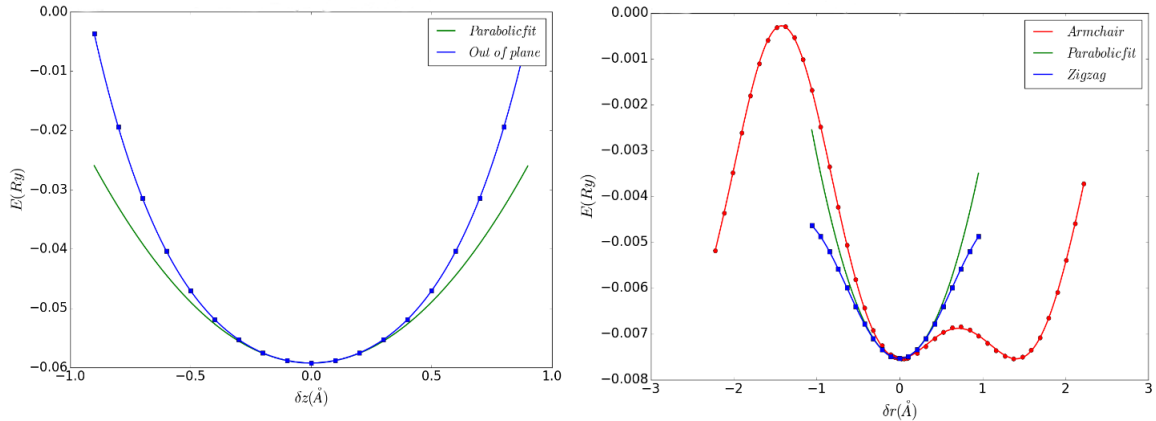


Figure 3.17: Example of frozen phonon calculations for out-of-plane (left) and in-plane (right) modes. The two in plane modes (displacements in the armchair and zigzag directions) are degenerate. Harmonic fits (green curves) are presented for comparison.

One can see in the above graphs that anharmonic effects may be important for a proper description of these vibrational modes. We also included anharmonic effects by first order perturbation theory as explained in Appendix B for the out-of-plane modes. In plane modes would require degenerate perturbation theory and we leave this subject for future work. Results comparing the inclusion of anharmonic effects are summarized in fig. 3.23

Data Analysis

The results of DFPT and frozen phonon calculations for the in-plane and out-of-plane modes are shown in figs. 3.18 and 3.19 respectively. Theoretical and experimental lattice parameters were used.

For the in plane mode, in general, the use of experimental lattice parameters improves the performance of the calculations. For the theoretical parameters, LDA and vdw-df2-c09 have the best performances in reproducing the experimental value of the frequency.

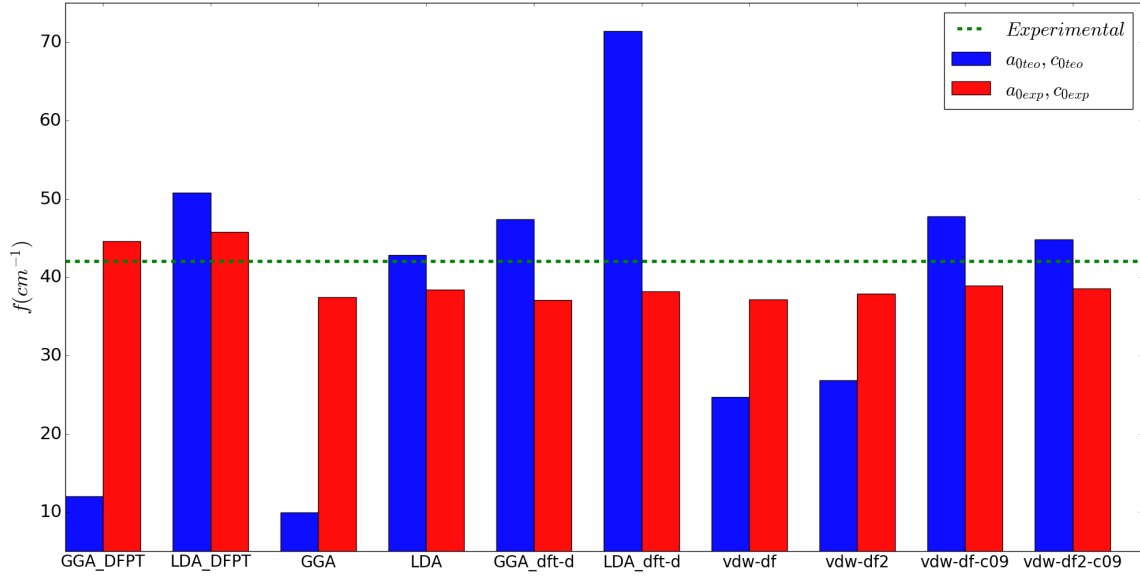


Figure 3.18: Comparison of DFPT method and frozen-phonon for several functionals for the in plane mode frequency at the Γ point. Experimental value is 42 cm^{-1} [91]. Bars without label DFPT refer to frozen phonon calculations.

For the out of plane mode, the use of GGA with experimental lattice parameters and LDA, GGA with dft-d, vdw-df-c09 and vdw-df2-c09 with theoretical parameters have the best performances.

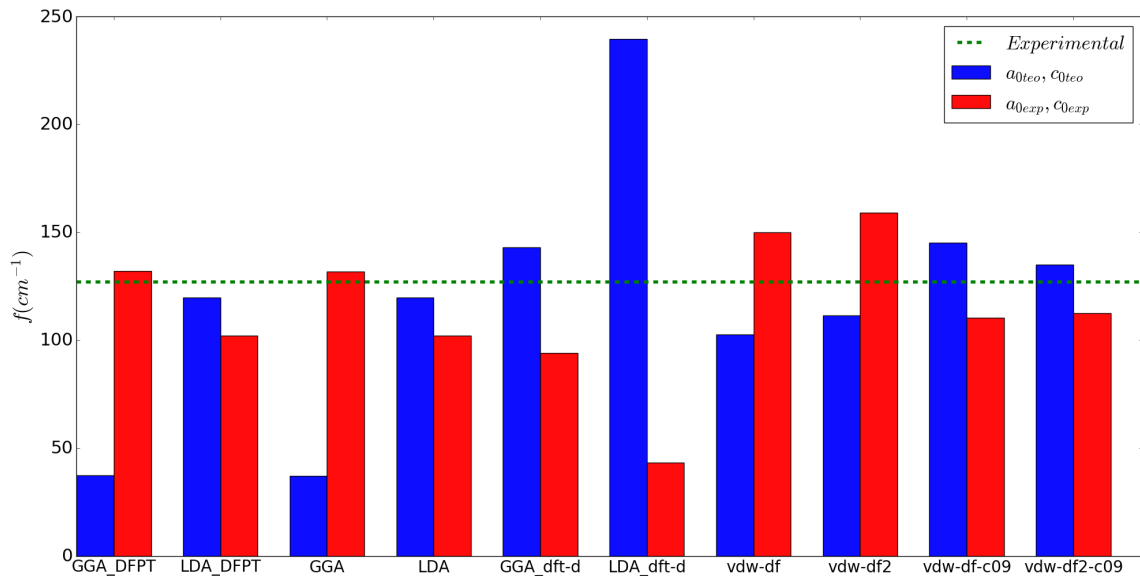


Figure 3.19: Comparison of DFPT method and frozen-phonon for several functionals for the out of plane mode. Experimental value is 127 cm^{-1} [91]. Bars without label DFPT refer to frozen phonon calculations.

The LDA with dft-d using theoretical lattice parameters overestimates the frequencies of the in plane and out of plane modes. This can be associated to the overestimation of the binding energy of graphene using this functional (see fig. 3.12). One can also notice that there is a good agreement between DFPT and frozen phonon calculations for the LDA and GGA functionals, thus showing that the eigenvectors for graphite in appendix A are exact.

3.3.3 Multilayer Graphene

As there is no experimental values for the interlayer distance for multilayer graphene, we use theoretical values obtained from relaxation. The in plane parameter used for all cases was the theoretical value for graphite for each functional, as shown in fig. 3.2.

For multilayer graphene, we use only the vdw-df2-c09 as functional that includes VDW interactions, as it has the best performance in reproducing the experimental frequencies and exfoliation energies for graphite, according to our discussion in the previous section.

DFPT

DFPT calculations for multilayer graphene (from 2 to 5 layers) were done for GGA and LDA functionals and phonon dispersions are shown in fig. 3.20.

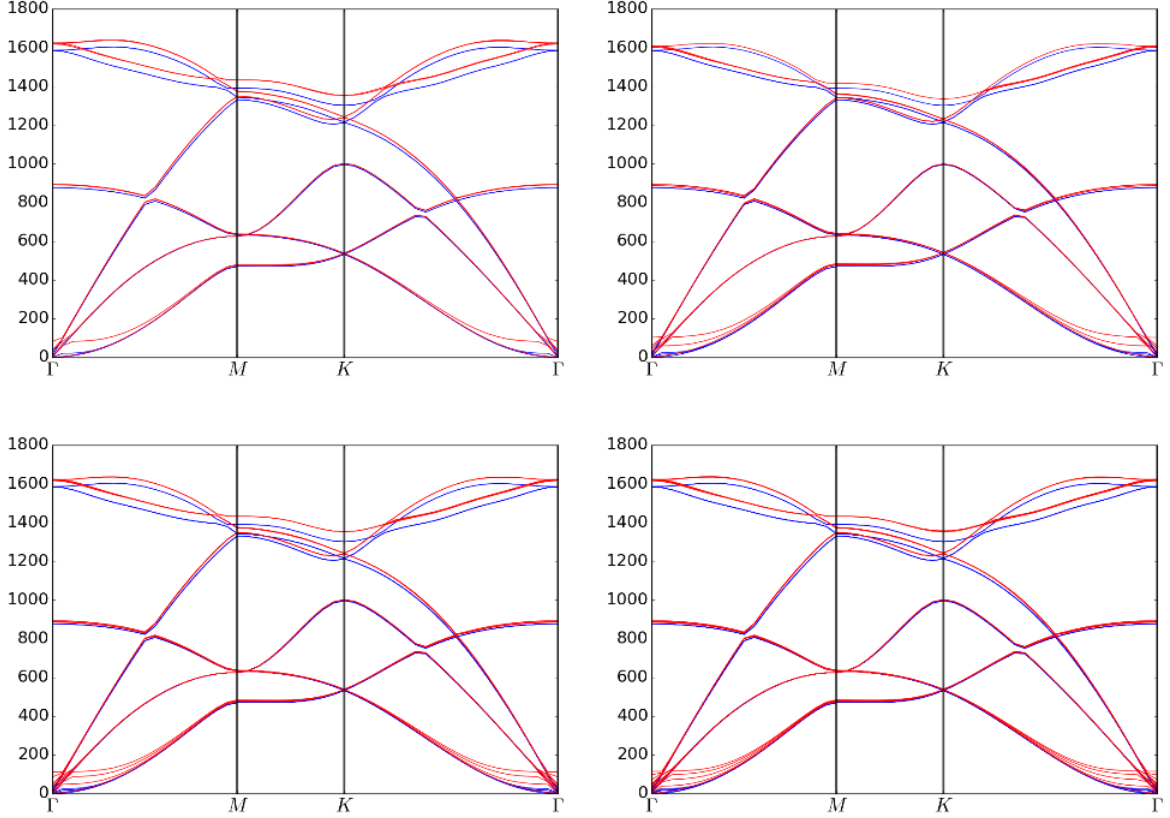


Figure 3.20: Phonon dispersion of bilayer graphene (top left), trilayer graphene (top right), 4layer graphene (down left) and 5layer graphene (down right) using LDA (red lines) and GGA (blue lines) functionals. Units in cm^{-1}

At the Γ point, there are $N - 1$ out-of-plane non-zero frequency modes and $2(N - 1)$ in-plane non-zero frequency modes degenerated two by two.

Frozen Phonon

For multilayer graphene we follow a procedure similar to that of graphite, as described in section 3.3.2. However, for multilayer graphene, we use an approximation of nearest-neighbor interactions only between graphene sheets and the assumption that force constants between neighboring sheets are the same for all pairs. The accuracy of these approximations assumptions will be tested against the finite difference approach, to be described below. The corresponding eigenvectors can be found in appendix A.

We included anharmonic effects by first order perturbation theory as explained in

Appendix B. Results comparing the inclusion of anharmonic effects are summarized in fig. 3.23.

Finite Difference Method

As explained in section 2.6.2, we construct the FCM by applying displacements in specific directions and measuring the forces over graphene layers. For each layer, displacements from -0.6 bohr to 0.6 bohr were applied and curves of force vs distance were fitted by a fifth order polynomial as in fig. 3.21. The force constant is given by the first derivative of the fitted curve. Once the FCM is obtained the acoustic sum rule is imposed.

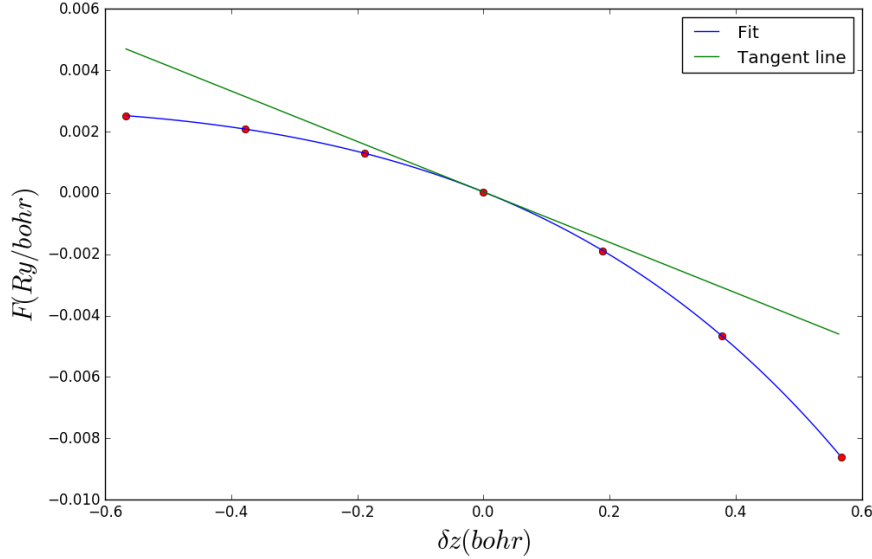


Figure 3.21: Force in the out-of-plane direction on the edge layer of 4-layer graphene as a function of the displacement in the out-of-plane direction of the same layer as an example of evaluation of a matrix element of the FCM. This example corresponds to $\mu = 1$ and $\nu = 1$ in eq. 2.104

Data Analysis

Out of plane frequencies obtained from DFPT, frozen-phonon (FP) and finite difference (FD) at the Γ point method are shown in fig. 3.22. All three methods used for LDA and GGA agree with each other satisfactorily, indicating that the eigenvectors, obtained from first neighbors approximation, in appendix A are good approximations. Vdw-df2-

c09 gives higher frequencies than LDA by about $5 - 10 \text{ cm}^{-1}$ and reproduces better the experimental values from [94] for the higher frequencies for each N-layer. GGA gives frequencies that are clearly too low with respect to experiment.

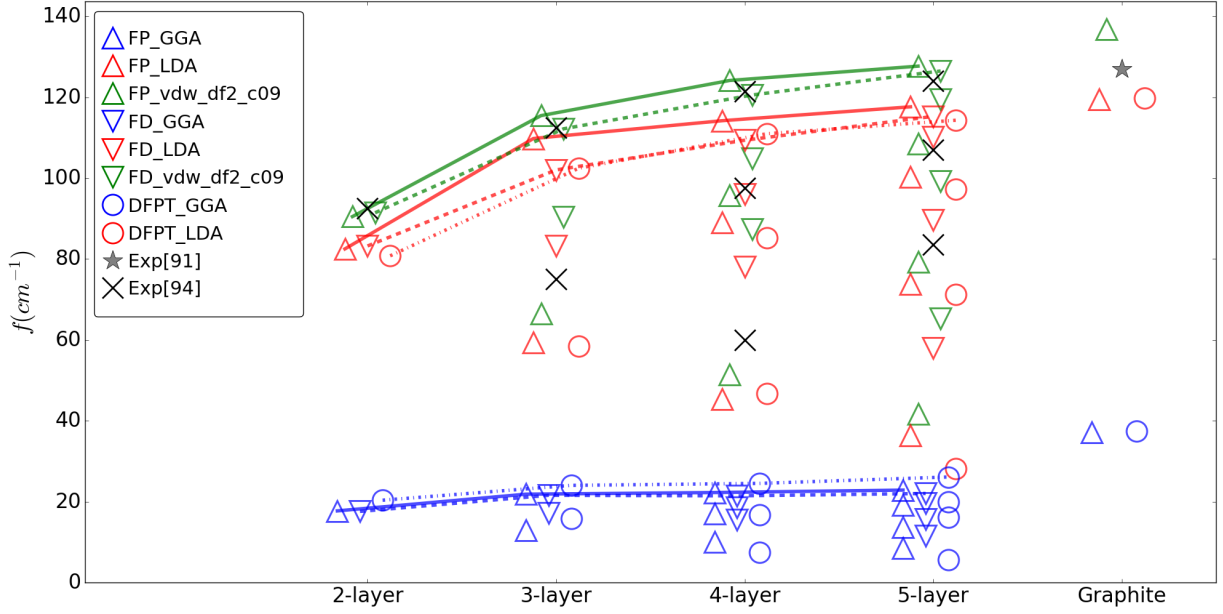


Figure 3.22: Out of plane frozen phonon (FP), finite difference (FD) and DFPT calculations (triangles, reverse triangles and circles respectively) using GGA (blue), LDA (red) and vdW-df2-c09 (green) functionals. Experimental value for the layer breathing mode of graphite is from [91] and black crosses are experimental values from two-phonon overtone spectra observed in doubly resonant Raman spectroscopy in [94]. Lines are connecting the higher frequencies for each N-layer to show the convergence of those values with the number of layers until they reach the graphite frequency. Theoretical calculations of graphite presented here were done with the theoretical lattice parameters (figs. 3.19).

We also included anharmonic effects in the frozen phonon calculations by first order perturbation theory (see appendix B). In general, its inclusion improves the frequencies of low out-of-plane optical modes.

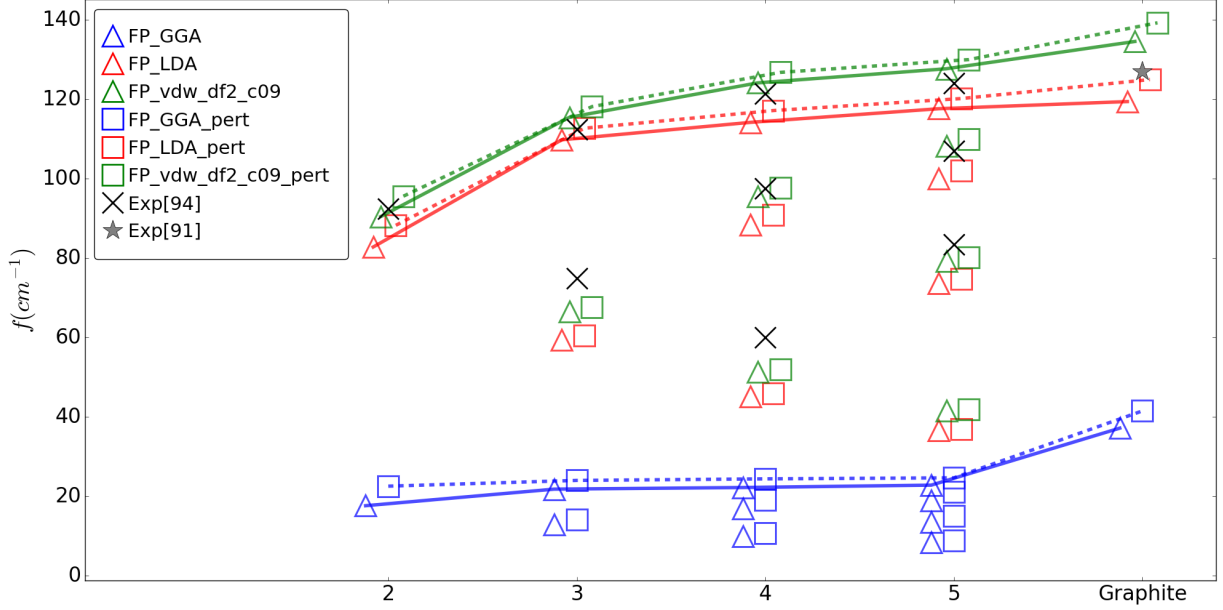


Figure 3.23: Effect of including anharmonic effects in the out-of-plane modes in frozen phonon calculations. Squares include anharmonic effects and triangles do not using GGA (blue), LDA (red) and vdw-df2-c09 (green) functionals. Experimental value for the layer breathing mode of graphite is from [91] and black crosses are experimental values from two-phonon overtone spectra observed in doubly resonant Raman spectroscopy in [94]. Lines are connecting the higher frequencies for each N-layer to show the convergence of those values until graphite frequency. Theoretical calculations of graphite presented here were done with the theoretical lattice parameters (figs. 3.18).

In plane frequencies obtained from DFPT, FP and FD at the Γ point method are shown in fig. 3.24. Once again, all calculations with GGA have very small frequencies due to the weak interaction between layers (fig. 3.12). We notice several potential problems in the calculations: (1) Contrary to the out-of-plane case, DFPT for LDA does not agree very well with FP for LDA. (2) FP and FD method for LDA and vdw-df2-c09 cases work well for bilayer graphene, although for the other multilayer structures they underestimate the experimental frequency and have smaller frequency than the DFPT for LDA. (3) FP calculations seem not to follow the trend that the highest frequency should increase with the number of layers, gradually approaching the value for graphite.

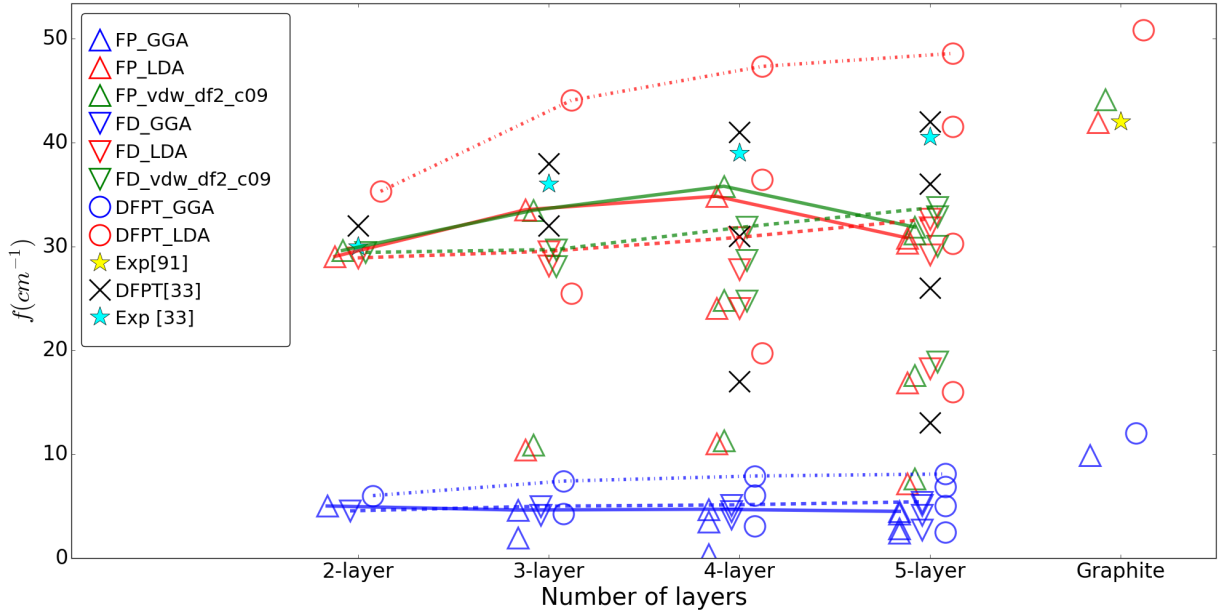


Figure 3.24: In plane frozen phonon (FP), finite difference (FD) and DFPT calculations (triangles, reverse triangles and circles respectively) using GGA (blue), LDA (red) and vdw-df2-c09 (green) functionals. Experimental value for the shear mode of graphite is from [91], black crosses are ab initio calculations from [33] and cyan stars are experimental Raman measures of C peak position from [33]. Lines are connecting the higher frequencies for each N-layer to show the convergence of those values until graphite frequency. Theoretical calculations of graphite presented here were done with the theoretical lattice parameters (figs. 3.18).

Trying to correct the results, a convergence study of the frequencies of in-plane modes was done in relation to the K points sampling and an example of analysis is shown in fig. 3.25. Some frequencies change about 5cm^{-1} . We believe that this happens because of the symmetry break due to in-plane displacements that opens an electronic gap in multilayer graphene requiring a higher K points sampling.

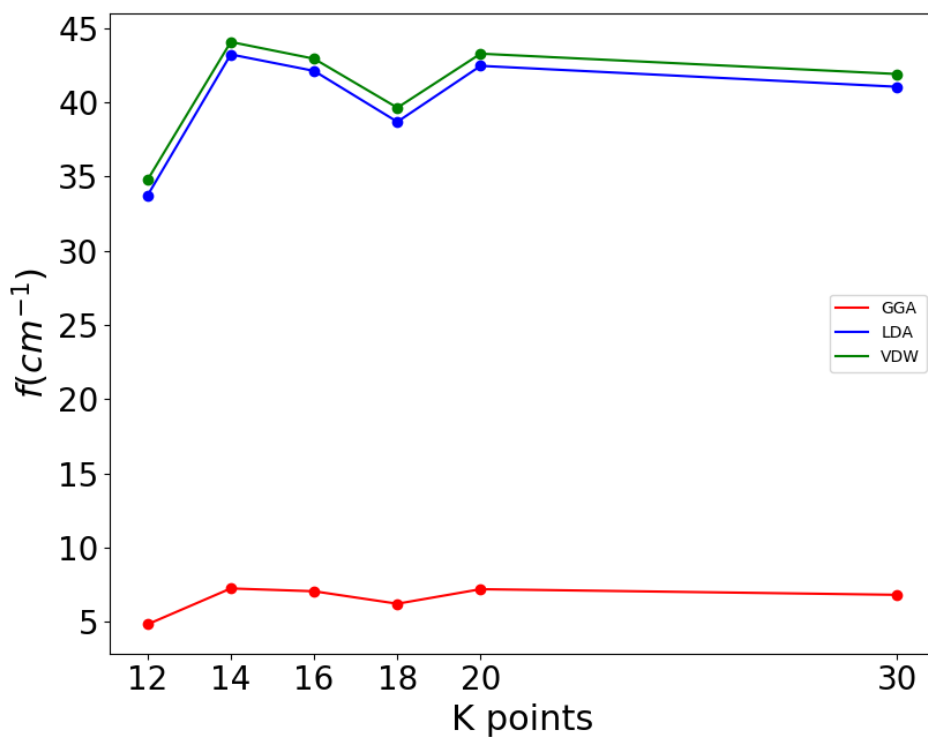


Figure 3.25: Convergence of the frequency of the highest mode of 5-layer graphene in relation to the number of K points sampling

We considered a grid $30 \times 30 \times 1$ satisfactory and frozen phonon frequencies with this grid are shown in fig. 3.26. The higher frequencies of in plane modes are closer to the experimental values and show the convergence behavior in relation to the number of layers.

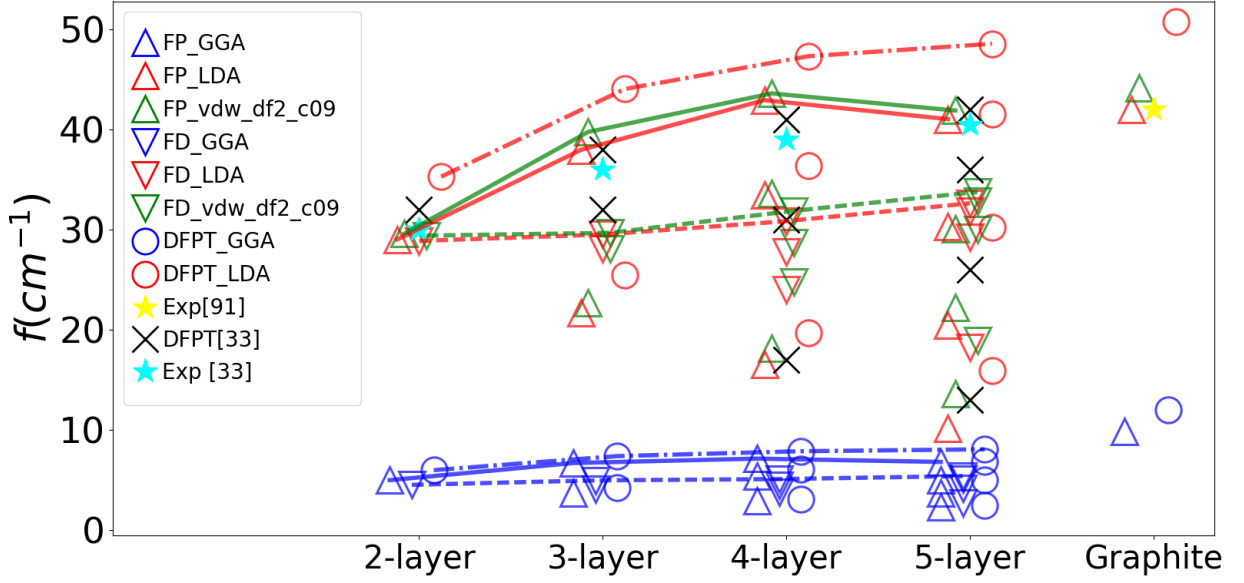


Figure 3.26: In plane frozen phonon (FP) using higher K points sampling than in fig. 3.24, finite difference (FD) and DFPT calculations (triangles, reverse triangles and circles respectively) using GGA (blue), LDA (red) and vdw-df2-c09 (green) functionals. Experimental value for the shear mode of graphite is from [91], black crosses are ab initio calculations from [33] and cyan stars are experimental Raman measures of C peak position from [33]. Lines are connecting the higher frequencies for each N -layer to show the convergence of those values until graphite frequency. Theoretical calculations of graphite presented here were done with the theoretical lattice parameters (figs. 3.18).

To evaluate the consistency of our calculations, we can evaluate the ratio $(\omega_{\text{graphite}}/\omega_{\text{bilayer}})^2$. By analyzing the eigenvalues in appendix A, this ratio is expected to near 2, if one considers a simple mass-spring model in which, within the first neighbor approximation, one graphene sheet in graphite interacts with other two adjacent layers, while in bilayer graphene one graphene layer just interacts with another, making the effective spring constant over one layer in graphite twice that of one layer in bilayer graphene (of course, assuming the the force constants do not change their value with the number of layers).

Table 3.2: $(\omega_{graphite}/\omega_{bilayer})^2$

	LDA	GGA	vdw-df2-c09
In plane			
DFPT	2.07	4.0	-
Frozen phonon	2.17	3.95	2.29
Out of plane			
DFPT	2.20	3.38	-
Frozen phonon	2.11	4.45	2.23
Frozen phonon with perturbation	2.00	3.38	2.13

Table 3.2 shows that the ratio $(\omega_{graphite}/\omega_{bilayer})^2$ is close to 2 for by LDA and vdw-df2-c09 in both DFPT and frozen phonon techniques, but much higher for GGA calculations.

Chapter 4

Conclusions

In summary, we have analyzed the accuracy of different vdW functionals in describing different properties of graphene and graphite. For graphene most physical parameters obtained with GGA and LDA functionals are in good agreement with experimental and other reported theoretical values. The phonon dispersion is also satisfactory except at the K point, where the Born-Oppenheimer approximation fails [96].

For graphite, we have analyzed the stiffness coefficients, exfoliation energy and the frequencies of the breathing layer and shear modes obtained from DFPT and frozen phonon calculations. Based on our results, we chose the vdw-df2-c09 as the best functional for calculations in multilayer graphene, even though LDA with no VDW corrections also has a good performance. For properties that depend on a good description of the interlayer interaction, GGA with no VDW corrections gives the worst results.

For calculations on multilayer graphene, DFPT, frozen phonon (FP) and finite difference methods (FD) were used. The out-of-plane mode is better reproduced by FP and FD with the vdw-df2-c09 functional. It is possible to see that the higher frequencies of N -layer graphene converges to graphite frequency with respect to the number of layers. The in-plane modes are not well reproduced by FP and FD. DFPT with LDA gives the correct behavior, but it overestimates the experimental values. The use of a higher K points sampling for frozen phonon correct those frequencies reproducing better the ex-

perimental results. The use of first order perturbation theory in the out of plane modes gives small corrections to calculated frequencies and brings them closer to experimental values.

In summary, we see that the use of vdw-df2-c09 improves substantially the properties that depend on the interlayer interactions, although LDA with no VDW corrections gives satisfactory results. Frozen phonon calculations including only nearest layer interactions have a good performance in comparison to other methods.

Bibliography

- [1] Geim, A. K., Novoselov, K. S. *The rise of graphene*, Nat Mater, **6**, (2007) 183-191
xiii, 1, 2
- [2] Novoselov, K. S. *Nobel Lecture: Graphene: Materials in the Flatland*, Rev. Mod. Physics, vol 83, No. 3 (2011), 837-849 1, 2
- [3] K. S. Novoselov, A. K. Geim, S. V. Morozov, D. Jiang, Y. Zhang, S. V. Dubonos, I. V. Grigorieva, A. A. Firsov *Electric Field Effect in Atomically Thin Carbon Films*, Science, vol. 306, (2004), 666-669 1
- [4] H. W. Kroto, J. R. Heath, S. C. O'Brien, R. F. Curl, R. E. Smalley, *C60: Buckminsterfullerene* Nature. 318 (6042): 162-163. (1985) 1
- [5] R. E. Smalley, *Discovering the fullerenes* Rev. Mod. Physics, Vol. 69, No. 3, 723-730 (1997) 1
- [6] S. Iijima, *Helical microtubules of graphitic carbon*, Nature, **354**, 56-58 (1991) 1
- [7] A. H. Castro Neto, F. Guinea, N. M. R. Peres, K. S. Novoselov, A. K. Geim *The electronic properties of graphene*, Rev. Mod. Physics, vol 81, No. 1 (2009), 109-162
xiii, xiv, 3, 8
- [8] Daniel R. Cooper, Benjamin D'Anjou, Nageswara Ghattamaneni, Benjamin Harack, Michael Hilke, Alexandre Horth, Norberto Majlis, Mathieu Massicotte, Leron Vands-

- burger, Eric Whiteway, Victor Yu, *Experimental Review of Graphene*, ISRN Condensed Matter Physics, vol 2012, doi:10.5402/2012/501686 3
- [9] Jiang-Bin Wu, Xin Zhang, Mari Ijäs, Wen-Peng Han, Xiao-Fen Qiao, Xiao-Li Li, De-Sheng Jiang, Andrea C. Ferrari, Ping-Heng Tan *Resonant Raman spectroscopy of twisted multilayer graphene*, (2014), Nature communications, Doi: 10.1038/ncomms6309 xiii, 3, 4
- [10] V. Meunier, A. G. Souza Filho, E. B. Barros, M. S. Dresselhaus, *Physical properties of low-dimensional sp²-based carbon nanostructures*, Rev. Mod. Physics, vol. 88, No. 2 (2016), Doi: 10.1103/RevModPhys.88.025005 7
- [11] R. Saito, G. Dresselhaus, M. S. Dresselhaus, *Physical Properties of Carbon Nanotubes*, Imperial College Press (1998) 7
- [12] N. W. Ashcroft and N. D. Mermin, *Solid State Physics* (1976) 8, 24, 26, 36, 40, 89
- [13] C. Kittel, *Introduction to Solid State Physics - 7th ed.* (1996) 26
- [14] O. Madelung *Introduction to solid state theory*, Springer (1978) 11, 26
- [15] J. D. M. Vianna, A. Fazzio, S. Canuto *Teoria Quântica de Moléculas e Sólidos - simulação computacional*, Livraria da Física (2004) 13, 16, 24, 26, 35, 41, 42
- [16] R. M. Martin *Electronic Structure - Basic Theory and Practical Methods*, Cambridge University Press (2004) xiv, 11, 13, 16, 23, 25, 26, 28, 30, 31, 41, 42
- [17] E. Kaxiras *Atomic and Electronic Structure of Solids*, Cambridge University Press (2003) xiv, 28, 30, 36
- [18] A. Kokalj, *Computer graphics and graphical user interfaces as tools in simulations of matter at the atomic scale*, Comp. Mater. Sci., (2003), 28, 155–168. Code available from <http://www.xcrysden.org/>. xiv, xv, 9, 56

- [19] A. Kokalj, *XCrySDen—a new program for displaying crystalline structures and electron densities*, J. Mol. Graphics Modelling, (1999), 17, 176–179. xiv, xv, 9, 56
- [20] Chun Hung Lui, Zhiqiang Li, Kin Fai Mak, Emmanuele Cappelluti, Tony F. Heinz, *Observation of an electrically tunable band gap in trilayer graphene*, Nature Physics, vol.7 (2011) xiv, 9, 10
- [21] Toshiaki Enoki, Tsuneya Ando *Physics and Chemistry of Graphene - Graphene to Nanographene*, CRC Press (2014) xiv, 10
- [22] W. Kohn *Nobel Lecture: Electronic structure of matter - wave functions and density functionals*, Rev. Mod. Physics, Vol. 71, No. 5, (1999) 15
- [23] L. Thomas *The calculation of atomic fields*, Mathematical Proceedings of the Cambridge Philosophical Society, Vol. 23, Issue 5, 542-548 (1927) 16
- [24] E. Fermi *Un Metodo Statistico per la Determinazione di alcune Proprietà dell'Atomo*, Rend. Accad. Naz. Lincei., **6**, 602-607 (1927) 16
- [25] P. Hohenberg, W. Kohn *Inhomogeneous electron gas*, Phys. Rev. B, Vol. 136, N. 3B, B864-871 (1964) 17
- [26] W. Kohn, L. J. Sham *Self-Consistent Equations Including Exchange and Correlation Effects* Phys. Rev. **140**, A1133-A1138 (1965) 20
- [27] A. E. Mattsson *In Pursuit of the "Divine" Functional*, Science, Vol. 298 759-760 (2002) 24
- [28] J. P. Perdew, K. Schmidt *Jacob's Ladder of Density Functional Approximations for the Exchange-Correlation Energy*, AIP Conference Proceedings, (2001) 24

- [29] *Molecular and Solid-State Tests of Density Functional Approximations: LSD, GGAs, and Meta-GGAs*, S. Kurth, J. P. Perdew, P. Blaha, Int. J. of Quantum Chemistry, Vol. 75, 889-909 (1999) 24
- [30] V. N. Staroverov, G. E. Scuseria, *Tests of a ladder of density functionals for bulk solids and surfaces*, Phys. Rev. B **69**, 075102 (2004) 24
- [31] J. P. Perdew, A. Zunger *Self-interaction correction to density-functional approximations for many-electrons systems*, Phys. Rev. B **23**, (1981) 25, 48
- [32] J. P. Perdew, K. Burke, M. Ernzerhof *Generalized Gradient Approximation Made Simple*, Phys. Rev. Letters, Vol. 77, N. 18, 3865-3868 (1996) 25, 26, 48
- [33] P. H. Tan, W. P. Han, W. J. Zhao, Z. H. Wu, K. Chang, H. Wang, Y. F. Wang, N. Bonini, N. Marzari, N. Pugno, G. Savini, A. Lombardo, A. C. Ferrari, *The shear mode of multilayer graphene*, Nature Materials, Vol. 11, 294-300 (2012) xiii, xviii, xix, 4, 5, 69, 71
- [34] S. K. Saha, U. V. Waghmare, H. R. Krishnamurthy, A. K. Sood, *Phonons in few-layer graphene and interplanar interaction: A first-principles study*, Phys. Rev. B **78**, 165421 (2008) xiv, 4, 6
- [35] C. H. Lui, L. M. Malard, S. Kim, G. Lantz, F. E. Laverge, R. Saito, T. F. Heinz *Observation of Layer-Breathing Mode Vibrations in Few-Layer Graphene through Combination Raman Scattering*, Nano Letters, 12 (11), pp 5539-5544 (2012) xiii, 4, 5
- [36] A. E. Nel, L. Mädler, D. Velegol, T. Xia, E. M. V. Hoek, P. Somasundaran, F. Klaessig, V. Castranova, M. Thompson, *Understanding biophysicochemical interactions at the nano-bio interface*, Nature Materials, vol. 8 (2009) 32
- [37] A. K. Geim, I. V. Grigorieva, *Van der Waals heterostructures*, Nature, vol. 499 (2013)

- [38] K.S. Vasu, E. Prestat, J. Abraham, J. Dix, R. J. Kashtiban, J. Beheshtian, J. Sloan, P. Carbone, M. Neek-Amal, S. J. Haigh, A. K. Geim, R. R. Nair *Van der Waals pressure and its effect on trapped interlayer molecules*, Nature Communications (2016) 32
- [39] R. H. French, V. A. Parsegian, R. Podgornik, R. F. Rajte, A. Jagota, J. Luo, D. Asthagiri, M. K. Chaudhury, Y. Chiang, S. Granick, S. Kalinin, M. Kardar, R. Kjellander, D. C. Langreth, J. Lewis, S. Lustig, D. Wesolowski, J. S. Wettlaufer, W. Ching, M. Finnis, F. Houlihan, O. A. von Lilienfeld, C. J. van Oss, T. Zemb, *Long range interactions in nanoscale science*, Rev. Mod. Physics, Vol. 82 (2010) 32
- [40] D. Jariwala , T. J. Marks, M. C. Hersam, *Mixed-dimensional van der Waals heterostructures*, Nature Materials, (2016) Doi: 10.1038/NMAT4703 6, 32
- [41] L. M. Woods, D. A. R. Dalvit, A. Tkatchenko, P. Rodriguez-Lopez, A. W. Rodriguez, R. Podgornik, *Materials perspective on Casimir and van der Waals interactions*, Rev. Mod. Physics, vol. 88 (2016) 6, 32, 35
- [42] F. L. Leite, C. C. Bueno, A. L. Da Róz, E. C. Ziemath, O. N. Oliveira Jr. *Theoretical Models for Surface Forces and Adhesion and Their Measurement Using Atomic Force Microscopy* Int. J. Mol. Sci. (2012), 13, 12773-12856 32
- [43] W. H. Keesom *The second virial coefficient for rigid spherical molecules whose mutual attraction is equivalent to that of a quadruplet placed at its center* Proc. R. Acad. Sci. (1915), 18, 636-646. 32
- [44] J. N. Israelachvili *Intermolecular and Surface Forces - Third Edition*, Elsevier (2011) 33
- [45] V. A. Parsegian *Van der Waals Forces - A handbook for biologists, chemists, engineers and physicists*, Cambridge University Press (2006) 33

- [46] M. Dion, H. Rydberg, E. Schröder, D. C. Langreth, B. I. Lundqvist *Van der Waals Density Functional for General Geometries*, Phys. Rev. Letters, vol. 92, (2004) 34, 48
- [47] T. Thonhauser, V. R. Cooper, S. Li, A. Puzder, P. Hyldgaard, D. C. Langreth *Van der Waals density functional: Self-consistent potential and the nature of the van der Waals bond*, Phys. Rev. B, **76**, 125112 (2007) 34, 48
- [48] G. Román-Pérez, J. M. Soler *Efficient Implementation of a van der Waals Density Functional: Application to Double-Wall Carbon Nanotubes*, Phys. Rev. Letters, **103**, 096102 (2009) 34, 48
- [49] D. C. Langreth, M. Dion, H. Rydberg, E. Schröder, P. Hyldgaard, B. I. Lundqvist, *Van der Waals Density Functional Theory with Applications*, Int. Jour. Quant. Chem., Vol 101, 599-610 (2005) 34
- [50] Zhang, Yang, *Comment on "Generalized Gradient Approximation Made Simple"* Phys. Rev. Letters, **80**, 890 (1998) 34
- [51] J. P. Perdew, Y. Wang, *Accurate and simple analytic representation of the electron-gas correlation energy*, Phys. Rev. B, vol. 45 (1992) 34
- [52] J.P.Perdew, *Density-functional approximation for the correlation energy of the inhomogeneous electron gas*, Phys. Rev. B **33**, 8800 (1986) 34
- [53] K. Lee, É. D. Murray, L. Kong, B. I. Lundqvist and D. C. Langreth *Higher-accuracy van der Waals density functional*, Phys. Rev. B, **82**, 081101(R) (2010) 34, 35, 48
- [54] V. R. Cooper, *Van der Waals density functional: An appropriate exchange functional*, Phys. Rev. B **81**, 161104(R) (2010) xv, 35, 36, 48
- [55] S. Grimme, *Semiempirical GGA-Type Density Functional Constructed with a Long-Range Dispersion Correction*, J. Comp. Chem. 27, 1787 (2006) 33, 48

- [56] V. Barone, M. Casarin, D. Forrer, M. Pavone, M. Sambri, A. Vittadini, *Role and Effective Treatment of Dispersive Forces in Materials: Polyethylene and Graphite Crystals as Test Cases*, J. Comp. Chem. 30, 934 (2009) 33, 48
- [57] I. Hamada, M. Otani *Comparative van der Waals density-functional study of graphene on metal surfaces*, Phys. Rev. B **82**, 153412 (2010) xiv, 6, 7, 35
- [58] H. J. Monkhorst, J. D. Pack, *Special points for Brillouin-zone integrations*, Phys. Rev. B, vol. 13 (1976) 29, 48
- [59] J. Moreno, J. M. Soler, *Optimal meshes for integrals in real- and reciprocal-spaces unit cells*, Phys. Rev. B, vol. 45 (1992) xiv, 28, 29
- [60] J. C. Phillips, L. Kleinman, *New Method for Calculating Wave Functions in Crystals and Molecules* Phys. Rev. 116, 287 (1959). 30
- [61] S. Baroni, S. de Gironcoli, A. D. Corso, P. Giannozzi *Phonons and related crystal properties from density-functional perturbation theory*, Rev. of Mod. Phys., vol. 73, 515-562 (2001) 45, 47
- [62] M. Born, K. Huang *Dynamical theory of crystal lattices (Oxford Classic Texts in the Physical Sciences)*, A Clarendon Press Publication (1954) 36
- [63] G. P. Srivastava *The Physics of Phonons*, Adam Hilger (1990) 36, 42
- [64] J.-A. Yan, W. Y. Ruan, M. Y. Chou, *Phonon dispersions and vibrational properties of monolayer, bilayer, and trilayer graphene: Density-functional perturbation theory*, Phys. Rev. B, **77**, 125401 (2008) xv, 41
- [65] K. Kunc, R. M. Martin, *Ab Initio Force Constants of GaAs: A New Approach to Calculation of Phonons and Dielectric Properties*, Phys. Rev. Lett. **48**, 406 (1982)

- [66] M. S. Dresselhaus, G. Dresselhaus, A. Jorio, *Group Theory - Applications to the Physics of Condensed Matter*, Springer (2010) 45
- [67] L. M. Malard, D. L. Mafra, M. H. D. Guimarães, M. S. C. Mazzoni, A. Jorio, *Group theory analysis of electrons and phonons in N-layer graphene systems*, Phys. Rev. B **79**, 125426, (2008) 45
- [68] P. Giannozzi, S. Baroni, N. Bonini, M. Calandra, R. Car, C. Cavazzoni, D. Ceresoli, G. L. Chiarotti, M. Cococcioni, I. Dabo, A. Dal Corso, S. Fabris, G. Fratesi, S. de Gironcoli, R. Gebauer, U. Gerstmann, C. Gougoussis, A. Kokalj, M. Lazzeri, L. Martin-Samos, N. Marzari, F. Mauri, R. Mazzarello, S. Paolini, A. Pasquarello, L. Paulatto, C. Sbraccia, S. Scandolo, G. Sclauzero, A. P. Seitsonen, A. Smogunov, P. Umari, R. M. Wentzcovitch, *QUANTUM ESPRESSO: a modular and open-source software project for quantum simulations of materials* J.Phys.:Condens.Matter, 21, 395502 (2009) 6, 48, 60
- [69] A. Dal Corso, S. Baroni, R. Resta, S. de Gironcoli, *Ab initio calculation of phonon dispersions in II-VI semiconductors*, Phys. Rev. B **47**, 3588 (1993) 48
- [70] A. M. Rappe, K. M. Rabe, E. Kaxiras, J. D. Joannopoulos, *Optimized pseudopotentials*, Phys. Rev. B 41, 1227 (1990) (erratum: Phys. Rev. B 44, 13175 (1991)) 48
- [71] N. Mounet and N. Marzari, *First-principles determination of the structural, vibrational and thermodynamic properties of diamond, graphite, and derivatives*, Phys. Rev. B **71**, 205214 (2005) xv, xvi, 51, 52, 53, 54, 55, 58, 60, 61
- [72] O. L. Blakslee, D. G. Proctor, E. J. Seldin, G. B. Spence, T. Weng, *Elastic Constants of Compression Annealed Pyrolytic Graphite*, J. Appl. Phys. **41**, 3373 (1970) xv, 51, 56, 57

- [73] J. R. Macdonald, *Review of Some experimental and Analytical Equations of State*, Rev. Mod. Phys., Vol. 41 (1969) 49
- [74] B. D. Jensen, K. E. Wise, G. M. Odegard, *Simulation of the Elastic and Ultimate Tensile Properties of Diamond, Graphene, Carbon Nanotubes, and Amorphous Carbon Using a Revised ReaxFF Parametrization*, J. Phys. Chem. A, 119 (37), pp 9710-9721 (2015) 50
- [75] P. Lambin, *Elastic Properties and Stability of Physisorbed Graphene*, Appl. Sci., 4, 282-304 (2014) 50, 51
- [76] G. Cao, *Atomistic Studies of Mechanical Properties of Graphene*, Polymers, 6, 2404-2432 (2014) 50, 51
- [77] F. Behroozi, *Theory of Elasticity in Two Dimensions and Its Application to Langmuir-Blodgett Films*, Langmuir, 12, 2289-2291 (1996) 50
- [78] X. Chen, F. Tian, C. Persson, W. Duan, Nan-xian Chen *Interlayer interactions in graphites*, Sci. Rep. 3, 3046; DOI:10.1038/srep03046 (2013) xvi, 6, 58
- [79] L. A. Girifalco, R. A. Lad, *Energy of Cohesion, Compressibility, and the Potential Energy Functions of the Graphite System*, J. Chem. Phys. **25**, 693 (1956) xvi, 58
- [80] L. X Benedict, N. G. Chopra, M. L. Cohen, A. Zettl, S. G. Louie, V. H. Crespi, *Microscopic determination of the interlayer binding energy in graphite* Chem. Phys. Lett. **286**, 490 (1998) xvi, 58
- [81] R. Zacharia, H. Ulbricht, T. Hertel, *Interlayer cohesive energy of graphite from thermal desorption of polyaromatic hydrocarbons*, Phys. Rev. B **69**, 155406 (2004) xvi, 58

- [82] Z. Liu, J. Z. Liu, Y. Cheng, Z. Li, L. Wang, Q. Zheng, *Interlayer binding energy of graphite: A mesoscopic determination from deformation* Phys. Rev. B **85**, 205418 (2012). xvi, 58
- [83] K. V. Zakharchenko, M. I. Katsnelson, A. Fasolino, *Finite Temperature Lattice Properties of Graphene beyond the Quasiharmonic Approximation*, Phys. Rev. Lett. **102**, 046808 (2009) 51
- [84] G. Kalosakas, N. N. Lathiotakis, C. Galiotis, K. Papagelis, *In-plane force fields and elastic properties of graphene*, Journal of Applied Physics **113**, 134307 (2013) 51
- [85] R. C. Andrew, R. E. Mapasha, A. M. Ukpong, N. Chetty *Mechanical properties of graphene and boronitrene*, Phys. Rev. B **85**, 125428 (2012) 51
- [86] J. Maultzsch, S. Reich, C. Thomsen, H. Requardt, and P. Ordejón, *Phonon Dispersion in Graphite*, Phys. Rev. Lett. **92**, 075501, (2004) xvi, 60, 61
- [87] C. Oshima, T. Aizawa, R. Souda, Y. Ishizawa, Y. Sumiyoshi, *Surface phonon dispersion curves of graphite (0001) over the entire energy region*, Solid State Communications, Vol. 65, Issue 12, 1601-1604(1988) xvi, 60, 61
- [88] S. Siebentritt, R. Pues, Karl-Heinz Rieder, and A. M. Shikin *Surface phonon dispersion in graphite and in a lanthanum graphite intercalation compound*, Phys. Rev. B **55**, 7927 (1997) xvi, 60, 61
- [89] H. Yanagisawa, T. Tanaka, Y. Ishida, M. Matsue, E. Rokuta, S. Otani, C. Oshima *Analysis of phonons in graphene sheets by means of HREELS measurement and ab initio calculation*, Surf. Interface Anal. (2005); 37: 133-136 xvi, 60, 61
- [90] R. Nicklow, N. Wakabayashi, H. G. Smith, *Lattice Dynamics of Pyrolytic Graphite*, Phys. Rev. B **5**, 4951 (1972) xvi, 60, 61

- [91] P. C. Eklund, J. M. Holden, R. A. Jishi, *Vibrational Modes of Carbon Nanotubes; Spectroscopy and Theory*, Carbon, vol. 33, No. 7, 959-972 (1995) xvii, xviii, xix, 63, 67, 68, 69, 71
- [92] R. Sabatini, E. Küçükbenli, C. H. Pham, S. de Gironcoli *Phonons in nonlocal van der Waals density functional theory*, Phys. Rev. B **93** 235120 (2016) 6, 60
- [93] L. Wirtz, A. Rubio, *The phonon dispersion of graphite revisited*, Solid State Communications **131** 141-152 (2004) 86
- [94] C. H. Lui, T. F. Heinz, *Measurements of layer breathing mode vibrations in few-layer graphene*, Phys. Rev. B, **87**, 121404(R) (2013) xvii, xviii, 67, 68
- [95] D. Boschetto, L. Malard, C. H. Lui, K. F. Mak, Z. Li, H. Yan, T. F. Heinz, *Real-Time Observation of Interlayer Vibrations in Bilayer and Few-Layer Graphene*, Nano Lett., 13 (10), pp 4620-4623 (2013) 87
- [96] S. Pisana, M. Lazzeri, C. Casiraghi, K. S. Novoselov, A. K. Geim, A. C. Ferrari, F. Mauri, *Breakdown of the adiabatic Born-Oppenheimer approximation in graphene*, Nature Materials **6**, 198-201 (2007) 73
- [97] C. Cohen-Tannoudji, B. Diu, F. Laloe, *Quantum Mechanics (vol. 2)*, John Wiley (1977) 92

Appendix A

Eigenvectors for frozen phonon calculations

As explained in section 2.6.2 the knowledge of the eigenvectors u_α allow us to relate variations of energy to the eigenvalues of the dynamical matrix through eq. 2.103. As we are interested only in shear and layer breathing modes, we can model each graphene layer in multilayer graphene or graphite as a "particle". These modes belong to the Γ point, making the use of supercells unnecessary.

The shear and layer breathing modes are uncoupled due to symmetry, so we can deal with each one separately. In both cases, as we show below, the associated dynamical matrices have the same form, but the force constants are different.

We include only first neighbor interactions in this model, as we are dealing with VDW interactions. One can estimate for the case of graphite the second order force constant by remembering that the VDW interaction is proportional to $1/r^6$, and that the next nearest layer will be at a distance that is twice the distance that the first neighbor is. With that, the ratio between the force that the next nearest layer exerts and the force that the nearest layer exerts over a layer is $(1/2)^7 \approx 0.01$. Therefore, the next nearest layer force constant is about 1% of the nearest layer force constant. For bonded interactions, the inclusion of up to fourth neighbors is necessary in graphite [93].

As we are approximating our problem to N coupled harmonic oscillators, the higher frequencies for each N -layer graphene is given by [95]

$$\omega_N = \omega_\infty \cos\left(\frac{\pi}{2N}\right); \quad (\text{A.1})$$

where ω_∞ is the frequency of an infinite 1D linear chain (or in our context, graphite). The convergence behavior in fig. A.1 is well reproduced by our results in figs. 3.24 and 3.22.

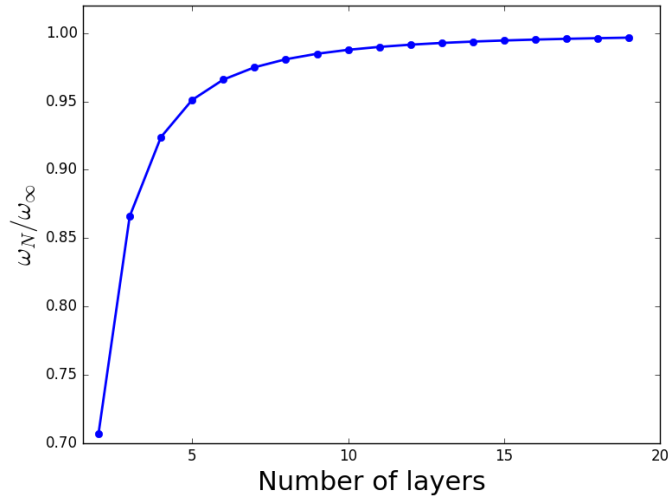


Figure A.1: Plot of the ratio ω_N/ω_∞ as a function of the number of layers using equation A.1.

One can see that the frequencies from the higher eigenvalues described below obey the equation A.1.

A.1 Bilayer graphene

For bilayer graphene, the dynamical matrix at the Γ point is given by

$$D = \frac{1}{M} \begin{bmatrix} c & -c \\ -c & c \end{bmatrix}; \quad (\text{A.2})$$

where c is the force constant between the two layers (which is different for shear and layer breathing modes) and $M = 2M_{carbon}$. The eigenvectors are given by

$$\begin{bmatrix} 1 \\ 1 \end{bmatrix}, \begin{bmatrix} 1 \\ -1 \end{bmatrix}; \quad (\text{A.3})$$

The first one corresponds to a translation of the center of mass and the second to a vibrational mode (shear or layer breathing). The corresponding eigenvalues are respectively 0 and $2c/M$.

A.2 Trilayer graphene

For trilayer graphene, the dynamical matrix at the Γ point is given by

$$D = \frac{1}{M} \begin{bmatrix} c & -c & 0 \\ -c & 2c & -c \\ 0 & -c & c \end{bmatrix}; \quad (\text{A.4})$$

The eigenvectors are given by

$$\begin{bmatrix} 1 \\ 1 \\ 1 \end{bmatrix}, \begin{bmatrix} 1 \\ -2 \\ 1 \end{bmatrix}, \begin{bmatrix} -1 \\ 0 \\ 1 \end{bmatrix}; \quad (\text{A.5})$$

and the corresponding eigenvalues are respectively 0, c/M and $3c/M$.

A.3 4-layer graphene

For 4-layer graphene, the dynamical matrix at the Γ point is given by

$$D = \frac{1}{M} \begin{bmatrix} c & -c & 0 & 0 \\ -c & 2c & -c & 0 \\ 0 & -c & 2c & -c \\ 0 & 0 & -c & c \end{bmatrix}; \quad (\text{A.6})$$

The eigenvectors are given by

$$\begin{bmatrix} 1 \\ 1 \\ 1 \\ 1 \end{bmatrix}, \begin{bmatrix} 1 \\ -1 \\ -1 \\ 1 \end{bmatrix}, \begin{bmatrix} -1 \\ -\frac{1}{1+\sqrt{2}} \\ \frac{1}{1+\sqrt{2}} \\ 1 \end{bmatrix}, \begin{bmatrix} -1 \\ \frac{1}{\sqrt{2}-1} \\ \frac{1}{\sqrt{2}-1} \\ 1 \end{bmatrix}; \quad (\text{A.7})$$

and the corresponding eigenvalues are respectively 0, $2c/M$, $(2 - \sqrt{2})c/M$ and $(2 + \sqrt{2})c/M$.

A.4 5-layer graphene

For 5-layer graphene, the dynamical matrix at the Γ point is given by

$$D = \frac{1}{M} \begin{bmatrix} c & -c & 0 & 0 & 0 \\ -c & 2c & -c & 0 & 0 \\ 0 & -c & 2c & -c & 0 \\ 0 & 0 & -c & 2c & -c \\ 0 & 0 & 0 & -c & c \end{bmatrix}. \quad (\text{A.8})$$

The eigenvectors are given by

$$\begin{bmatrix} 1 \\ 1 \\ 1 \\ 1 \\ 1 \end{bmatrix}, \begin{bmatrix} -1 \\ \frac{1-\sqrt{5}}{2} \\ 0 \\ \frac{\sqrt{5}-1}{2} \\ 1 \end{bmatrix}, \begin{bmatrix} 1 \\ \frac{\sqrt{5}-3}{2} \\ 1 - \sqrt{5} \\ \frac{\sqrt{5}-3}{2} \\ 1 \end{bmatrix}, \begin{bmatrix} -1 \\ \frac{\sqrt{5}+1}{2} \\ 0 \\ -\frac{\sqrt{5}+1}{2} \\ 1 \end{bmatrix}, \begin{bmatrix} 1 \\ -\frac{\sqrt{5}+3}{2} \\ 1 + \sqrt{5} \\ -\frac{\sqrt{5}+3}{2} \\ 1 \end{bmatrix}; \quad (\text{A.9})$$

and the corresponding eigenvalues are respectively 0, $[(3 - \sqrt{5})/2]c/M$, $[(5 - \sqrt{5})/2]c/M$, $[(3 + \sqrt{5})/2]c/M$ and $[(5 + \sqrt{5})/2]c/M$.

A.5 Graphite

In the graphite case we make use of PBC. For interlayer vibrations, one can consider graphite as an infinite 1D linear homogeneous chain [12]. The dynamical matrix at the Γ point is given by

$$D = \frac{1}{M} \begin{bmatrix} 2c & -2c \\ -2c & 2c \end{bmatrix}; \quad (\text{A.10})$$

The eigenvectors are given by

$$\begin{bmatrix} 1 \\ 1 \end{bmatrix}, \begin{bmatrix} 1 \\ -1 \end{bmatrix}. \quad (\text{A.11})$$

The corresponding eigenvalues are respectively 0 and $4c/M$. As in the above cases this analysis is valid for the shear and layer breathing modes (each one with a different force constant c).

Appendix B

Anharmonic Effects included by First Order Perturbation Theory

The unperturbed quantum harmonic oscillator hamiltonian is given by

$$H^{(0)} = \frac{\hat{p}^2}{2m} + \frac{1}{2}m\omega_0^2\hat{x}^2; \quad (\text{B.1})$$

and its eigenvalues are

$$E_n^{(0)} = \hbar\omega_0 \left(n + \frac{1}{2} \right); \quad (\text{B.2})$$

for each eigenvector $|n^{(0)}\rangle$. The frequency for a phonon in this quantum harmonic oscillator is given by

$$\hbar\omega_f = E_1^{(0)} - E_0^{(0)} \quad (\text{B.3})$$

$$\omega_f = \omega_0;$$

If we want to include anharmonic effects, we can do it by using the following perturbation

$$H' = \lambda x^4; \quad (\text{B.4})$$

where λ is a constant. This particular form of perturbation is adequate for the out-of-plane mode of graphite, as the potential energy with respect to the mode displacement is

symmetric with respect to x , as it can be seen in Fig. 3.17. For multilayer systems and in-plane modes, a term proportional to x^3 may appear, but energy eigenvalue corrections from this term in first-order perturbation theory are zero. The first order correction to the energy is given by

$$E_n^{(1)} = \langle n^{(0)} | H' | n^{(0)} \rangle. \quad (\text{B.5})$$

To evaluate the term $\langle n^{(0)} | x^4 | n^{(0)} \rangle$ we can make use of the creation and annihilation operators [97], writing \hat{x} as a function of \hat{a} and \hat{a}^\dagger .

The first correction in energy is given by

$$E_n^{(1)} = \lambda \left(\frac{\hbar}{2m\omega_0} \right)^2 (6n^2 + 6n + 3). \quad (\text{B.6})$$

With this information we can modify the phonon frequency

$$\begin{aligned} \hbar\omega_f &= (E_1^{(0)} + E_1^{(1)}) - (E_0^{(0)} + E_0^{(1)}) \\ \omega_f &= \omega_0 + 3\lambda \frac{\hbar}{m^2\omega_0^2}; \end{aligned} \quad (\text{B.7})$$

In summary, if in frozen phonon calculations we fit an energy curve by a polynomial $V(x) = a_0 + a_1x + a_2x^2 + a_3x^3 + a_4x^4 + \dots$, the phonon frequency as a function of a_2 and a_4 is

$$\omega_f = \left(\frac{2a_2}{m} \right)^{1/2} + \frac{3}{2} \frac{\hbar a_4}{ma_2}. \quad (\text{B.8})$$